The Abundance of Carbon Monoxide in Neptune's Atmosphere

A Thesis Submitted to the
College of Graduate Studies and Research
in Partial Fulfillment of the Requirements
for the degree of Doctor of Philosophy
in the Department of Physics and Engineering Physics
University of Saskatchewan
Saskatoon

By

Brigette Emily Hesman

Permission to Use

In presenting this thesis in partial fulfilment of the requirements for a Postgraduate degree from the University of Saskatchewan, I agree that the Libraries of this University may make it freely available for inspection. I further agree that permission for copying of this thesis in any manner, in whole or in part, for scholarly purposes may be granted by the professor or professors who supervised my thesis work or, in their absence, by the Head of the Department or the Dean of the College in which my thesis work was done. It is understood that any copying or publication or use of this thesis or parts thereof for financial gain shall not be allowed without my written permission. It is also understood that due recognition shall be given to me and to the University of Saskatchewan in any scholarly use which may be made of any material in my thesis.

Requests for permission to copy or to make other use of material in this thesis in whole or part should be addressed to:

Head of the Department of Physics and Engineering Physics
116 Science Place
University of Saskatchewan
Saskatoon, Saskatchewan
Canada
S7N 5E2

Abstract

Carbon Monoxide (CO) was discovered in the stratosphere of Neptune from the detection of the J=3-2 and J=2-1 rotational transitions in emission at 345.8 and 230.5 GHz respectively. It was conventionally thought that all of the atmospheric carbon should be in its reduced form of methane (CH_4). Two sources of stratospheric CO have been postulated: CO transported from the interior by convection due to Neptune's strong internal heat source (internal source); or, CO produced through photochemical reactions from an external supply of water (external source).

In this research project the J=3-2 transition of CO was observed to find the CO profile in Neptune's atmosphere and determine the mechanism producing CO. Three instruments were used at the James Clerk Maxwell Telescope (JCMT) to measure the CO line: the heterodyne receiver B3; the University of Lethbridge Fourier Transform Spectrometer (FTS); and, the Submillimeter Common User Bolometer Array (SCUBA).

The high resolution (1.25 MHz) of the heterodyne observations over a large frequency range ($\sim$20 GHz) produced a very powerful result because the narrow emission core from the stratosphere and the broad absorption feature arising in the lower atmosphere were measured simultaneously. The CO abundance profile was determined using a model of the J=3-2 CO transition in Neptune's atmosphere developed for this project. Calculations indicate a CO abundance of $1.9^{+0.5}_{-0.3}$x10^{-6} in the upper stratosphere and (0.8 ± 0.2)x10^{-6} in the lower stratosphere and troposphere.

The moderate resolution of the FTS data allowed the broad absorption feature to be measured. Uranus was originally chosen as the calibration source, but the discovery of CO in Uranus by Encrenaz *et al.* (2004), while this project was in progress,

prompted both Neptune and Uranus to be examined for CO absorption. Two data sets (1993 and 2002) were analyzed and it was found that the 1993 spectra produced superior results, giving a CO mole ratio in the lower atmosphere between $0.8\text{x}10^{-6}$ and $2\text{x}10^{-5}$; this agrees, within the uncertainty limit, with the lower atmosphere heterodyne result. A tentative detection of CO in Uranus was also obtained from the 1993 data, with a CO abundance profile constrained to pressures greater than 0.5 bar with an abundance between $5\text{x}10^{-7}$ and $1\text{x}10^{-5}$. The 2002 data were found to be inferior to the 1993 data because of imperfect cancellation of thermal emission from the terrestrial atmosphere.

The 850 μm SCUBA filter profile is well matched to the width of the CO feature. Photometric observations of Neptune and Uranus were used to determine if the reduction in integrated flux due to CO absorption could be detected using SCUBA. A CO mole ratio in the range $(1.2 - 1.7)\text{x}10^{-6}$ was found for Neptune, calibrated against Uranus and assuming no CO in Uranus. Calibration of the Neptune and Uranus SCUBA data against Mars to produce an independent estimate of the CO abundance in both planets did not produce a useful result because of large calibration errors.

Comparison of the results from the three techniques determined that the heterodyne measurement was superior and the derived CO profile was used to determine the source of neptunian CO. It was concluded that the source of CO in Neptune is both internal and external. The lower atmosphere result indicates an interior dominated by water ice. The most likely mechanism for the upper atmosphere CO involves meteoritic ablation, photolysis of H_2O, and chemical reaction with by-products of methane photochemistry. The required H_2O influx for this mechanism is at least two orders of magnitude higher than previously observed, indicating either that the observed H_2O abundance is too small or that CO is produced by a different mechanism.

Acknowledgements

The work presented in this thesis would not have been possible without my supervisor Professor Gary Davis. His guidance and patience are greatly appreciated; even when an ocean separated us, he always made my work a high priority. He offered many extra observing shifts; the data from which have been incredibly valuable in making this thesis possible. During the writing of this thesis he provided helpful advice and willingly gave up numerous weekends to editing. I have learned so much from him, not only about science, but about everything in life. He is my mentor.

During the start of my Ph.D. program, I was part of a planetary astronomy group headed by Professor Davis with two research associates, Joe Taylor and Trevor Fulton. Both Joe and Trevor provided guidance and answers to all of my questions. Most importantly though, they provided friendship and an amazing work environment.

I would like to thank Professor David Naylor and the Astronomical Instrumentation Group at the University of Lethbridge; a large part of this thesis is based on data from the University of Lethbridge Fourier transform spectrometer. Professor Naylor's group was always just a phone call away and willing to help no matter what the time of day when we were at the telescope. Professor Naylor himself was always available to answer questions, even when his schedule was extremely busy. Both he and his technician Gregory Tompkins worked tirelessly on observing runs to ensure the instrument was always functioning properly. There are many other people within Professor Naylor's group who have graciously helped whenever I called on them. For this reason, I wish to recognize Brad Gom, Ian Chapman, Margaret Tahić, and Ian Schofield.

Dr. Doug Johnstone and Rachel Friesen, fellow FTS users, were great support

during observing runs and after. Specifically, I must thank Rachel for making observing runs a lot of fun. She was invaluable for advice and discussion even when we were back at our home institutions. We solved many of our work problems over email and it was wonderful to have her to turn to.

During my time at the University of Saskatchewan I met many great people, two in particular, who continually helped me out with various science and computer issues. I would like to thank Tatyana Chshyolkova for being an awesome office mate and providing helpful scientific advice whenever I needed it. I must also thank Jennifer Hadley, because she was always there to help with my computer systems. Most importantly though, she has been a dear friend; always offering words of encouragement.

Both Dr. Henry Matthews and Dr. Glenn Orton have provided excellent support during this thesis project. Dr. Matthews provided significant help with the heterodyne observations and Dr. Orton graciously provided the temperature profiles for Neptune and Uranus and helped with the Neptune model.

I spent a significant amount of time in Hawaii during my Ph.D. program visiting my supervisor at the Joint Astronomy Centre (JAC). The staff at the JAC were always extremely helpful and friendly. I would like to specifically acknowledge Vicki Barnard because she always ensured my observations were properly set-up, helped with data reduction, and answered any question I posed.

While visiting the JAC, I was able to stay with my supervisor and his wife Caroline Davis. Gary and Caroline always made me feel at home and I look back fondly on my time spent with both of them. I will never forget their hospitality and the many fun activities they took me to; the trip to the Volcano on my birthday was especially memorable.

I was financially supported during my program by a post-graduate NSERC scholarship, the University of Saskatchewan, and my supervisor's NSERC grant.

Finally, this thesis owes much to the support I received from my family. My parents, Gale Easter and Ken Hesman, have always been there supporting me (emotionally and financially) in all my ventures. I must thank my Mom specifically for

being my best friend and believing in my abilities even when I did not. My husband, Don Gaitens, has worked tirelessly on editing this thesis and has cared for me with such generosity and patience. He has been my partner, in love and life, and has truly been amazing. Thank-you.

To my family, who have always supported and believed in me even when I did not.

Contents

List of Tables

List of Figures

List of Abbreviations

AU	Astronomical Unit
CSO	Caltech Submillimeter Observatory
DAS	Digital Autocorrelation Spectrometer
DCM	Down-Converter Modules
FFT	Fast Fourier Transform
FTS	Fourier Transform Spectrometer
FWHM	Full Width Half Maximum
HST	Hubble Space Telescope
IDL	Interactive Data Language
IF	Intermediate Frequency
ILS	Instrument Line Shape
IR	Infrared
IRAM	Institut de Radio Astronomie Millimétrique radio telescope
IRIS	Infrared Spectrometer and Radiometer
ISO	Infrared Space Observatory
JAC	Joint Astronomy Centre
JCMT	James Clerk Maxwell Telescope
LTE	Local Thermodynamic Equilibrium
LO	Local Oscillator
LSB	Lower Sideband
LWS	Long Wavelength Spectrometer
MSISE	Mass Spectrometer, Incoherent Scatter Radar Extended Model
MZ	Mach-Zehnder
NET	Noise Equivalent Temperature
pwv	Precipitable Water Vapour
RSS	Radio Science Subsystem
Rx	Receiver
SCUBA	Submillimetre Common User Bolometer Array
SIS	Superconductor-Insulator-Supercondutor
SNR	Signal-to-Noise Ratio
SSB	Single Sideband
SURF	SCUBA User Reduction Facility

SWS	Short Wavelength Spectrometer
USB	Upper Sideband
UT	Universal Time
UV	Ultraviolet
UVS	Ultraviolet spectrometer
VLT	Very Large Telescope
WVM	Water Vapour Monitor

Chapter 1

Introduction

Neptune is the furthest of the Jovian planets and very poorly understood. The objective of this project was to study the chemical composition of Neptune to more accurately constrain its structure. The history of neptunian observations, including a review of the thermal balance, thermal structure, and chemical composition, are considered first in this chapter. The discovery of CO in Neptune's atmosphere, the measurements that ensued, and the possible sources of neptunian CO follows. The telescope used in this project is the James Clerk Maxwell Telescope (JCMT); a brief overview of the telescope including a discussion of the obstacles facing submillimetre planetary astronomy is provided. This chapter closes with a summary of the objective and organization of this thesis.

1.1 History of observations

Observations of the perturbations of Uranus' orbit taken between 1790 and 1840, were used to discover Neptune. J.C. Adams (in 1843) and U.J. Leverrier (in 1846) independently postulated that the perturbations of Uranus' orbit were due to a more distant planet. Celestial mechanics and Uranus' perturbations were used to determine the mass and orbit of Neptune. At the Berlin observatory in 1846, Johann G. Galle found Neptune within 1° of its predicted position (Zeilik *et al.* 1992).

Early measurements of Neptune's atmospheric composition and temperature structure were obtained by ground-based observatories. These results laid the foundation for understanding Neptune's atmosphere and identified areas that required investigation by the Voyager 2 spacecraft (Voyager, hereafter). The Voyager mission produced

a wealth of data on Neptune's atmosphere due to the wide spectral coverage of its onboard instrumentation. The relevant Voyager observations were carried out with the following instruments: the Ultraviolet Spectrometer (UVS); the Infrared Spectrometer and Radiometer (IRIS); and, the Radio Science Subsystem (RSS). There have been no other probes to Neptune since Voyager; despite this, space-based studies have continued with the Infrared Space Observatory (ISO) and the Hubble Space Telescope (HST). The most significant results, in the determination of Neptune's thermal and chemical structure, from these platforms are reviewed.

1.2 Thermal balance

A comparison of the emitted thermal flux with the absorbed solar flux is key to determining the structure and formation of the planet (Fig. 1.1). The power absorbed from incident sunlight is given by,

$$F_{in} = (1 - A_b)\frac{F_\odot}{r_{AU}^2}\pi R^2, \tag{1.1}$$

where $F_\odot$ is the solar constant, r_{AU} is the heliocentric distance in AU, and πR^2 is the projected surface area of the planet that intercepts solar radiation. An astronomical unit is the mean Sun-to-Earth distance (1 AU = 1.496x10^{11} m). The solar constant is the solar flux at 1 AU ($F_\odot$=1360 Wm^{-2}). A_b is the bond albedo of the planet, which is the fraction of incident energy reflected by the planet in all directions. This quantity was measured by Voyager for each of the Jovian planets and is given in Table 1.1 (Conrath *et al.* 1989).

The power emitted due to thermal emission is given by,

$$F_{out} = 4\pi R^2 \epsilon \sigma T^4, \tag{1.2}$$

where $4\pi R^2$ is the surface area of the planet, ϵ is the emissivity, σ is the Stefan-Boltzmann constant, and T is the temperature of the planet. An emissivity of 0.9 was assumed for this calculation to account for the fact that the Jovian planets are not perfect blackbody radiators (de Pater and Lissauer 2001).

Table 1.1: *The Bond albedo for the Jovian planets (Conrath* et al. *1989).*

Planet	Bond albedo
Jupiter	0.343±0.032
Saturn	0.342±0.030
Uranus	0.290±0.051
Neptune	0.31±0.04

Table 1.2: *The equilibrium temperature and effective temperature for the Jovian planets (de Pater and Lissauer 2001, Hubbard* et al. *1995).*

	Jupiter	Saturn	Uranus	Neptune
Equilibrium Temperature (K)	113	83	60	48
Effective Temperature (K)	124.4±0.3	95.0±0.4	59.1±0.3	59.3±0.8

If the planet is assumed to be in thermal equilibrium Eqs. 1.1 and 1.2 are equated and the equilibrium temperature T_{eq} of the planet is,

$$T_{eq} = \left(\frac{F_{\odot}}{r_{AU}^2} \frac{1 - A_b}{4\epsilon\sigma} \right)^{1/4} . \tag{1.3}$$

This equilibrium temperature can be compared to the measured effective temperature of the planet. The effective temperature T_e is the temperature a blackbody, that radiates with a flux equivalent to the total of the infrared energy flux from the planet, would have. Table 1.2 compares these two values for the Jovian planets.

These values indicate that Uranus is in thermal equilibrium but Jupiter, Saturn, and Neptune must possess an internal heat source to account for their higher effective temperatures. The magnitude of the Jovian internal heat sources is given by the internal energy flux in Table 1.3, as derived from the energy balance. The energy balance is defined as the ratio of the total energy flux from the planet (interior plus reradiated solar flux) to the flux from reradiated solar energy alone. The internal energy flux is defined as the total infrared energy flux minus the flux from reradiated

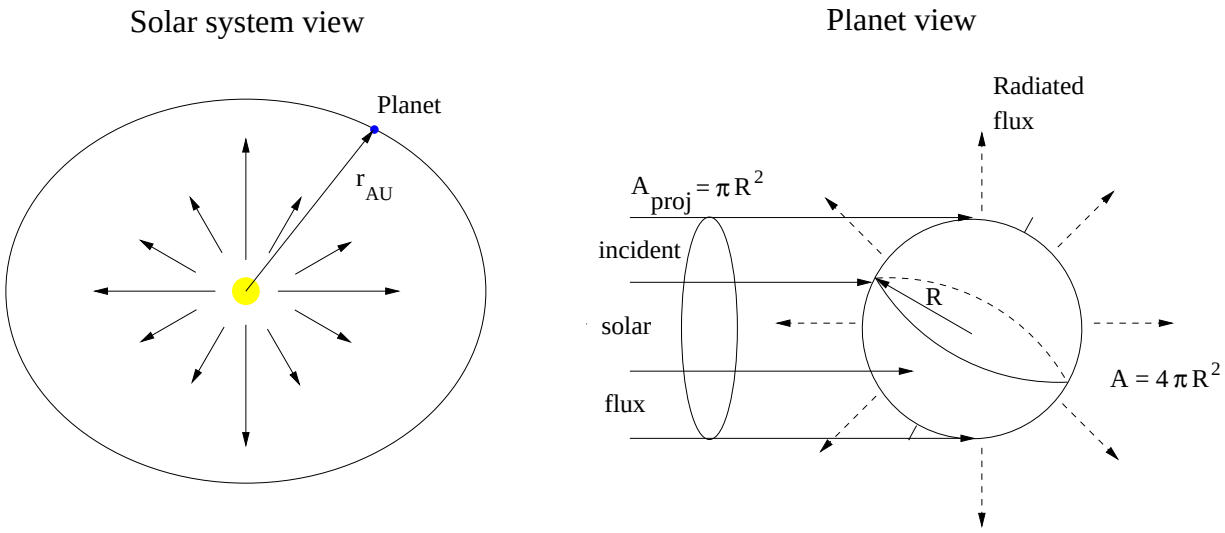

Figure 1.1: *A planet in thermal equilibrium where the absorbed solar flux is balanced by the radiated thermal flux.*

Table 1.3: *The energy balance and internal heat flux for the Jovian planets (de Pater and Lissauer 2001, Hubbard* et al. *1995).*

	Jupiter	Saturn	Uranus	Neptune
Energy Balance	1.67±0.09	1.78±0.09	1.06±0.08	2.61±0.28
Internal Energy Flux ($W \cdot m^{-2}$)	5.44±0.43	2.01±0.14	0.042±0.047	0.433±0.046

solar energy (Hubbard *et al.* 1995).

The release of primordial heat stored during the accretion stage of the planet's formation is likely the major source of internal heat. Jupiter's internal flux is consistent with this mechanism; however, Saturn's internal flux cannot be explained by accretion alone. The additional heat flux in Saturn results from an energy release due to helium differentiation in the interior.

Explaining the difference between Uranus and Neptune's internal fluxes is more difficult. Neptune's internal flux can be explained by energy release from accretion. Uranus, however, has little or no internal heat flux, but it seems unlikely that Uranus did not store heat during its accretion stage. The low internal flux of Uranus can be explained if convection is inhibited in the interior due to differences in density gradients. Compositional gradients may have arisen from the late accretion of large planetesimals which would have broken up on impact and only partially mixed in Uranus' interior (de Pater and Lissauer 2001).

Neptune's internal heat flux indicates that it should have strong convection; this is central to constraining the chemical structure.

1.3 Thermal structure

The thermal structure of Neptune, before the Voyager encounter, was deduced from stellar occultations by the planet and measurements of the atmospheric thermal emission at wavelengths between 7 μm and 3 mm. These measurements provided

thermal structure information for the upper troposphere and stratosphere. The wide spectral coverage of the Voyager instrumentation allowed more altitudes to be probed producing a more complete temperature profile. The temperature structure is discussed in three areas: the deep, middle, and upper atmosphere. A comparison with the Earth's atmosphere is presented last.

1.3.1 Deep atmosphere

The deep atmosphere comprises pressures higher than approximately 2 bars (lower troposphere). The temperatures at these altitudes are key to determining the composition of the interior which places constraints on interior models and formation theories of Neptune. There is a lack of knowledge of deep atmosphere opacity sources and the atmospheric structure because the atmosphere is optically opaque at pressures higher than approximately 2 bars; this limits the ability to extract temperatures from microwave measurements.

The temperature profile must be determined using theoretical calculations involving adiabatic extrapolation using a reference temperature and pressure (T_0, P_0) from the convective part of the upper troposphere. Hydrostatic equilibrium is assumed to construct the adiabatic model,

$$dP = -\rho g dz, \tag{1.4}$$

where dP is the layer atmospheric pressure, ρ is the atmospheric density, g is the acceleration of gravity for Neptune, and dz is the thickness of an atmospheric layer (Lewis 1997). The atmospheric density is determined using the ideal gas law,

$$\rho = \frac{\mu P}{RT}, \tag{1.5}$$

where μ is the molecular weight, P is the atmospheric pressure, R is the universal gas constant, and T is the atmospheric temperature. Substituting Eq. 1.5 into Eq. 1.4 gives,

$$dP = -\frac{\mu P}{RT} g dz. \tag{1.6}$$

When the planetary interior is assumed to lie along an adiabat, the temperature

gradient is given by,

$$\frac{dT}{dz} = -\frac{g}{c_p}, \tag{1.7}$$

where c_p is the specific heat for the mixture of atmospheric gases (de Pater and Lissauer 2001). Assuming that g and c_p are constant allows the atmospheric temperature to be expressed as,

$$T = T_o - \frac{g}{c_p}(z - z_o). \tag{1.8}$$

Substituting Eqs. 1.8 and 1.7 into Eq. 1.6 and integrating from the reference level gives,

$$T = T_o \left(\frac{P_o}{P}\right)^{\mu c_p/R}. \tag{1.9}$$

The specific heat of H_2 is dependent upon the ortho-to-para hydrogen ratio and the rate of equilibration between the two states. The spins of both protons are parallel in the ortho-hydrogen state; in para-hydrogen the proton spins are anti-parallel. The ratio of H_2 in the ortho- and para-states is important to both the thermodynamic and spectroscopic properties of H_2. When the ortho-to-para ratio is equal to the equilibrium ratio at the local temperature at each level in the atmosphere it is referred to as frozen equilibrium. To fit millimetre spectra, a frozen equilibrium adiabat is required (see §1.4.1, Gautier *et al.* 1995).

Condensation of molecular species must be considered at these high pressures in the lower troposphere. CH_4, H_2O, NH_3, PH_3, and H_2S are believed to exist in the deep atmosphere, but condense when the partial pressure of the condensing species reaches the saturation vapour pressure at the local temperature. This condensation causes a release of latent heat and slows cooling, requiring the use of the wet adiabatic lapse rate in determining the temperature structure. This effect can be significant if the species is present in large quantities, as CH_4 is in Neptune. When interpolating temperatures in the lower atmosphere the dry and wet adiabatic lapse rates must be used in the proper areas of the atmosphere. The extrapolation of the temperature profile to the lower troposphere is shown in Fig. 1.2.

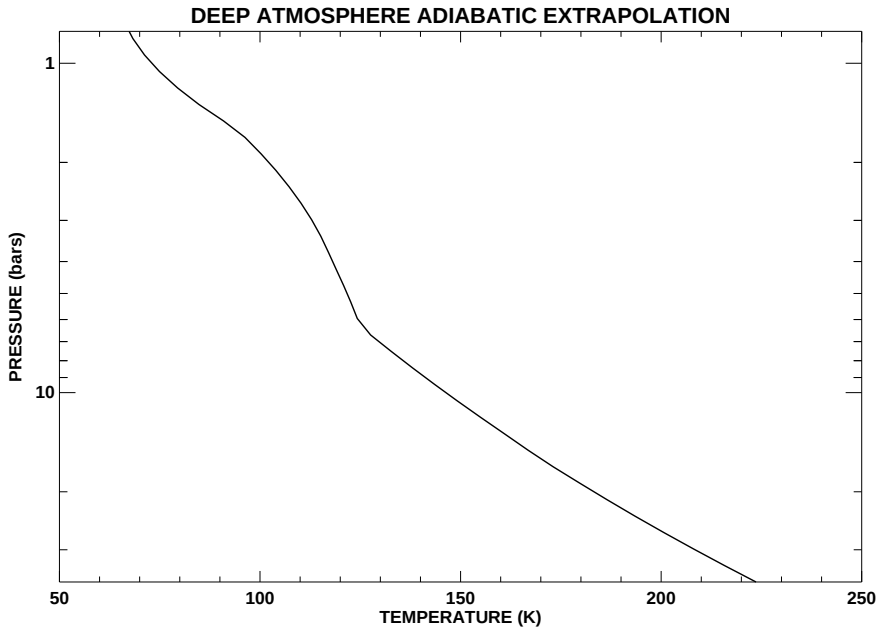

Figure 1.2: *Temperature profile of the deep atmosphere as determined by adiabatic extrapolation (Burgdorf* et al. *2003).*

1.3.2 Middle atmosphere

This region comprises pressures less than 2 bars and greater than 10^{-3} mbar (upper troposphere and stratosphere). Fig. 1.3 is a summary of the temperature profiles extracted from ground-based observations and Voyager data. Three methods have been used to determine the middle atmosphere temperatures: radiative transfer modelling of thermal emission measurements; the Voyager RSS occultation by Neptune; and stellar occultations by Neptune's atmosphere.

The upper troposphere and lower stratosphere temperatures have been deduced primarily by radiative transfer modelling of ground-based thermal emission measurements and the occultation of the Voyager radio link by Neptune. Orton *et al.* (1987, 1990) used perturbations of the radiative-convective models of Appleby (1986) (see inset Fig. 1.3; profiles a, c, and e are from Appleby) to fit their ground-based thermal emission measurements in the range 7–23 μm. The results of this analysis (dashed curve, Fig. 1.3) determined temperatures at pressures between 2 bar and 10^{-3} mbar.

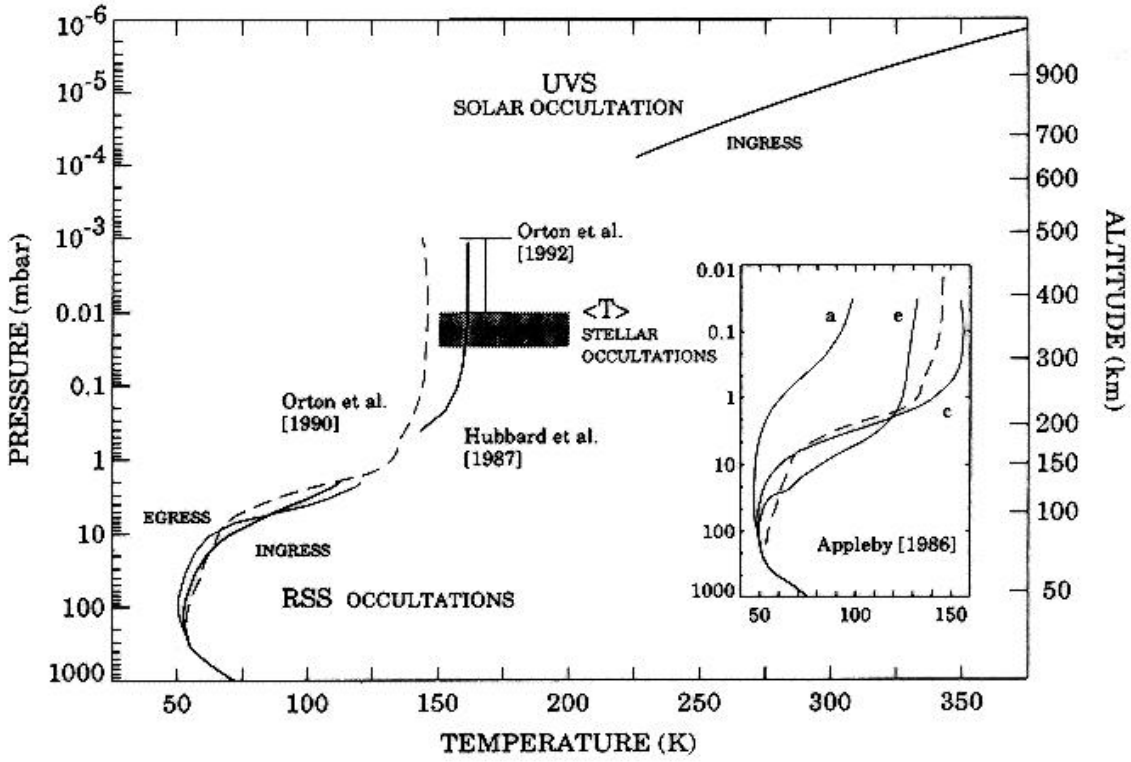

Figure 1.3: *P-T profiles for the atmosphere of Neptune. The RSS occultations provide the thermal structure for P>2 mbar (Lindal* et al. *1990, Lindal 1992). Ground-based measurements by Orton* et al. *(1990), with f(He)=0.15, provide thermal information on the lower stratosphere/upper troposphere (dashed curve). Stellar occultations provide data at pressures from 10^{-3} to 0.03 mbar. The August 20, 1985 occultation observed by Hubbard* et al. *(1987) permitted the construction of the upper stratosphere temperature profile (solid curve). The shaded region corresponds to the range of mean temperatures, defined by Roques* et al. *(1994), after analysis of many stellar occultations. Ground-based measurements by Orton* et al. *(1992) provide a mean stratospheric temperature. The UVS solar occultation analysis by Broadfoot* et al. *(1989) and Yelle* et al. *(1993) provide thermosphere temperatures. The lower inset shows the radiative-convective models of Appleby (1986) (a, c, and e), with a $f(He)/f(H_2)$=0.1, used in the determination of the Orton* et al. *(1990) profile. Note: unless otherwise noted, f(He)=0.19 (Bishop* et al. *1995).*

The RSS on Voyager was used to probe Neptune's atmosphere during the occultation of the spacecraft by Neptune. This was accomplished by tracking the signals transmitted at 3.6 and 13 cm as they passed through Neptune's atmosphere. Ingress and egress of the spacecraft sampled the atmosphere at latitudes from 62°N to 59°N and 45°S to 20°S respectively (Lindal *et al.* 1990, Lindal 1992). The ingress and egress results are shown in Fig. 1.3. The RSS profiles are location-specific to the planet whereas the ground-based observations of Orton *et al.* (1990) are not spatially resolved. This probably accounts for the higher temperatures determined by the Orton *et al.* (1990) analysis in comparison to the results obtained from the RSS data.

The temperature structure was recently updated by Burgdorf *et al.* (2003) in the region of the tropopause (63 to 630 mbar) using disk-averaged spectra of Neptune from ISO's Short Wavelength Spectrometer (SWS) and Long Wavelength Spectrometer (LWS) instruments. The initial input to their derivation was taken from far-infrared and submillimetre disk-averaged photometry (Orton *et al.* 1986, Griffin and Orton 1993) and middle-infrared ground-based spectra (Orton *et al.* 1987, 1990).

The upper stratosphere temperatures have been determined using radiative transfer modelling of ground-based thermal emission measurements and stellar occultations by Neptune's atmosphere. Thermal emission measurements at high spectral resolution, combined with the moderate resolution measurements of Orton *et al.* (1990), allowed Orton *et al.* (1992) to determine a mean temperature in the upper stratosphere of 168 $\pm$ 10 K (see Fig. 1.3). Hubbard *et al.* (1987) and Roques *et al.* (1994) observed stellar occultations to determine the thermal profile of the upper stratosphere. During a stellar occultation, refractive dimming on immersion and brightening on emersion of the stellar light is recorded as a star passes behind Neptune as seen from Earth. The results of these studies are shown in Fig. 1.3. This method, unfortunately, yielded a field of solutions requiring Roques *et al.* (1994) to define a range of stratospheric temperatures at 0.025 mbar of 150 to 200 K. The upper stratosphere comprises the greatest temperature uncertainty in Neptune's thermal profile.

1.3.3 Upper atmosphere

The high atmosphere comprises pressures lower than approximately 10^{-3} mbar (thermosphere). The thermal structure in this region was determined by Voyager UVS solar occultation whereby the transmission of Neptune's atmosphere was determined by measuring the solar spectrum during the atmospheric occultation. UVS transmission spectra were used to calculate the variation of H_2 density with altitude. The H_2 density profile and the hydrostatic law (Eq. 1.4) were used to determine the temperature structure; this required that extinction be caused predominantly by H_2.

H_2 is the dominant absorber in the atmosphere in three wavelength regions allowing the UVS to probe different areas of Neptune's atmosphere. At wavelengths below 80 nm extinction is due to absorption by H_2 in its ionization continuum; these wavelengths probe the upper thermosphere at pressures of approximately 10^{-8} mbar. From 80 to 110 nm, extinction is caused by absorption in the electronic band of H_2, which probes a large pressure range of the lower thermosphere centred at 10^{-5} mbar. The temperatures resulting from the analysis of UVS transmission data in these two wavelength regions are shown in Fig. 1.3 (Broadfoot *et al.* 1989, Yelle *et al.* 1993).

The third region comprises wavelengths longward of 150 nm where Rayleigh-Raman scattering by H_2 is the dominant extinction process. This should allow the upper stratosphere to probed; unfortunately, this region appears to be dominated by hydrocarbon absorption rather than H_2 absorption (Bishop *et al.* 1995). There is, therefore, great uncertainty in the temperatures in the region from 2 to 10^{-4} mbar.

1.3.4 Comparison with Earth's atmosphere

Using the results described above, a thermal profile of Neptune's atmosphere can be constructed. Fig. 1.4 has been constructed in 4 regions:

1. At pressures higher than 10^{-3} bar the profile is the result of the analysis by Burgdorf *et al.* (2003).

2. Between 10^{-3} and 10^{-6} bar, the temperature structure follows that used by

Marten *et al.* (1993); the temperature approaches a constant value of 159 K at 10^{-6} bar (solid line, Fig. 1.4). This upper stratosphere temperature is within the range of temperatures determined by Orton *et al.* (1992) and Roques *et al.* (1994). The large temperature uncertainty in the upper stratosphere requires a range of profiles to be considered (dashed curves, Fig. 1.4).

3. Between 10^{-6} to 4x10^{-8} bar, temperatures are not extracted from measurements and have, therefore, been interpolated between the upper stratosphere and thermosphere profiles. The following interpolation is used in connecting the two regions,

$$\frac{T}{T_o} = \left(\frac{P}{P_o}\right)^{\alpha}, \tag{1.10}$$

where T is the atmospheric temperature, and P is the atmospheric pressure. Reference temperatures of 159 K at 10^{-6} bar and 250 K at 4x10^{-8} bar are used to determine α (Bishop *et al.* 1995).

4. The thermosphere temperature profile ($P <$ 4x10^{-8} bar) is that determined by Broadfoot *et al.* (1989) and Yelle *et al.* (1993). The thermospheric profile has only been measured by Voyager so the temporal and spatial variability is unknown.

The measurements performed in this project are not sensitive to pressures less than 10^{-6} bar; this region of the temperature profile is not required but included here for completeness.

Fig. 1.5 is the Earth's temperature profile for northern winter and summer as calculated using the Mass Spectrometer, Incoherent Scatter Radar Extended Model (MSISE). This model is based on the work of Barnett and Corney (1985) and Hedin (1991). The processes that cause the shape of the Earth's temperature profile can be compared to Neptune's. The troposphere in Neptune is marked by decreasing temperatures; at the tropopause, absorption of solar radiation by CH_4 causes the temperature inversion and increasing temperatures of the stratosphere. On Earth the same process is observed, but with ozone (O_3) as the absorbing molecule.

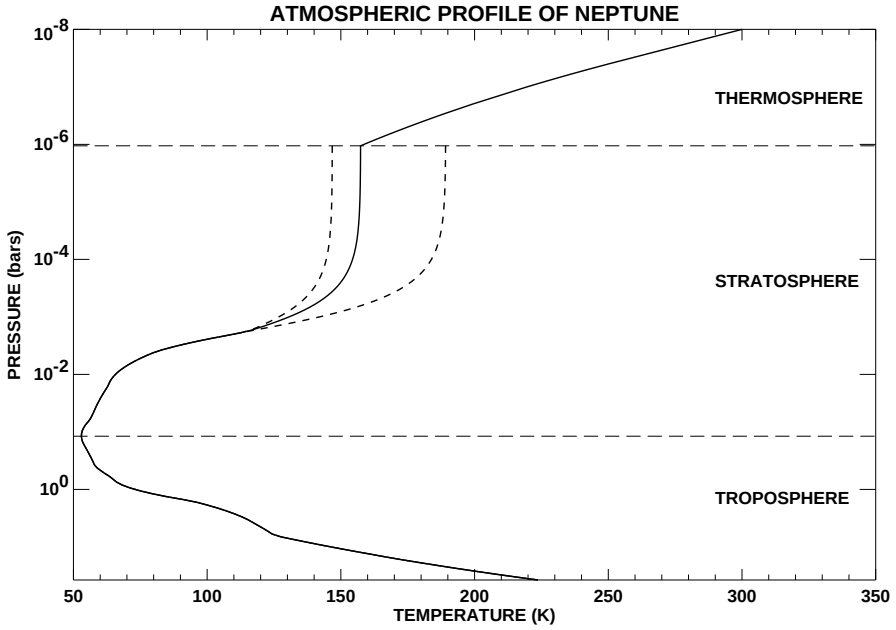

Figure 1.4: *Temperature profile of Neptune's atmosphere derived from ground-based, Voyager, and ISO measurements (Burgdorf* et al. *2003, Marten* et al. *1993, Broadfoot* et al. *1989, Yelle* et al. *1993).*

The upper stratosphere of Neptune approaches a constant temperature, but at the stratopause on Earth the temperature begins to decrease. A lack of ozone absorbing solar radiation causes the decreasing temperatures of the mesosphere on Earth. Neptune and Earth's thermospheres exhibit a strong temperature increase due to the absorption of UV radiation by H_2 in Neptune and O_2 in Earth. The thermosphere marks the region in both planets where molecular diffusion becomes the dominant process over eddy diffusion (turbulent mixing; see §1.4.2).

There are two temperature profiles shown in Fig. 1.5. On Earth, the temperature profile in the mesosphere changes significantly between summer and winter; this is due to breaking waves in the Earth's atmosphere (Lewis 1997). This behaviour is not shown in Neptune's profile. The temperature profile has been monitored for only 20 years; much longer seasons ($\sim$ 80 years between summer and winter) require many generations of observations before Neptune's seasonal response can be determined.

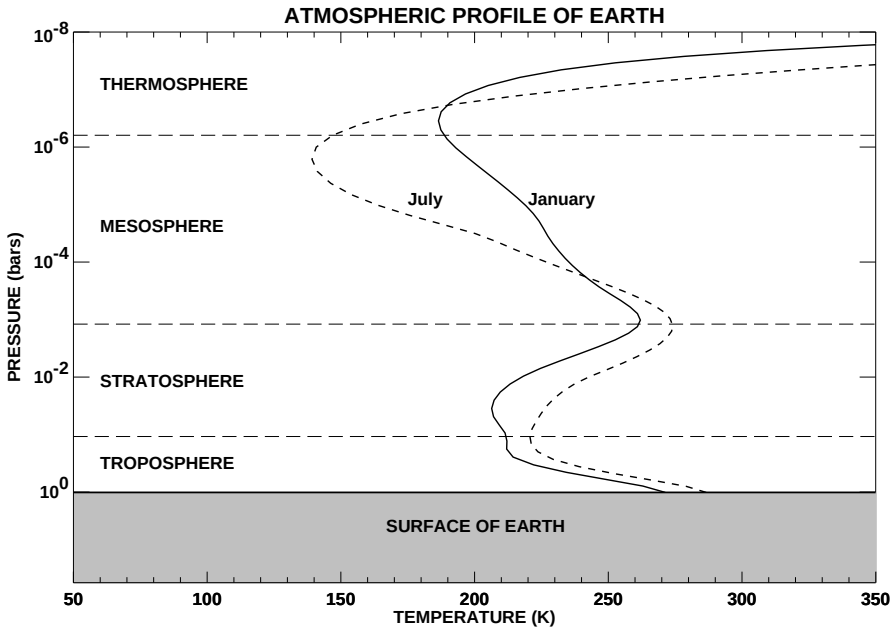

Figure 1.5: *Temperature profile of the Earth's atmosphere at mid-latitudes for two seasons: northern winter (solid), and northern summer (dashed). Temperature data from http://nssdc.gsfc.nasa.gov/space/model/models/msis.html.*

1.4 Chemical composition

The major constituents of Neptune's atmosphere are molecular hydrogen (H_2), helium (He) and methane (CH_4). Methane is of importance in the atmosphere because its absorption of solar photons causes the positive temperature gradient in the stratosphere (see Fig. 1.3). Photochemical reactions resulting from methane photolysis give rise to hydrocarbons such as ethane (C_2H_6), acetylene (C_2H_2), ethylene (C_2H_4), and methyl (CH_3)in the stratosphere. Carbon monoxide (CO), hydrogen cyanide (HCN), monodeuterated methane (CH_3D), and monodeuterated hydrogen (HD) have also been detected. Other species expected to exist deep in the troposphere include water (H_2O), ammonia (NH_3), hydrogen sulphide (H_2S) and phosphine (PH_3), but these have not been detected. Measurements to determine the abundance and profile of the species relevant to this project are discussed in the following sections. The abundances will be reported in terms of the mole ratio q,

$$q = \frac{P_{species}}{P_{total}}, \tag{1.11}$$

where $P_{species}$ is the partial pressure of the species and P_{total} is the total atmospheric pressure.

1.4.1 Hydrogen and Helium

H_2 was first observed in Neptune's atmosphere by Belton and Spinrad (1973). H_2 is a homonuclear molecule and has no electric dipole moment. It should, therefore, exhibit no dipole transitions; however, at high pressures electric dipole absorption is observed (eg. Bishop *et al.* 1998). This absorption is the result of a collision between two molecules (i.e. H_2–H_2) causing a transient dipole moment to arise; during this collision transitions among rotational, vibrational, and translational states can take place. This type of absorption dominates the far-infrared spectrum of Neptune. In addition, H_2 has an electric quadrupole moment. These transitions, while weaker than electric dipole transitions, are also observed in Neptune's spectrum (eg. Baines *et al.* 1995).

Observations of the collision-induced and quadrupole transitions of H_2 have been used to determine the ortho-to-para ratio in Neptune's atmosphere. Frozen equilibrium is usually assumed in model calculations (see §1.3.1). The validity of this assumption has been tested most recently by Conrath *et al.* (1998) and Burgdorf *et al.* (2003); both concluded that the ratio must be near the equilibrium value.

The abundances of H_2 and He have been determined simultaneously by the analysis of a combination of IRIS spectra and egress radio occultation measurements from Voyager. Conrath *et al.* (1991) assumed that only H_2 and He contributed significantly to the mean molecular weight and the coefficient of radio refractivity in the upper troposphere and lower stratosphere. Temperature profiles were calculated from the radio refractivity results for various values of the helium mole fraction. These temperature profiles were used in a radiative transfer model to calculate thermal emission spectra for comparison against IRIS spectra between 25 and 50 μm. The IRIS spectra were obtained in the same latitudinal location as the egress RSS measurements. The best-fit to the IRIS data found a helium mole fraction of $q_{He} = 19.0 \pm 3.2\%$, indicating that $q_{H_2} = 81.0 \pm 3.2\%$ (Conrath *et al.* 1991).

The H_2/He ratio was re-investigated by Burgdorf *et al.* (2003) recently using ISO's SWS and LWS. Disk-averaged mole ratios of $q_{He} = 14.9^{+1.7}_{-2.2}\%$ and $q_{H_2} = 83.1^{+1.7}_{-2.2}\%$ were determined using the most recent temperature profile, a tropospheric CH_4 mole ratio of 2%, and a radiative transfer model incorporating collision-induced absorption of H_2 by H_2, He, and CH_4.

1.4.2 Methane

The low temperatures on Neptune ($\sim$ 50 K near the tropopause) cause CH_4 to condense indicating that the CH_4 abundance profile should be constant in the troposphere until it reaches the saturation layer; at that point the CH_4 abundance profile should follow the vapour pressure curve.

Measurements of the tropospheric CH_4 abundance were not possible using Voyager instruments because the CH_4 fundamental bands at 3.3 and 7.8 μm were obscured by emission from the CH_4-rich stratosphere. The determination of the tropo-

spheric CH_4 mole ratio has relied on ground-based observations in the submillimetre by Orton *et al.* (1986) and visible by Baines *et al.* (1995). The most recent findings show a tropospheric value of $q^t_{CH_4} = 2.2^{+0.5}_{-0.6}\%$ (Baines *et al.* 1995).

Early measurements, by Orton *et al.* (1987, 1990), found that the stratospheric and tropospheric CH_4 abundances were approximately equivalent. The analysis of Voyager UVS measurements by Yelle *et al.* (1993) and Bishop *et al.* (1992) found much lower stratospheric values in the range 0.001–0.1%. Ground-based work in the infrared by Orton *et al.* (1992) and visible by Baines and Hammel (1994) found a similar range to the Voyager results. Most recently, ISO measurements found a stratospheric value of $q^s_{CH_4} = 0.13 \pm 0.08\%$ (B. Bézard, personal communication).

CH_4 gas should be trapped below the tropopause by condensation, due to the low temperatures found there; however, measurements of the stratospheric abundances have proved otherwise ($>$ 10 times the value allowed by saturation). This "leaky tropopause" is explained by Appleby (1986) who labels this mechanism "convective penetration". Appleby argued that supersaturation, partial pressures greater than the vapour pressure at the local temperature, could be caused by rapid upward transport inhibiting condensation as the gas is swept into warmer regions.

The CH_4 abundance profile is shown in Fig. 1.6; between the tropospheric and stratospheric abundances it is limited by condensation. The following vapour pressure equation for CH_4 was used,

$$log_{10}(P) = \frac{-459.82}{T} + 4.09, \tag{1.12}$$

where P is the pressure in bars, and T is the temperature in kelvins (Lide 2003).

CH_4 reaches levels where absorption of solar photons becomes important. The primary photolysis levels for CH_4 occur at pressures $\leq 10^{-3}$ mbar. At these levels CH_4 is converted to higher order hydrocarbons (C_2H_2, C_2H_4, C_2H_6, and CH_3) by photolysis and subsequent chemical reactions (Bishop *et al.* 1995, Schulz *et al.* 1999, Bézard *et al.* 1999). The important effects governing the distribution of hydrocarbons in the upper atmosphere include: diffusive separation, vertical mixing, production and loss processes. These effects are considered using the steady-state continuity

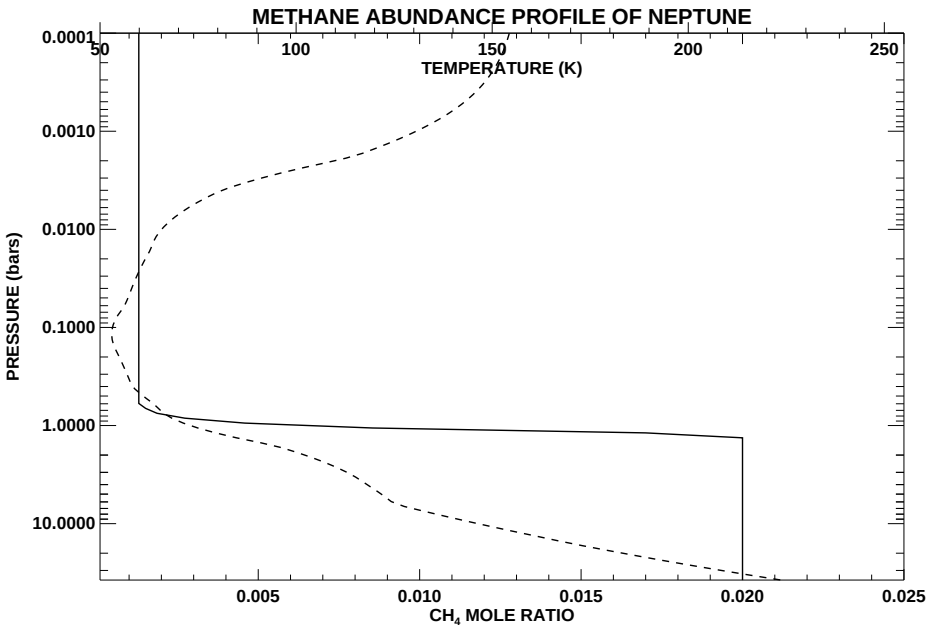

Figure 1.6: *CH_4 profile in Neptune's atmosphere (solid curve). The temperature profile assumed for Neptune's atmosphere is shown as the dashed curve.*

equation,

$$\frac{d\Phi_i}{dz} = P_i - L_i, \tag{1.13}$$

where z is the altitude, Φ_i is the flux of species i, and P_i and L_i are the production and loss rates of the species (Bishop *et al.* 1995). The flux is given by the vertical transport equation,

$$\Phi_i = -D_i \left[\frac{dn_i}{dz} + n_i \left(\frac{1}{H} + \frac{1+\alpha}{T}\frac{dT}{dz} \right) \right] - K \left[\frac{dn_i}{dz} + n_i \left(\frac{1}{H} + \frac{1}{T}\frac{dT}{dz} \right) \right], \tag{1.14}$$

where D_i is the molecular diffusion coefficient, n_i is the number density of constituent i, H is the scale height ($H = k_b T/mg$), α is the thermal diffusion parameter, and K is the eddy diffusion coefficient (de Pater and Lissauer 2001). Molecular diffusion, the vertical movement of individual molecules, only dominates in regions where the atmospheric density is low and mixing is weak (P $< 10^{-8}$ bar). Eddy diffusion, the turbulent movement of air parcels, dominates at pressures greater than 10^{-8} bar. The altitude at which the atmosphere ceases to be dominated by turbulent diffusion and molecular diffusion takes over is referred to both as the homopause and turbopause.

In the stratosphere, where hydrocarbons are produced, eddy diffusion dominates requiring knowledge of the eddy diffusion coefficient to determine the hydrocarbon abundances in this region. It has been conventional to adopt, for K, a dependence on the number density,

$$K(z) = K_0 \left(\frac{n_0}{n(z)} \right)^{\beta}, \tag{1.15}$$

where n is the number density at altitude z, n_0 and K_0 are respectively the number density and eddy diffusion coefficient at the CH_4 homopause (the level to which CH_4 is well mixed in the atmosphere) and β is a fitting parameter used in modelling the observations (Bishop *et al.* 1998).

Hydrocarbons will move downwards through the atmosphere from the location in the stratosphere where they are formed. Their abundances will follow the saturation vapour pressure curve as they move to the tropopause and condense. Their abundances in the stratosphere will be driven by eddy diffusion and photochemical production and loss processes. The hydrocarbon abundance profiles are important, in the context of this thesis, only in that they help constrain the eddy diffusion profile.

Romani *et al.* (1993) used photochemical modelling of Voyager IRIS and UVS measurements of C_2H_2, C_2H_4, and C_2H_6 to determine eddy diffusion profiles. Two types of profile were found: the first used the traditional form of Eq. 1.15 with $\beta = 0.6$ and $K_0 = 10^7$ cm$^2 \cdot$ s^{-1} (Romani "A" profile, hereafter); the second had a stagnant lower stratosphere below a rapidly mixed upper stratosphere with $K = 5\text{x}10^7 \text{cm}^2 \cdot \text{s}^{-1}$ from 1 to 0.001 mbar (Romani "B" profile, hereafter). The Romani B profile was found to produce a better fit to the IRIS and UVS data.

The most recent update to the eddy profile is from observations using ISO of C_2H_4 and CH_3 emission by Schulz *et al.* (1999) and Bézard *et al.* (1999), respectively. Schulz *et al.* found their data were best fit using an eddy profile equivalent to the Romani A profile. Bézard *et al.* also found the Romani A profile to be the best fit; however, they required a lower homopause eddy value of $K_0 = 5\text{x}10^6 \text{cm}^2 \cdot \text{s}^{-1}$.

1.4.3 Minor constituents

CO and HCN were discovered in the stratosphere of Neptune by Marten *et al.* (1993). The discovery of CO and its importance in Neptune's atmosphere is covered in §1.5. Marten *et al.* found a HCN mole fraction of $q = (1.2 \pm 0.4)\text{x}10^{-9}$ using the J=4–3 rotational emission line at 354.5 GHz. The discovery of HCN was unexpected because the species is not expected to survive the low temperatures found at the tropopause. Marten *et al.* postulated that upward transport of N_2 from the interior could subsequently dissociate in the stratosphere and form HCN. There is no direct evidence of N_2 in the upper troposphere to support the internal origin theory and this led Rosenqvist *et al.* (1992) and Lellouch *et al.* (1994) to formulate a theory that nitrogen atoms originate from an exterior source.

CH_3D and HD have been found in Neptune's atmosphere by de Bergh *et al.* (1990), Orton *et al.* (1992) and Feuchtgruber *et al.* (1999), respectively. These species have been used to determine the D/H ratio in Neptune. The deuterium content of Neptune's atmosphere provides a useful constraint on models for planetary origin and evolution. All three measurements concluded that there is deuterium enhancement on Neptune relative to the protosolar abundance.

Feuchtgruber *et al.* (1997) detected gaseous H_2O in the upper atmosphere of Neptune using ISO's SWS. A uniform abundance was assumed above the H_2O condensation level, at approximately 140 K, to find a mole ratio of $q = (1.5 - 3.5)\text{x}10^{-9}$. A transport model was used to calculate the external H_2O flux that corresponds to the measured abundance. In creating this model, both the Romani A and B profiles were assumed (see §1.4.2) to give an H_2O external flux of $(1.2 - 150)\text{x}10^5$ $\text{cm}^{-2}\text{s}^{-1}$.

1.4.4 Deep atmosphere constituents

The composition of the deep atmosphere (P > 8 bars) has been deduced using microwave remote sensing. H_2S, NH_3, PH_3, and H_2O have been used as sources of opacity in radiative transfer models to fit microwave observations; there have been no direct observations of these molecules. The most recent model fits to radio

observations require mole ratios of $q_{H_2S} = (300-600)\text{x}10^{-6}$, $q_{NH_3} = 95\text{x}10^{-6}$, $q_{PH_3} = (2.5-3.5)\text{x}10^{-6}$, and $q_{H_2O} = 1.45\text{x}10^{-3}$ (Hoffman *et al.* 2001).

1.5 CO in Neptune's atmosphere

CO was discovered in the stratosphere of Neptune through the detection of the J=3–2 and 2–1 rotational transitions in emission at 345.8 and 230.5 GHz respectively (Marten *et al.* 1993). Fig. 1.7 shows the original detection of the J=3–2 emission. These narrow emission lines originate in the upper stratosphere of Neptune. Narrow spectral lines arise because the pressure is low since pressure broadening is the dominant process. These lines appear in emission because the temperature of the upper stratosphere is greater than the region in which the surrounding continuum is produced ($\sim$ 90 K, 2 bar). This discovery was unexpected because CO is not thermochemically stable at observable levels (Bishop *et al.* 1995); it was conventionally thought that Neptune's atmospheric carbon must be in its reduced form of CH_4. Several measurements of the stratospheric emission lines followed. Using the JCMT and the Caltech Submillimeter Observatory (CSO), Marten *et al.* (1993) found a CO mole ratio of $(1.2 \pm 0.4)\text{x}10^{-6}$; Rosenqvist *et al.* (1992) used the Institut de Radio Astronomie Millimétrique radio telescope (IRAM) to determine a value of $(0.65 \pm 0.35)\text{x}10^{-6}$; and, recently Marten *et al.* (2005) confirmed their 1993 values using the JCMT and IRAM.

Two explanations have been proposed for the presence of CO in Neptune's stratosphere. The first consists of CO being transported from the interior to higher altitudes by convection due to Neptune's strong internal heat source. If this is the only mechanism, then thermochemical models require the interior to be enriched in oxygen 440 times the solar abundance in order to produce the observed stratospheric CO abundance (Lodders and Fegley 1994), indicating a planetary interior composed primarily of water ice. The second hypothesis involves the external supply of OH radicals or oxygen atoms into the atmosphere where they can be combined with by-products of methane photochemistry to produce CO (Rosenqvist *et al.* 1992). It

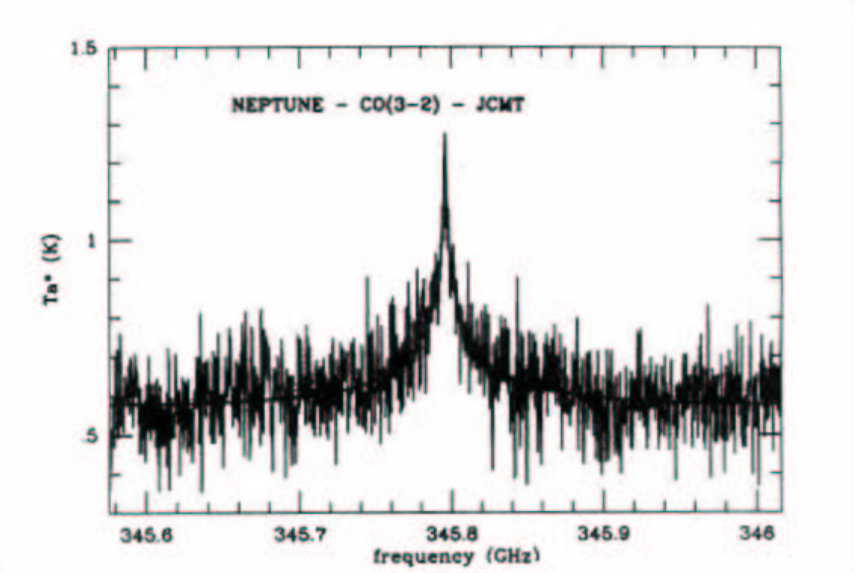

Figure 1.7: *Stratospheric CO line detected by RxB at the JCMT in 1991 (Marten* et al. *1993).*

is unlikely, however, that an external supply of oxygen can be the dominant source of CO in Neptune, considering that Saturn has more abundant water sources (rings, satellites) but a much smaller stratospheric CO abundance ($< 10^{-7}$) (Noll *et al.* 1986).

A measurement of the CO abundance profile through the atmosphere is required in order to determine the correct mechanism. If CO exists in the troposphere, the spectral line will be in absorption because the temperature in the troposphere is lower than the region in which the surrounding continuum is produced ($\sim$ 90 K, 2 bar). The spectral feature will be pressure-broadened due to the high pressures in this region of the atmosphere, resulting in the tropospheric spectral feature being a broad absorption line. These lines are difficult to measure because of the large bandwidth required.

There have been four reported attempts to measure CO in Neptune's troposphere, with divergent results. Guilloteau *et al.* (1993) used a hybrid heterodyne technique on IRAM to measure the reduction in flux that would result from an absorption line. This resulted in a tropospheric abundance of $(0.6 - 1.5)\text{x}10^{-6}$. Naylor *et al.* (1994)

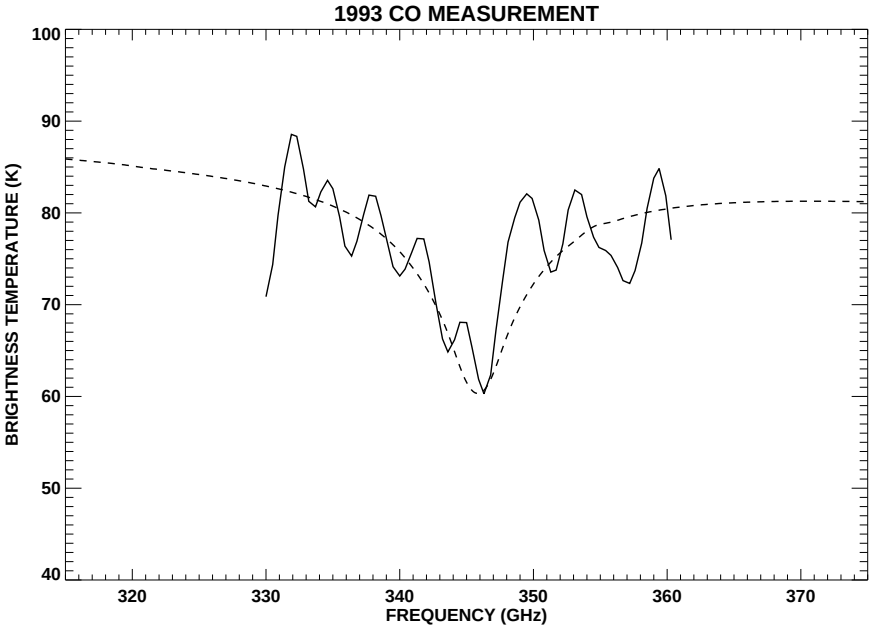

Figure 1.8: *Detection of the J=3–2 CO absorption line. Model fit, dashed curve, is for a CO model ratio of* $1.2\text{x}10^{-6}$*; data is the solid curve (Naylor* et al. *1994).*

used a polarizing Fourier Transform Spectrometer (FTS) at the JCMT to measure the J=3–2 absorption line at 345.8 GHz. The moderate resolution and large spectral bandwidth of an FTS makes it particularly well suited to measuring these strongly pressure broadened absorption lines. A marginal detection was achieved to find a mole ratio of $(0.7 - 1.3)\text{x}10^{-6}$. The measured spectrum, along with a model fit, is shown in Fig. 1.8. The sinusoidal modulation present in the data limited the precision of this measurement. The modulation was attributed to channel fringing, which is the result of multiple reflections in the optics of the photometric detector system. Courtin *et al.* (1996) used the Faint Object Spectrograph onboard the HST to identify the UV Cameron bands of CO leading to a value of $(2.7 \pm 1.8)\text{x}10^{-6}$. Using a different FTS on the CSO, Encrenaz *et al.* (1996) found an upper limit on the tropospheric value of $1.0\text{x}10^{-6}$.

The precision of these measurements limited the ability to draw firm conclusions as to the source of atmospheric CO. A more accurate determination of the CO

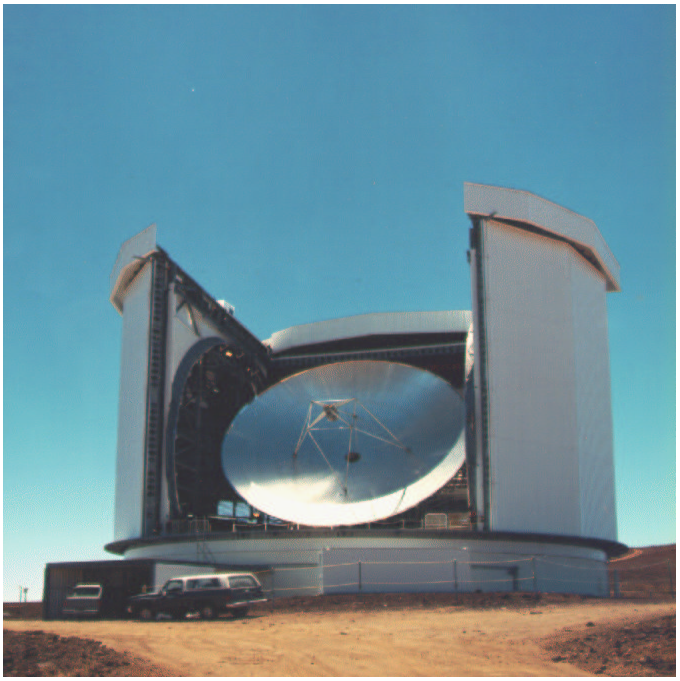

Figure 1.9: *The James Clerk Maxwell Telescope. The telescope is shown here without the Gore-Tex membrane that resides above the telescope. The membrane prevents wind and dirt from entering the dome and is transparent to radiation at these wavelengths.*

abundance profile is required and has been the focus of this thesis project.

1.6 The James Clerk Maxwell Telescope

The CO line in this investigation (J=3–2 at 345.8 GHz, 0.87 mm) is in the submillimetre region of the electromagnetic spectrum. The largest telescope in the world for submillimetre astronomy is the JCMT located on the island of Hawaii on Mauna Kea at an altitude of 4092 m (Fig. 1.9). Mauna Kea is the highest point in the Pacific Ocean and the telescope is above 97% of the water vapour in the terrestrial atmosphere. The JCMT covers a wavelength range from 0.3 to 3 mm. It is a Cassegrain telescope with a 15 m primary dish composed of 276 aluminum panels with each one adjustable to ensure a parabolic surface.

Fig. 1.10 is a schematic of the optical configuration. Radiation is reflected from

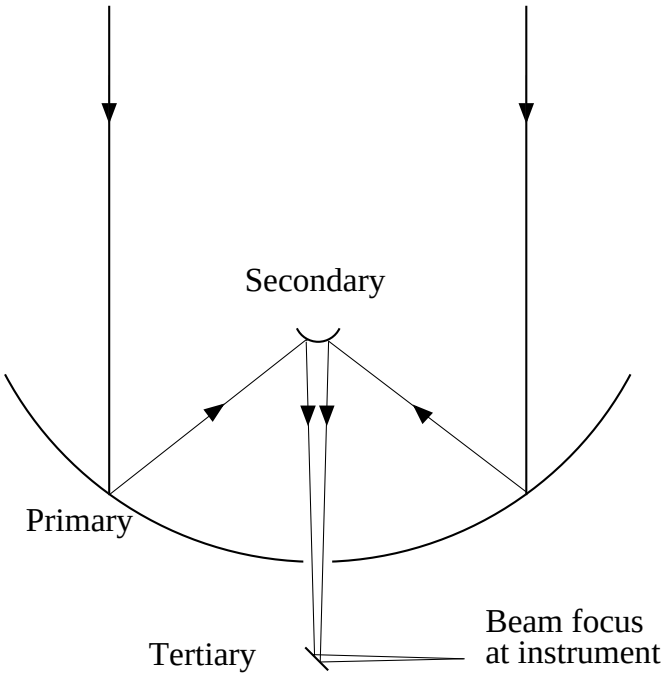

Figure 1.10: *Optical configuration of the JCMT.*

the main dish to the convex secondary where it is redirected through a hole in the main dish to the planar tertiary; from there it is redirected to the selected instrument.

The angular resolution of the JCMT is limited by diffraction. The diffraction limit is, therefore, used to define the beamwidth (B_w) of the primary mirror and is given by,

$$B_w = 1.22\frac{\lambda}{D}, \tag{1.16}$$

where λ is the wavelength of observation and D is the primary mirror diameter (Hanel *et al.* 1992). This gives a beamwidth of approximately $14''$ (arcseconds) at the wavelength of this CO line. Neptune has an equatorial diameter of approximately $2.3''$ and an effective temperature of 59K (Table 1.2). The small size and low temperature of Neptune presents some observational challenges, particularly when viewed through a warm, semi-transparent, and variable atmosphere that fills the telescope beam.

The precision of spectroscopic measurements is limited by the variability of the

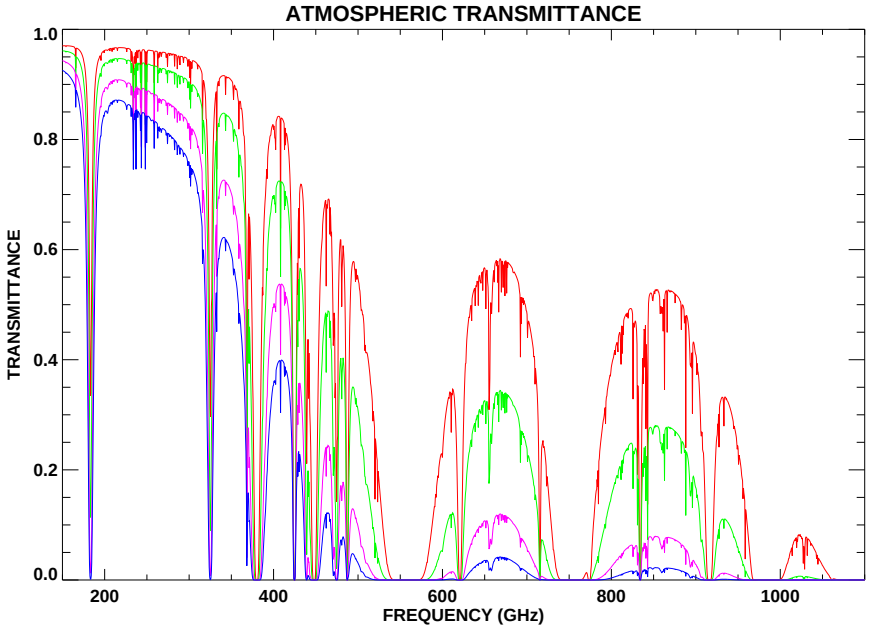

Figure 1.11: *Transmittance of the Earth's atmosphere for pwv values of 0.5mm (red), 1mm (green), 2mm (violet), 3mm (blue).*

Earth's atmosphere. The atmospheric transmittance spectrum above Mauna Kea is shown in Fig. 1.11. The window used for this measurement is located in the 350 GHz region, which is not as sensitive to water vapour as the regions around 600 and 800 GHz. Water vapour content in the atmosphere in quantified by the precipitable water vapour (pwv), which is the depth in millimetres of liquid water that would result from condensing the water vapour in an atmospheric column. Fluctuations in water vapour can hinder the removal of the Earth's atmospheric sky emission; it is for this reason that dry and stable weather is required for this measurement.

Fluctuations in the pwv are a source of noise and have a daily fluctuation that peaks during the middle of the day. The most ideal conditions occur during the night. This is observed on the mountain when the clouds come in during the afternoon and then sink into the valley during the early evening. The sun rising and setting causes turbulence in the atmosphere making measurements during these times nearly impossible (Fig. 1.12).

The atmospheric transmittance is monitored during observations using the JCMT

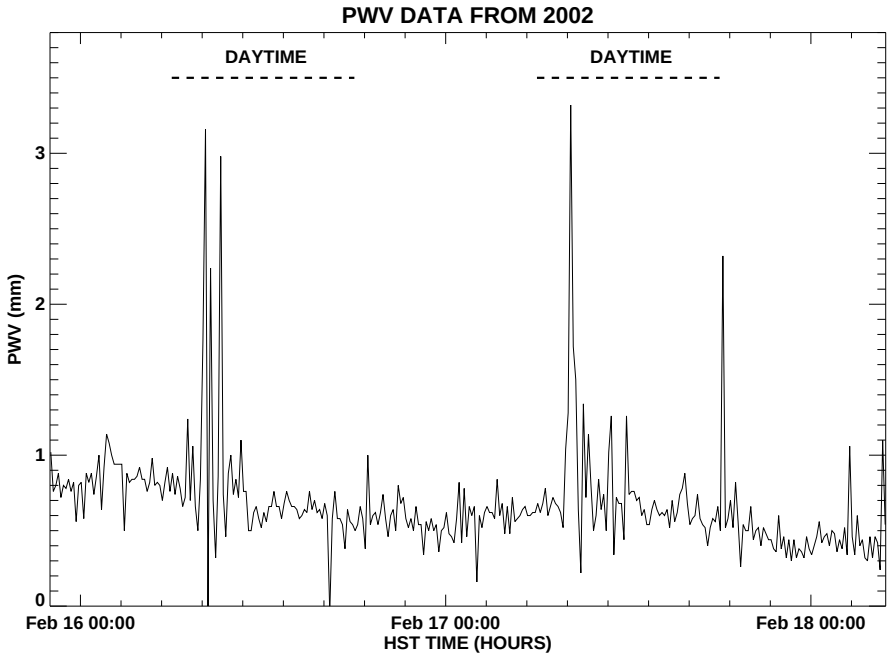

Figure 1.12: *The pwv values over a two-day period in 2002. The daylight hours show significant pwv fluctuations.*

Water Vapour Monitor (WVM). The WVM measures the atmospheric emission across the 183 GHz H_2O line in the telescope line of sight every 1.2 s to determine the optical depth at 183 GHz. The optical depth at 183 GHz is converted to the optical depth at 225 GHz (τ_{225}) for output to the telescope user. Davis *et al.* (1997) defined the relation between the τ_{225} and pwv w (in mm),

$$w = 20(\tau_{225} - 0.016). \tag{1.17}$$

1.7 Organization

The preceding sections of this chapter indicate that the CO abundance profile is poorly constrained. A more accurate profile is required to ascertain the source of atmospheric CO (internal or external). Determining a more accurate CO abundance profile has been the focus of this project. The first step was to develop a radiative transfer model of the CO J=3–2 transition in Neptune's atmosphere to calculate the CO abundance from measurements obtained for this project. This is presented

in Chapter 2. The next three chapters focus on the measurements of this CO line. Three instruments at the JCMT were used:

1. RxB3 was used to perform high resolution heterodyne spectroscopy. This instrument allowed the stratospheric emission and tropospheric absorption to be measured together (Chapter 3).

2. The University of Lethbridge FTS was used to perform low resolution Fourier transform spectroscopy. This instrument was used to observe the tropospheric absorption (Chapter 4).

3. The Submillimetre Common User Bolometer Array (SCUBA) was used to perform photometry of Neptune at 850μm. This instrument was used to measure the integrated flux of Neptune across the 850μm atmospheric window (Chapter 5).

Chapter 6 contains a comparison of the three results and recommendations for future work to be done.

Chapter 2

Radiative Transfer Model

Abundance profiles of atmospheric constituents are determined using model fits to measured spectra. A model of the J=3–2 CO line in Neptune's atmosphere was developed to determine the CO abundance profile from the measured line. This chapter starts with a brief overview of rotational transitions in molecules, then a description of the Neptune CO line model. The last part of this chapter will discuss the models used for the calibration targets: Uranus and Mars.

2.1 Absorption and emission by gases

Absorption and emission of radiation by molecules and atoms cause patterns of spectral lines. A spectral line is the result of a transition between quantized energy states in a molecule (or atom). The energy state is changed by absorption or emission of a photon with a frequency proportional to the energy difference between the initial and final energy states. Transitions are possible among the electronic, vibrational and rotational energy levels.

Vibrational and rotational transitions arise because a molecule is an aggregate of atoms bound together by mutually attractive and repulsive forces. These forces cause the molecule to both vibrate and rotate. Individual atoms vibrate with respect to each other while the molecule rotates around any spatial axis. Vibrational and rotational motion is quantized into states; transitions among these states give rise to vibrational and rotational spectra.

Transitions between electronic states require more energy than vibrational transitions, which also require more energy than rotational transitions. In the submil-

limetre, where this work is performed, photons only have sufficient energy to cause rotational transitions. In this section, the energy levels and spectrum of a rotating diatomic molecule are described.

In the rigid rotator model, a diatomic molecule is represented as two masses (m_1 and m_2) at distances (r_1 and r_2) from the centre of mass. The masses have a fixed separation and rotate about an axis perpendicular to the line joining the nuclei. For simplicity, these two masses can be treated as one with a reduced mass μ,

$$\mu = \frac{m_1 m_2}{m_1 + m_2}, \tag{2.1}$$

moving at a radius $r_e = (x^2 + y^2 + z^2)^{\frac{1}{2}}$ about the centre of mass of the system. The classical expression for the energy of this system is,

$$E = \frac{L^2}{2I}, \tag{2.2}$$

where $L = I\omega$ is the angular momentum, $\omega = 2\pi\nu$ is the rotation frequency, and I is the moment of inertia,

$$I = \mu r_e^2. \tag{2.3}$$

In quantum mechanics the rigid rotator can only exist in discrete energy states and these are found through the time independent Schrödinger wave equation,

$$-\frac{\hbar^2}{2\mu}\nabla^2\psi + V(x, y, z)\psi = E\psi, \tag{2.4}$$

where $\hbar = h/2\pi$, h is Planck's constant, μ is the reduced mass of the system, ψ is the time independent wave function, and $V(x, y, z)$ and E are the potential energy and energy of the system respectively. $V = 0$ in the rigid rotator model since the masses have a fixed separation; applying this to Eq. 2.4, expressed in spherical coordinates (θ, ϕ), gives the following wave equation,

$$\frac{1}{sin\,\theta}\frac{\partial}{\partial\theta}\left(sin\,\theta\frac{\partial\psi}{\partial\theta}\right) + \frac{1}{sin^2\theta}\frac{\partial^2\psi}{\partial\phi^2} + \frac{2\mu r_e^2}{\hbar^2}E\psi = 0, \tag{2.5}$$

(Hanel *et al.* 1992). The solutions to this wave equation are,

$$\psi_{JM} = \left[\frac{(2J+1)(J-|M|)!}{4\pi(J+|M|)!}\right]^{1/2} e^{iM\phi}P_J^{|M|}(cos\,\theta), \tag{2.6}$$

where J and M are the angular momentum quantum numbers ($J \geq 0, |M| \leq J$), and $P_J^{|M|}$ are the associated Legendre polynomials (Hanel *et al.* 1992). The corresponding energy for this system is,

$$E = \frac{\hbar^2}{2\mu r_e^2} J(J+1), \tag{2.7}$$

and angular momentum,

$$L = \hbar(J(J+1))^{\frac{1}{2}}, \tag{2.8}$$

(Hanel *et al.* 1992).

In the infrared and submillimetre, formulae are often expressed in terms of wavenumber $\widetilde{\nu}$ [cm^{-1}] rather than frequency ν [Hz] or wavelength λ [cm]. Wavenumber is related to frequency through the speed of light c in units of cm·s^{-1},

$$\nu = \frac{c}{\lambda} = c\widetilde{\nu}. \tag{2.9}$$

The energy of the system can be expressed in wavenumbers through the following relation,

$$E = hc\widetilde{\nu}. \tag{2.10}$$

Applying Eq. 2.10 to Eq. 2.7 results in an energy expression in units of cm^{-1},

$$F(J) = \frac{E}{hc} = BJ(J+1), \tag{2.11}$$

where,

$$B = \frac{h}{8\pi^2 c\mu r_e^2}. \tag{2.12}$$

To determine which transitions are allowed, the expectation value of the dipole moment is calculated,

$$R_{J'M'J''M''} = \int_{-\infty}^{\infty} \psi^*_{J'M'} \mathbf{M} \psi_{J''M''} d\theta d\phi, \tag{2.13}$$

where the dipole moment, the sum of the product of the charges q_i and the positions r_i of all the electrons and nuclei in the molecule, is given by,

$$\mathbf{M} = \sum_i q_i r_i, \tag{2.14}$$

(Hanel *et al.* 1992). This integral is only nonzero in the situation when $J' = J'' \pm 1$. Applying the selection rule of $\Delta J = 1$ the allowed transition wavenumbers are,

$$\begin{aligned} \widetilde{\nu} &= F(J+1) - F(J) \\ &= 2B(J+1), \end{aligned} \tag{2.15}$$

where J refers to the lower state. This indicates that the spectral lines will be spaced by 2B.

A detailed comparison between calculated and observed spectra shows that the rigid rotator model agrees reasonably well with the observed spectra, but there are some discrepancies. The discrepancies arise because a diatomic molecule cannot maintain a perfectly rigid structure as it rotates; it stretches slightly in response to centrifugal forces. When this effect is taken into account, the rotational energy levels are given by,

$$F(J) = \frac{E}{hc} = BJ(J+1) - DJ^2(J+1)^2, \tag{2.16}$$

where D is the centrifugal distortion constant (Hanel *et al.* 1992). The second term in Eq. 2.16 slightly lowers the energy level compared to the rigid rotator calculation.

Fig. 2.1 shows the pattern of transition lines that arise from purely rotational transitions in CO. The line being investigated in this work is the J=3–2 transition located at 11.5 cm^{-1} (in bold).

2.2 Radiative transfer

Radiative transfer is the process by which molecules in the atmosphere absorb, emit, and scatter electromagnetic radiation. Scattering can usually be neglected in submillimetre calculations because scattering particles are small in comparison to the wavelength of observation. Absorption and emission by atmospheric gases dominates the submillimetre spectrum.

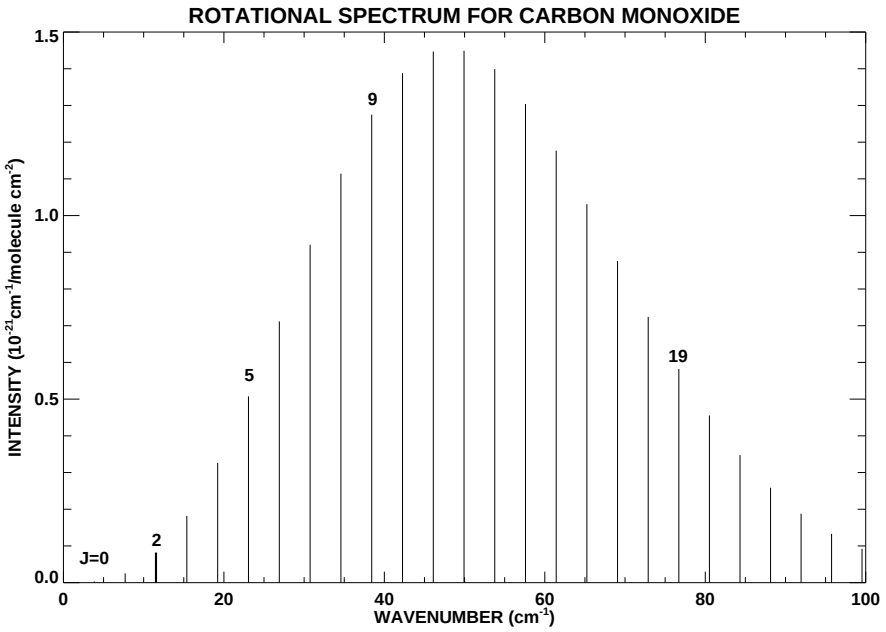

Figure 2.1: *The rotational spectrum of CO. The line intensities are for a temperature of 296 K. The rotational quantum number indicates the lower state of the transition (CO line data from HITRAN 2004; Rothman* et al. *2005).*

2.2.1 Single layer radiative transfer

The first step in developing the equation of radiative transfer is to consider a thin layer of atmosphere as shown in Fig. 2.2. Incident radiation $I(\nu)$ on the layer will be subject to absorption within the layer. The change in intensity due to absorption in the layer dI_a is given by,

$$dI_a(\nu) = -I(\nu)k(\nu)ndz, \tag{2.17}$$

where $k(\nu)$ is the absorption coefficient [$\mathrm{m}^2 \cdot \mathrm{molecule}^{-1}$], n is the number density of the absorbing molecule, and dz is the thickness of the layer. Eq. 2.17 can be rewritten as,

$$dI_a(\nu) = -I(\nu)k(\nu)du, \tag{2.18}$$

where du is the column density of the absorber [$\mathrm{molecule} \cdot \mathrm{m}^{-2}$]. Using the ideal gas law and the mole ratio of the absorber q_i, the absorber column density is expressed as,

$$du = \frac{q_i P}{k_b T} dz. \tag{2.19}$$

Integration of Eq. 2.18 produces the intensity of the transmitted radiation I_{tr},

$$I_{tr}(\nu) = I(\nu)e^{-k(\nu)u}. \tag{2.20}$$

The exponential in Eq. 2.20 is a measure of the transmittance of the layer and the exponent is defined as the optical depth τ,

$$\tau(\nu) \equiv k(\nu)u, \tag{2.21}$$

(de Pater and Lissauer 2001).

The layer of atmosphere in Fig. 2.2 will also emit radiation; by analogy with Eq. 2.17 the emission is expressed as,

$$dI_e(\nu) = k(\nu)J(\nu)ndz = k(\nu)J(\nu)du, \tag{2.22}$$

where $J(\nu)$ is the source function. If the layer is assumed to be surrounded by a perfectly insulating enclosure which maintains the particles in the layer at a constant temperature T, the layer is said to be in thermodynamic equilibrium. In this

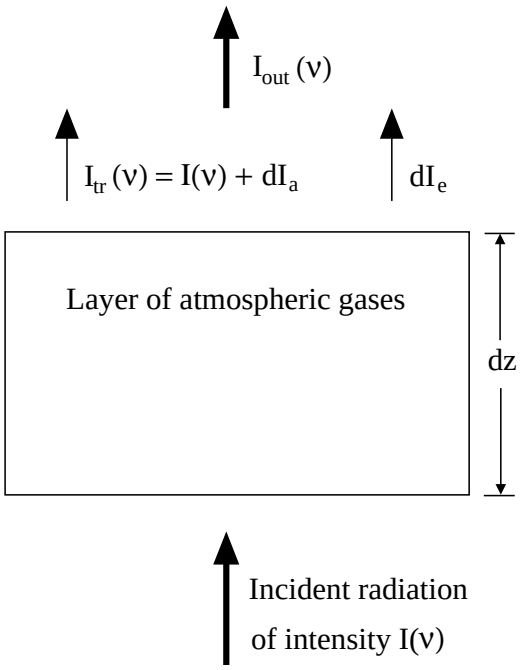

Figure 2.2: *Absorption and emission of radiation by an atmospheric layer.*

situation, the source function is given by the Planck function (de Pater and Lissauer 2001). The Planck function describes the continuous spectrum of a blackbody radiator and is given by,

$$B(\nu, T) = \frac{2h\nu^3}{c^2(e^{h\nu/k_bT} - 1)}, \tag{2.23}$$

where $B(\nu, T)$ is the intensity of radiation from a blackbody at temperature T and frequency ν [$\mathrm{W \cdot m^{-2} \cdot Hz^{-1} \cdot sr^{-1}}$] (Hanel *et al.* 1992). If the insulating enclosure is removed, thermodynamic equilibrium no longer exists because the matter in the layer will be subject to external radiation. The emission from the layer depends on the dominant process in the layer; either emission produced through absorption of incident radiation by molecules, or emission as a result of collisions between the molecules. Emission due to collisions between molecules dominates in regions of the atmosphere where the molecular density is high (troposphere and stratosphere). The temperature in the layer depends only on the energy available through collisions and the layer is said to be in Local Thermodynamic Equilibrium (LTE). In this situation, the Planck function is once again a valid representation of the source function (Hanel

et al. 1992).

The change in intensity due to absorption and emission in the layer can therefore be expressed as,

$$dI_a = -I(\nu)d\tau \quad \text{(absorption)}, \tag{2.24}$$

$$dI_e = B(\nu,T)d\tau \quad \text{(emission)}, \tag{2.25}$$

where $d\tau$ is the layer optical depth. The outgoing intensity of the layer is expressed as,

$$I_{out}(\nu) = I(\nu) + dI_a(\nu) + dI_e(\nu). \tag{2.26}$$

Substituting Eq. 2.24 and Eq. 2.25 into Eq. 2.26 and rearranging gives,

$$\begin{aligned} I_{out}(\nu) - I(\nu) &= -I(\nu)d\tau + B(\nu,T)d\tau \\ \frac{dI}{d\tau}(\nu) &= B(\nu,T) - I(\nu), \end{aligned} \tag{2.27}$$

which is known as the Schwarzschild equation and describes how the intensity of radiation changes due to the optical depth. Eq. 2.27 can be integrated using the integrating factor e^{τ} to find,

$$I_{out}(\nu) = I(\nu)e^{-\tau} + B(\nu,T)(1 - e^{-\tau}), \tag{2.28}$$

where the first term is the intensity transmitted through the layer and the second term the intensity emitted by the layer (de Pater and Lissauer 2001). The outgoing intensity in Eq. 2.28 is for radiation propagating at normal incidence in the atmosphere. When the emission angle of the radiation is taken into account Eq. 2.28 becomes,

$$I_{out}(\nu) = I(\nu)e^{-\tau/\mu} + B(\nu,T)(1 - e^{-\tau/\mu}), \tag{2.29}$$

where $\mu = cos(\theta)$ is the emission angle (de Pater and Lissauer 2001).

2.2.2 Multi-layer model

The outgoing intensity due to a single thin layer (Eq. 2.29) can be repeatedly applied to an atmosphere divided into n thin layers in each of which the temperature T_i, pressure P_i, and optical depth τ_i are known (Fig. 2.3).

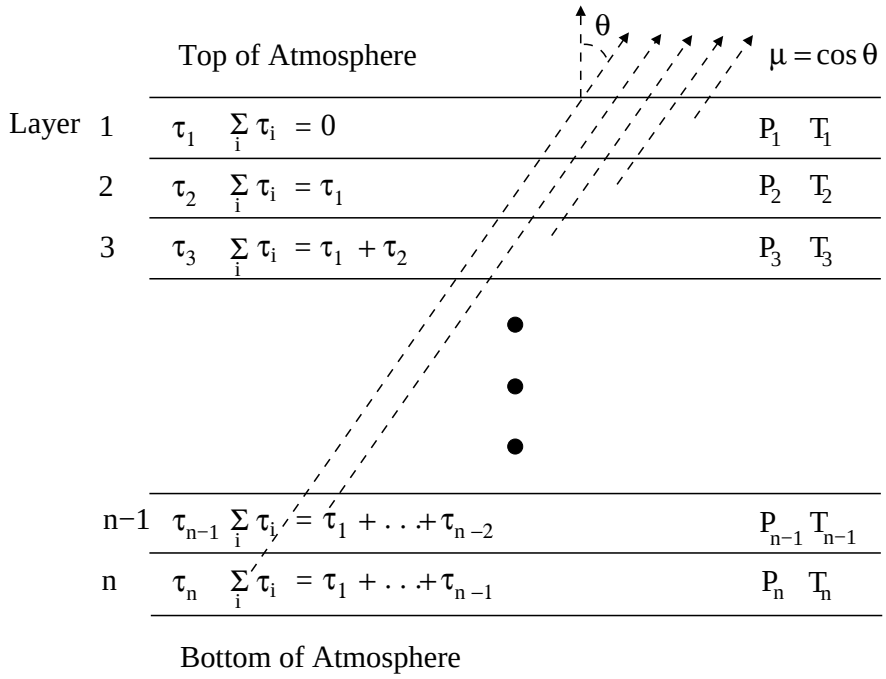

Figure 2.3: *Setup of the plane parallel atmosphere used in calculating the Neptune model.*

In the bottom layer, the emission will dominate over the transmission indicating that the first term of Eq. 2.29 is negligible. The outgoing intensity I_n from layer n will therefore be given by,

$$I_n(\nu, \mu) = B(\nu, T_n)(1 - e^{-\tau_n/\mu}), \tag{2.30}$$

where $B(\nu, T_n)$ is the Planck function for the layer at temperature T_n, and τ_n is the optical depth of layer n. The outgoing intensity from layer $n-1$ is composed of the transmission of the emission from layer n and the emission from layer $n-1$ to give,

$$I_{n-1}(\nu, \mu) = I_n(\nu, \mu)e^{-\tau_{n-1}/\mu} + B(\nu, T_{n-1})(1 - e^{-\tau_{n-1}/\mu}). \tag{2.31}$$

Substituting Eq. 2.30 into Eq. 2.31 gives,

$$I_{n-1}(\nu, \mu) = B(\nu, T_n)(1 - e^{-\tau_n/\mu})e^{-\tau_{n-1}/\mu} + B(\nu, T_{n-1})(1 - e^{-\tau_{n-1}/\mu}). \tag{2.32}$$

Eq. 2.29 is repeatedly applied to all of the layers until the top layer is reached. At layer 1 the outgoing intensity is given by,

$$I_1(\nu, \mu) = I_2(\nu, \mu)e^{-\tau_1/\mu} + B(\nu, T_1)(1 - e^{-\tau_1/\mu}). \tag{2.33}$$

Substituting the outgoing intensity from layer 2 gives the outgoing intensity at the top of the atmosphere,

$$\begin{aligned} I_1(\nu,\mu) &= B(\nu,T_n)(1-e^{-\tau_n/\mu})e^{-(\tau_{n-1}+\cdots+\tau_1)/\mu} + \\ & \quad B(\nu,T_{n-1})(1-e^{-\tau_{n-1}})e^{-(\tau_{n-2}+\cdots+\tau_1)/\mu} + \\ & \quad \cdots + \\ & \quad B(\nu,T_2)(1-e^{\tau_2/\mu})e^{-\tau_1/\mu} + \\ & \quad B(\nu,T_1)(1-e^{-\tau_1/\mu}), \end{aligned} \tag{2.34}$$

which can be expressed as,

$$I(\nu,\mu) = \sum_{i=1}^{n} B(\nu,T_i)\left(1-e^{-\frac{\tau_i}{\mu}}\right)\exp\left(-\frac{1}{\mu}\sum_{j=1}^{i-1}\tau_j\right), \tag{2.35}$$

(Hanel *et al.* 1992).

The Neptune CO model was calculated using a line-by-line, plane-parallel radiative transfer code written using the Interactive Data Language (IDL®). The model atmosphere was composed of 152 layers (P_i, T_i) in each of which the Planck function $B(\nu, T_i)$ (Eq. 2.23) and the layer optical depth τ_i were calculated (Fig. 2.3). The layer optical depth was calculated in two parts, CO line and continuum, and then combined to give the total layer optical depth,

$$\tau_i = \tau_i^{CO} + \tau_i^{cont}, \tag{2.36}$$

where τ_i^{CO} and τ_i^{cont} are the layer optical depths due to the CO line and continuum respectively.

2.2.3 CO opacity

The CO line optical depth was calculated using the CO column density and absorption coefficient,

$$\Delta u_{CO} = \frac{q_{CO}P}{k_b T}\Delta z, \tag{2.37}$$

$$\tau_{CO} = k_{CO}\Delta u_{CO}. \tag{2.38}$$

The absorption coefficient k_{CO} is the product of line strength, S, and line shape, f,

$$k_{CO}(\nu) = Sf(\nu), \tag{2.39}$$

where line strength is the spectrally integrated cross section (§2.2.4),

$$S = \int_0^\infty k_{CO}(\nu)d\nu, \tag{2.40}$$

and the line shape function determines the frequency dependence of a spectral feature around the central frequency of the line (§2.2.5).

2.2.4 Line strength

The strength of a spectral line is proportional to the number of molecules in the lower state and the probability of transition at that frequency. Rothman *et al.* (1998) define the line strength as,

$$S(T_0) = \frac{8\pi^3}{3hc^2}\nu_0 \frac{I_a g'' exp(-E''/k_b T_0)}{Q(T_0)} \left[1 - exp(-h\nu_0/k_b T_0)\right] |R_{J'M'J''M''}|^2, \tag{2.41}$$

where T_0 is the reference temperature, ν_0 is the transition frequency, I_a is the isotopic abundance, g'' and E'' are respectively the degeneracy and energy of the lower state, and $|R_{J'M'J''M''}|^2$ is the square of the electric dipole moment matrix (Eq. 2.13). The partition function $Q(T_0)$ is given by,

$$Q(T_0) = \sum_{n=0}^{\infty} g_n e^{-E''_n/k_b T_0}, \tag{2.42}$$

which is the sum of the Boltzmann factors ($e^{-E''_n/k_b T_0}$) weighted by their degeneracies (Hanel *et al.* 1992) .

Calculation of the electric dipole moment matrix is difficult, so line strengths are usually determined experimentally and catalogued in a database such as HITRAN (Rothman *et al.* 1998). In this catalogue, line strengths are tabulated at a reference temperature of 296 K and corrected for temperature using the following relation,

$$S(T) = S(T_0)\left(\frac{T_0}{T}\right)^m \left[\frac{exp\left(-\frac{E''}{k_b T}\right)}{exp\left(-\frac{E''}{k_b T_0}\right)}\right] \left[\frac{1 - exp\left(-\frac{h\nu_0}{k_b T}\right)}{1 - exp\left(-\frac{h\nu_0}{k_b T_0}\right)}\right], \tag{2.43}$$

where $m = 1$ for linear molecules (Rothman *et al.* 1998).

2.2.5 Line shape

Transitions do not produce infinitely narrow lines; each line has a shape associated with it. The line shape determines the frequency dependence around the central line position. Several mechanisms are responsible for causing the line to be spread over a frequency range: natural line broadening results from quantum mechanical principles; collision and Doppler broadening arise because of the environment the molecule is located in.

Natural line broadening arises from the Heisenberg uncertainty principle which states that it is not possible to absolutely determine the position and momentum of a particle simultaneously,

$$\Delta x \Delta p \geq \frac{\hbar}{2}, \tag{2.44}$$

where Δx and Δp are the uncertainties in the position and momentum respectively (Brehm and Mullin 1989). An alternative expression of this principle involves the uncertainty in energy ΔE and time Δt

$$\Delta E \Delta t \geq \frac{\hbar}{2}. \tag{2.45}$$

Applying $E = h\nu$ indicates that the uncertainty in the line centre is inversely proportional to the lifetime of the state,

$$\Delta \nu \sim \frac{1}{\Delta t}. \tag{2.46}$$

This indicates that as the excited state lifetime becomes shorter, the line will broaden. In the submillimetre, where rotational transitions dominate and lifetimes are long in comparison to electronic transitions, natural line broadening has little effect. This is true except for transitions that arise due to collision-induced dipoles; in this situation dipoles exist for short periods which result in very broad lines.

Line broadening due to the environment dominates the submillimetre spectrum. In collisional broadening (also known as pressure broadening), the mean lifetime of the excited state is reduced because of collisions between molecules. This process results in a Lorentzian line shape,

$$f(\nu) = \frac{1}{\pi} \frac{\alpha_L}{\alpha_L^2 + (\nu - \nu_0)^2}, \tag{2.47}$$

where ν_0 is the central frequency, and α_L is the Lorentz halfwidth (Hanel *et al.* 1992). α_L is proportional to the atmospheric pressure and defined as,

$$\alpha_L = [\alpha_s q_{CO} + \alpha_a(1 - q_{CO})] \left[\frac{P}{P_0}\right] \left[\frac{T_0}{T}\right]^n, \tag{2.48}$$

where α_s and α_a are the self-broadened and air-broadened halfwidths respectively, T_0 and P_0 are the reference temperature and pressure ($T_0 = 296$ K, $P_0 = 1$ atm), and n is the coefficient of temperature dependence. α_s, α_a, and n are quantities that are measured in the lab and tabulated in a database such as HITRAN (Rothman *et al.* 1998). The values used for this CO line are discussed in §2.3.2.

Doppler broadening of a spectral line results from the thermal motion of a gas. In this situation, molecules moving at a line-of-sight velocity v will exhibit a different transition frequency than those at rest. The frequency shift that results is given by,

$$\Delta\nu = \frac{v}{c}\nu_0, \tag{2.49}$$

where ν_0 is the rest transition frequency. The line-of-sight velocity components have a Maxwellian distribution which results in a Gaussian line shape,

$$f(\nu) = \frac{1}{\alpha_D}\sqrt{\frac{ln\ 2}{\pi}} e^{-ln\ 2(\nu-\nu_0)^2/\alpha_D^2}, \tag{2.50}$$

where α_d is the Doppler halfwidth which depends on the temperature T and molecular weight M of the gas,

$$\alpha_D = \frac{\nu_0}{c}\sqrt{\frac{2ln\ 2\ k_b T}{M/N_a}}, \tag{2.51}$$

and N_a is Avogadro's number (Hanel *et al.* 1992).

When the line profile is completely resolved by the spectrometer, collisional (pressure) and Doppler broadening must both be considered. This requires the convolution of the Gaussian and Lorentz line shapes to produce the Voigt line shape,

$$f(\nu) = \frac{1}{\alpha_D}\sqrt{\frac{ln\ 2}{\pi}} K(x, y), \tag{2.52}$$

where $K(x, y)$ is the Voigt function given by,

$$K(x, y) = \frac{y}{\pi}\int_{-\infty}^{+\infty} \frac{e^{-t^2}}{y^2 + (x - t)^2} dt, \tag{2.53}$$

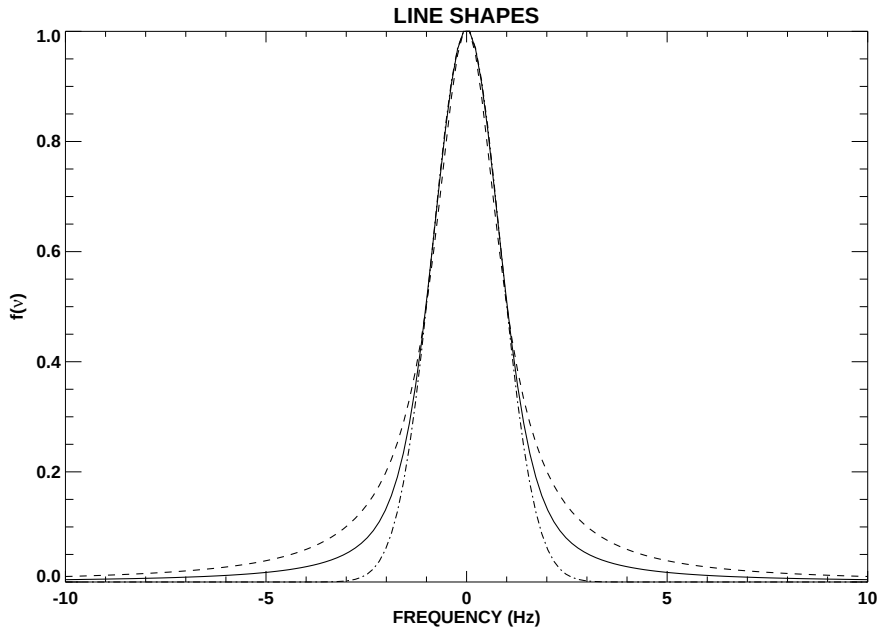

Figure 2.4: *The collision (dashed), Voigt (solid), and Doppler (dash-dot) line shape profiles. All three have been normalized to the same maximum amplitude and halfwidth half-maximum.*

where,

$$x \equiv \frac{\nu - \nu_0}{\alpha_D}\sqrt{ln\,2}, \tag{2.54}$$

$$y \equiv \frac{\alpha_L}{\alpha_D}\sqrt{ln\,2}, \tag{2.55}$$

(Armstrong 1967). Fig. 2.4 compares the collisional, Doppler and Voigt line shapes. The high-resolution heterodyne spectroscopy measurements performed for this project required the Voigt line shape to be used. The IDL® Voigt function was used in computing this line shape because execution time was not a dominant constraint in the radiative transfer model code.

2.2.6 Continuum opacity

Neptune's composition is dominated by H_2 and He which have no permanent dipole moments and should not exhibit electric dipole transitions. At high pressures and long path length, however, electric dipole absorption is observed. The absorption

results when two species collide and induce a transient dipole; during this time transitions among vibrational, rotational, and translational states take place. The dipole arises because the electron distribution is distorted during the collision. This process is important in Neptune's atmosphere because collision-induced absorption of H_2–H_2, H_2–He, and H_2–CH_4 dominate the far-infrared spectrum.

The spectral width $\Delta\nu$ of these collision-induced features is related to the collision time through Eq. 2.46. In this situation, Δt is very short ($< 10^{-12}$ s) indicating that these features are extremely broad (Hanel *et al.* 1992). Fig 2.5 shows the measured (+ marks) and calculated (solid line) collision-induced spectrum of H_2-H_2 from 0 to 2000 cm^{-1} (0 to 60 THz) (Bachet *et al.* 1983). The collision-induced H_2-H_2 spectrum is dominated by the J=0–2 and J=1–3 rotational transitions; at low wavenumbers a translational band also contributes.

A full quantum mechanical formalism is required for a correct description of the line shapes, positions, and strengths of these transitions. This type of calculation is cumbersome and not practical for wide use. Development of empirical line shape functions has, therefore, resulted. These are used to approximate the measured spectrum from collision-induced transitions (e.g. Borysow *et al.* 1985).

The absorption coefficients due to the collision-induced transitions of H_2–H_2, H_2–He, and H_2–CH_4 were calculated using the algorithms of Borysow *et al.* (1985), Borysow and Frommhold (1988), and Borysow and Frommhold (1986) respectively. The continuum optical depth was calculated using the H_2 column density and the absorption coefficients due to the H_2–H_2, H_2–He, and H_2–CH_4 collisions,

$$\Delta u_{H_2} = \frac{q_{H_2} P}{k_b T} \Delta z, \tag{2.56}$$

$$\tau_{cont} = (k_{H_2H_2} + k_{H_2He} + k_{H_2CH_4}) \Delta u_{H_2}. \tag{2.57}$$

2.2.7 Model geometry

Neptune is unresolved by the diffraction-limited beam of the JCMT (14″ at this frequency). Integration of the outgoing intensity over the visible hemisphere of the planet was therefore required. This was accomplished by dividing the visible disk

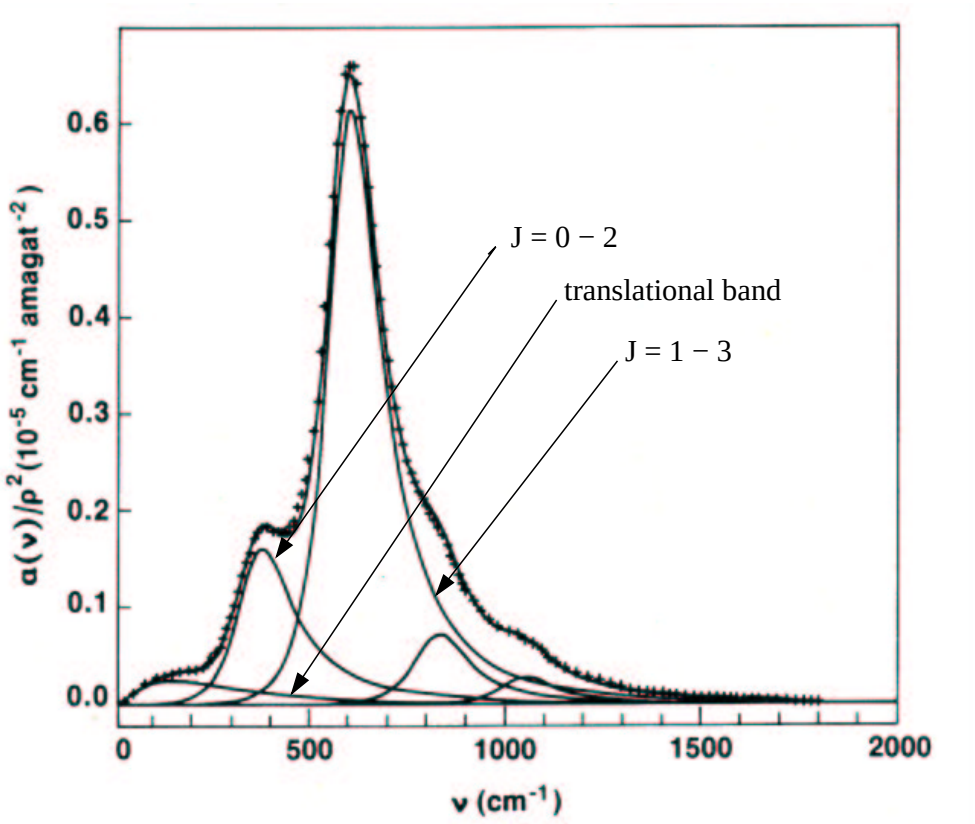

Figure 2.5: *The collision-induced spectrum of H_2 at a temperature of 195 K. Experimental data are shown in + marks while the calculated spectrum is the solid line. The individual spectral lines that dominate this spectrum are labelled (Bachet* et al. *1983).*

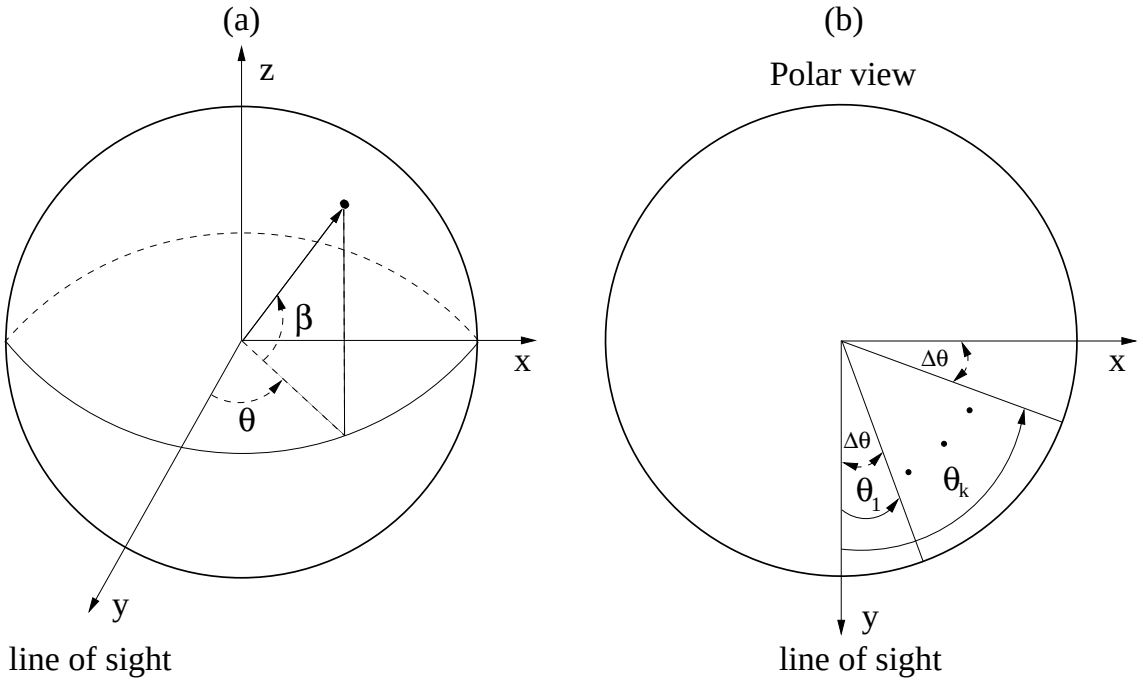

Figure 2.6: *Geometry for the Neptune model. In (a) the position of a point on Neptune is defined by the coordinates θ (longitude) and β (latitude); (b) shows a polar view of Neptune's disk divided into rings.*

of Neptune into 25 rings. Fig. 2.6 shows the geometry used in this calculation. In (a) θ is the longitude from the central meridian and β is the latitude; (b) shows the division of Neptune's disk into rings. Each ring had to be further divided into 100 equal-area segments (Fig. 2.7) when high-resolution ($\Delta\nu < 1.25$ MHz) calculations were required. This was needed to account for the line broadening resulting from the rotational velocity of Neptune.

To determine the line broadening, the line-of-sight component of the rotational velocity V, within each segment, was considered to be constant and given by,

$$V = V_{eq} sin(\theta) cos(\beta), \tag{2.58}$$

where V_{eq} is the velocity at the equatorial limb (2.68 km/s). The intensity spectrum (Eq. 2.35) was shifted to higher or lower frequencies depending on the sign and magnitude of V (Eq. 2.58). The segment intensities were then combined to give an

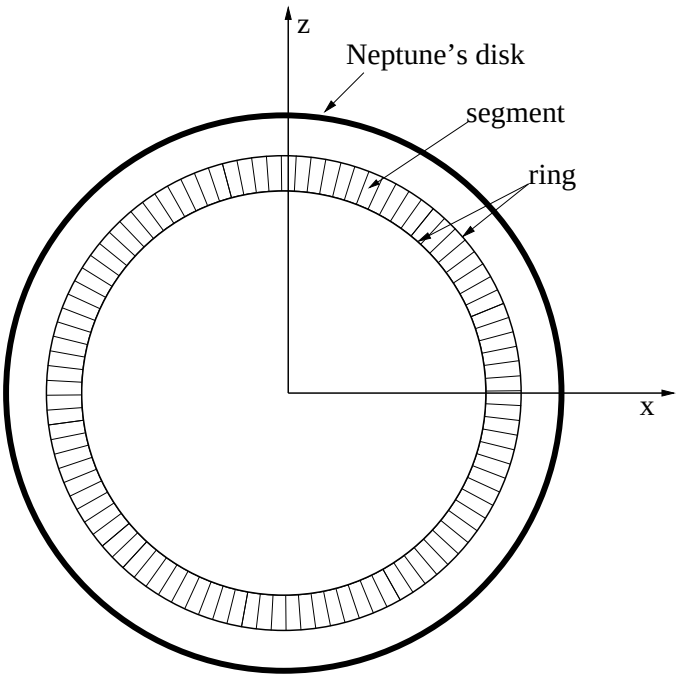

Figure 2.7: *The geometry used for calculating the line broadening. This example shows one of 25 rings divided into 100 equal-area segments.*

intensity for each ring,

$$I_{ring}(\nu,\mu) = \frac{1}{A_{ring}} \sum_{l=1}^{100} I_l(\nu,\mu) A_l, \tag{2.59}$$

where $I_l(\nu,\mu)$ is the frequency-shifted intensity of each segment in the ring with emission angle μ, A_l is the area of each segment, and A_{ring} is the total area of the ring. The segments were of equal area, allowing Eq. 2.59 to be re-written as,

$$I_{ring}(\nu,\mu) = \frac{1}{100} \sum_{l=1}^{100} I_l(\nu,\mu) = \overline{I_l(\nu,\mu)}. \tag{2.60}$$

This produces a rotationally-broadened intensity spectrum for each ring of the planet.

The ring intensities were combined using a weighted sum to produce the final outgoing intensity,

$$I_N(\nu) = 2 \sum_{k=1}^{25} I_{ring}(\nu,\mu_k) sin\theta_k cos\theta_k \Delta\theta, \tag{2.61}$$

where $I_{ring}(\nu,\mu_k)$ is the rotationally-broadened intensity in each ring k (Eq. 2.60). Fig. 2.8 shows the result of introducing this effect into the model. A line broadening of approximately 2 MHz was observed in the final spectrum.

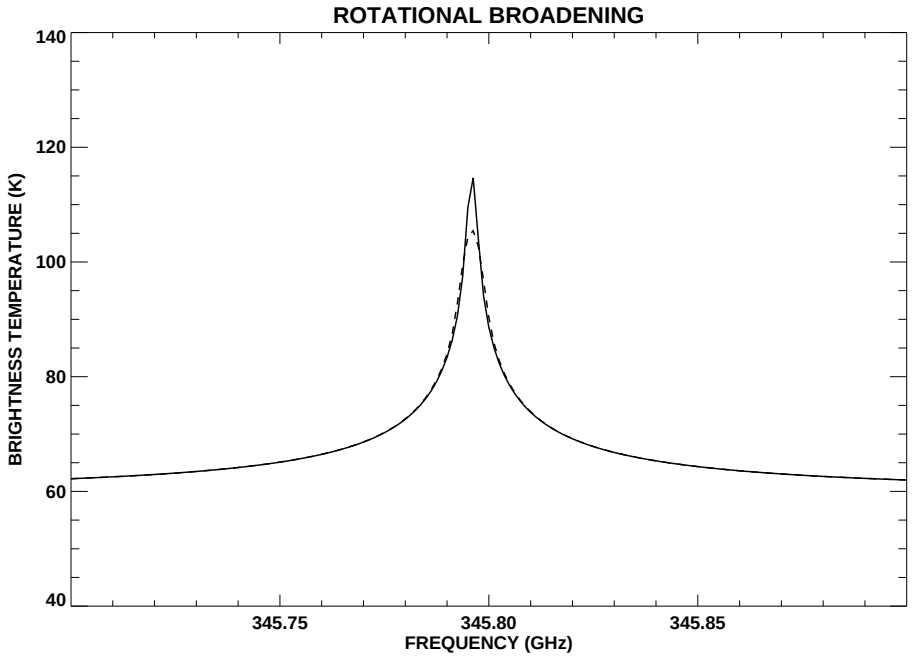

Figure 2.8: *The CO J=3–2 model of Neptune taking into account rotational broadening (dashed), and without rotational broadening (solid).*

Integration of the outgoing intensity over the visible hemisphere was sufficiently calculated using 25 rings; increasing the number of rings did not produce improved intensity results. The further division of the rings into 100 equal-area segments, to account for rotational broadening, produced equivalent broadening results to that found by Marten *et al.* (2005).

2.3 Model input parameters

2.3.1 Temperature profile

The temperature structure assumed for the radiative transfer calculations (Fig. 2.9) is identical to the temperature profile of Burgdorf *et al.* (2003) at pressures higher than 10^{-3} bar (see §1.3.2). At pressures lower than $1x10^{-3}$ bars the temperature structure follows that used by Marten *et al.* (1993) (see §1.3.4).

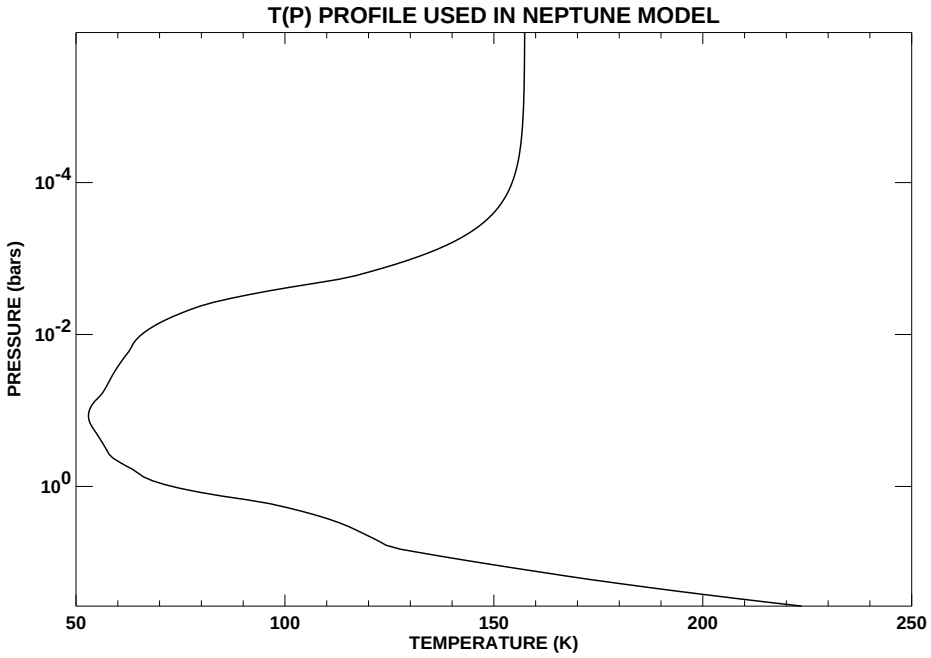

Figure 2.9: *The temperature profile of Neptune used in the CO line model (Burgdorf* et al. *2003, Marten* et al. *1993).*

2.3.2 CO line parameters

The CO line opacity was calculated using line parameters from the HITRAN molecular line catalogue, 2004 edition (Rothman *et al.* 2005). Table 2.1 lists the CO line parameters, and their associated errors, used in this model. The JPL molecular line catalogue (Pickett *et al.* 1998) was also accessed, but did not provide all of the parameters required for this calculation.

2.3.3 Abundances of atmospheric constituents

The two most abundant species in the model are H_2 and He, with mole ratios of $q_{H_2} = 83.1^{+1.7}_{-2.2}\%$ and $q_{He} = 14.9^{+1.7}_{-2.2}\%$ (Burgdorf *et al.* 2003). Methane is present, but its abundance is constrained by condensation due to the low temperatures found at the tropopause. Baines *et al.* (1995) determined the tropospheric value to be $q^{trop}_{CH_4} = 2.2^{+0.5}_{-0.6}\%$. This is consistent with a wet adiabatic lapse rate matching far-infrared photometry (Orton *et al.* 1986). The strong convection on Neptune allows

Table 2.1: *HITRAN 2004 CO line parameters*

Line Parameter	Value	Error
Central wavenumber ($\widetilde{\nu_0}$)	11.534513 cm^{-1}	≥ 0.00001 and < 0.0001 cm^{-1}
Lower state energy (E″)	11.534953404 cm^{-1}	$\pm 2x10^{-9}$ cm^{-1}
Line strength (S(T_0))	$8.210x10^{-23}$ cm^{-1}/molecule·cm^{-2}	$< 1\%$
Air-broadened halfwidth (α_a)	0.0709 $cm^{-1}atm^{-1}$	$\pm 1.3\%$
Self-broadened halfwidth (α_s)	0.0785 $cm^{-1}atm^{-1}$	$\pm 2.5\%$
Coefficient of temperature dependence (n)	0.740	$\pm 2.7\%$

methane to reach altitudes above its condensation level by convective penetration, producing a stratospheric abundance higher than would normally result from following the vapour pressure profile. A value of $q_{CH_4}^{strat} = 0.13 \pm 0.08\%$ was assumed for the stratospheric abundance (B. Bézard, personal communication, Orton *et al.* 1986). Between the tropospheric and stratospheric abundances the methane profile is limited by condensation (Eq. 1.12).

2.4 Neptune model results

The radiative transfer model of §2.2 produces a spectrum of outgoing intensity I as a function of frequency ν (Eq. 2.61). It is common to express the intensity in terms of the brightness temperature. The latter is also a function of frequency and is defined as the temperature of a blackbody, at each frequency, which would emit the same intensity. The relationship between the two quantities is described by the Planck function.

The spectra in Fig. 2.10 were calculated using the Neptune model for a selection of CO abundances. The abundance was assumed, for illustrative purposes, to be uniform with altitude. The CO line is composed of two parts: the emission from the upper stratosphere, and the broad absorption from the troposphere and lower stratosphere. The regions of the atmosphere that form these components of the line are determined through examination of the contribution functions.

Eq. 2.35 gives the sum of the emission at each pressure level attenuated by the transmission of the levels above it for all pressure levels in the model atmosphere. Both the opacity (τ) and the Planck function (B) are temperature and frequency dependent; therefore, each frequency and pressure level will contribute different amounts to the final outgoing intensity. At a particular frequency ν and an emission angle of $\mu = 1$ the intensity C_i that pressure level i contributes to the outgoing intensity I is determined by calculating Eq. 2.35 at pressure level i,

$$C_i(\nu) = B(\nu, T_i) \left[exp \left(- \sum_{j=1}^{i-1} \tau_j(\nu) \right) \right] \left[1 - e^{-\tau_i(\nu)} \right], \tag{2.62}$$

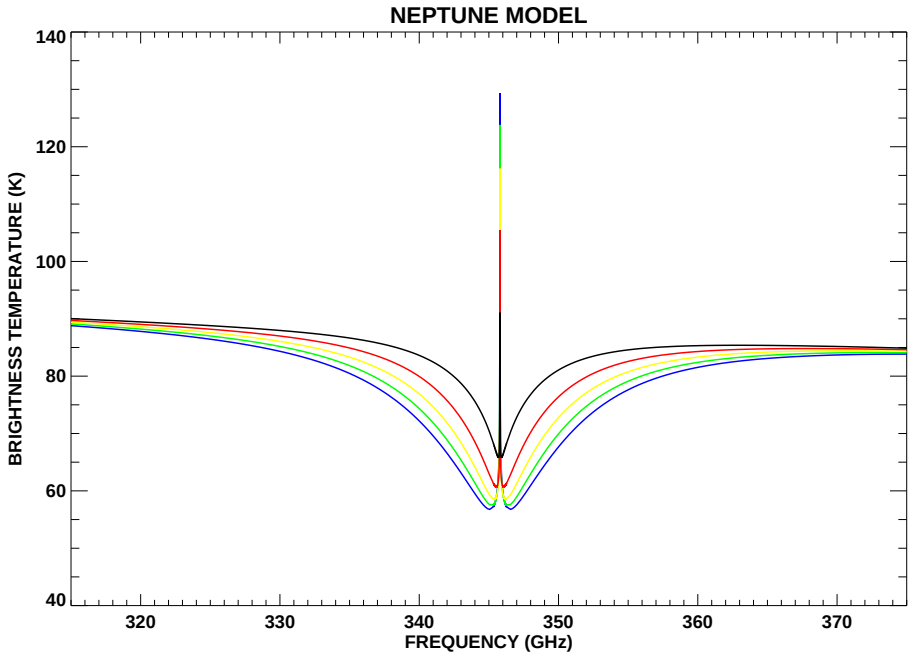

Figure 2.10: *The Neptune CO line model for constant CO distributions;* 0.5x10^{-6} *(black),* 1.0x10^{-6} *(red),* 1.5x10^{-6} *(yellow),* 2.0x10^{-6} *(green),* 2.5x10^{-6} *(blue).*

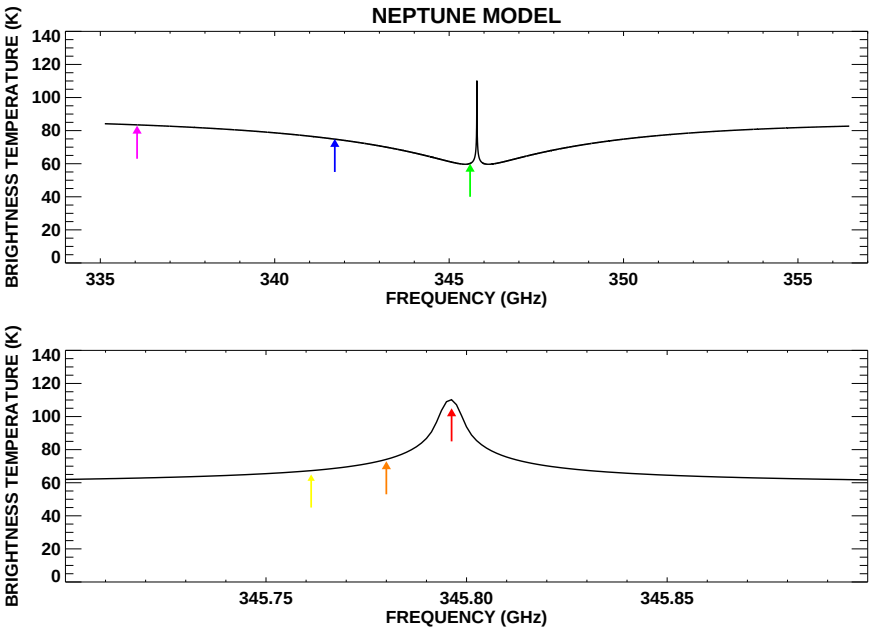

Figure 2.11: *The Neptune CO line model for a constant CO mole ratio of* $1.0\text{x}10^{-6}$ *indicating the frequencies used to calculate the contribution functions shown in Fig. 2.12.*

(Hanel *et al.* 1992). Calculation of Eq. 2.62 at each pressure level in the model atmosphere allows the contribution, at a particular frequency, to be examined, but does not take into account the effect of rotational broadening. A series of contribution functions, for the frequencies labelled in Fig. 2.11, are shown in Fig. 2.12. The contribution from the central frequency of the line (red curve) peaks in the stratosphere and, as the frequency moves away from line centre, peaks at higher pressures. At frequencies less than ∼335 GHz and greater than ∼355 GHz the contribution functions peak in the continuum forming region of the atmosphere at a pressure and temperature of approximately 2 bar and 90 K respectively.

2.5 Calibrators

Observations of Neptune using the FTS and SCUBA required calibration against an astronomical target. There were three criteria used for selecting a calibrator:

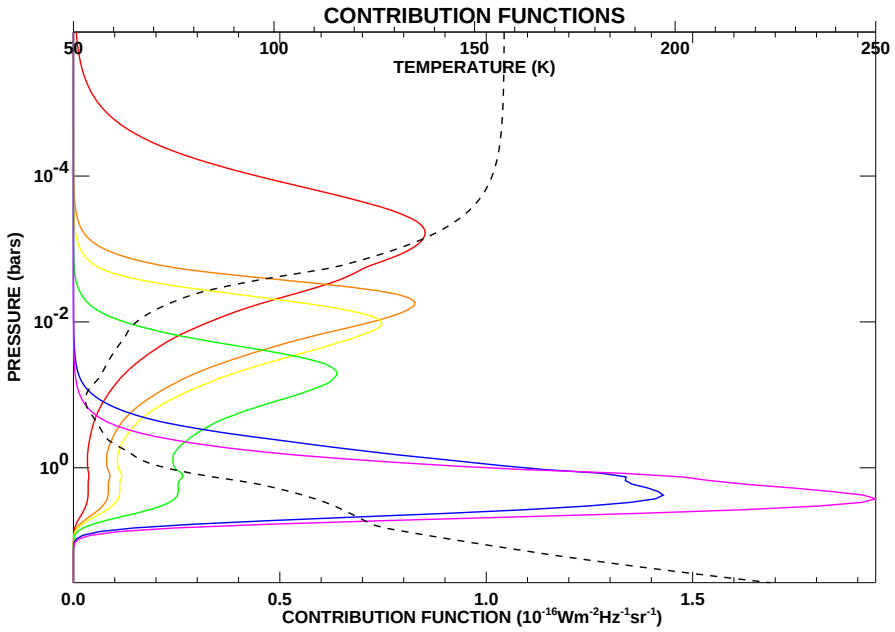

Figure 2.12: *The contribution functions for frequencies of the J=3–2 CO line shown in Fig. 2.11; 345.796 GHz (red), 345.780 GHz (orange), 345.761 GHz (yellow), 345.601 GHz (green), 341.722 GHz (blue), 336.054 GHz (violet). The temperature profile is shown as the dashed curve.*

1. The source must be amenable to spectral modelling,

2. CO absorption must not be measurable by the instrument being used and,

3. It must be a point source.

Two planets were selected: Uranus and Mars. These planets and their models will be briefly discussed.

2.5.1 Uranus

Uranus was a good candidate for a calibration target because of its similar angular size to Neptune (3.6″ compared to 2.3″), the ease in modelling its atmosphere, and the inability of Marten *et al.* (1993) to detect CO in its atmosphere.

Uranus is very different from the other Jovian planets because of its large obliquity of 97.86° and low internal heat flux. It has been postulated that its obliquity was caused by a collision with a large planetesimal, and the density gradients that resulted have inhibited convection in the interior. This may be the cause of its low internal heat flux (see §1.2, de Pater and Lissauer 2001).

The Uranus model is identical to the Neptune model except for the temperature profile and mole ratios of its atmospheric constituents. The temperature profile, shown in Fig. 2.13, was derived from the radio refractivity profile measured by the RSS experiment on Voyager when it visited Uranus in 1986 (Lindal *et al.* 1987). Uranus' profile has many similarities to Neptune's; for instance, the temperature inversion on Uranus is due to absorption of solar radiation by CH_4. Uranus' stratosphere, however, shows significant structure in comparison to Neptune's. Lindal *et al.* suggest that the vertical structure on Uranus is due to heating by C_2H_6 and C_2H_2 hazes.

Lindal *et al.* (1987) used the derived temperature profile of Uranus with IRIS data to determine H_2 and He mole ratios of $q_{H_2} = 85 \pm 3\%$ and $q_{He} = 15 \pm 3\%$. These values were determined for the stratosphere where CH_4 does not contribute to the mean molecular weight. When these values are scaled for the lower troposphere, where CH_4 exists, the mole ratios become $q_{H_2} = 83.0\%$ and $q_{He} = 14.7\%$.

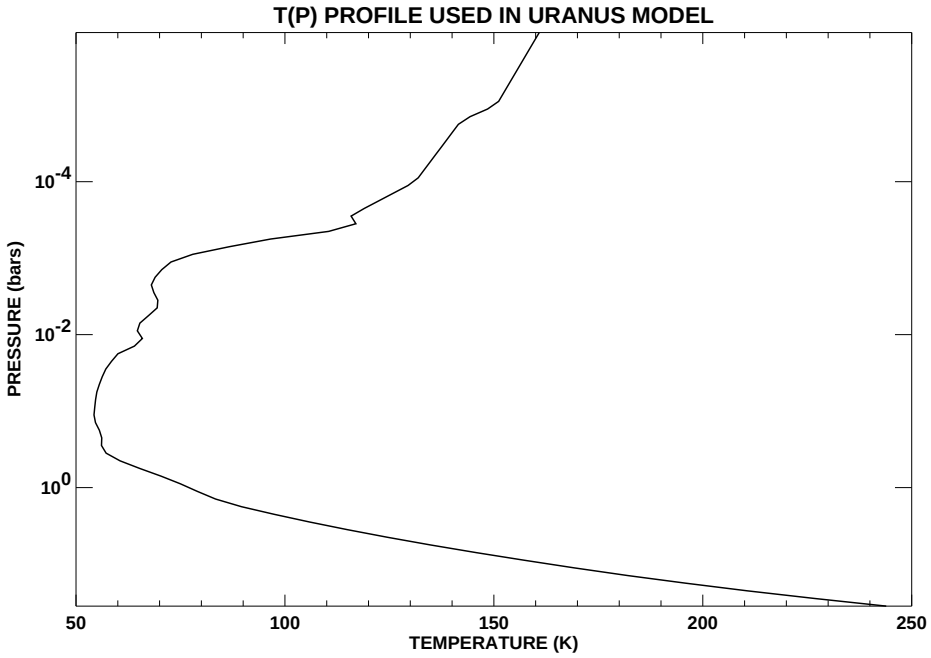

Figure 2.13: *The temperature profile of Uranus used in the model (Lindal* et al. *1987).*

The tropospheric methane mole ratio was determined by Orton *et al.* (1986) and Griffin and Orton (1993) using radiative transfer modelling of submillimetre and millimetre thermal emission measurements to find a $q^t_{CH_4} = 2.3\%$. The stratospheric methane mole ratio was determined by Orton *et al.* (1987) using mid-infrared spectra to set an upper limit of 0.001%, indicating that convective penetration (§1.4.2) is not significant on Uranus. The CH_4 mole ratio profile used in this model is constant in the troposphere, with a value of 2.3%, until it reaches the saturation layer; at that point the CH_4 abundance profile follows the vapour pressure curve (Eq. 1.12).

The above parameters and a CO mole ratio of 0 were used to create the Uranus model shown in Fig. 2.14.

2.5.2 Mars

Mars has a rocky surface composed mostly of silica, calcium carbonate, and iron oxides. It has global asymmetry in that half the planet (southern hemisphere) is

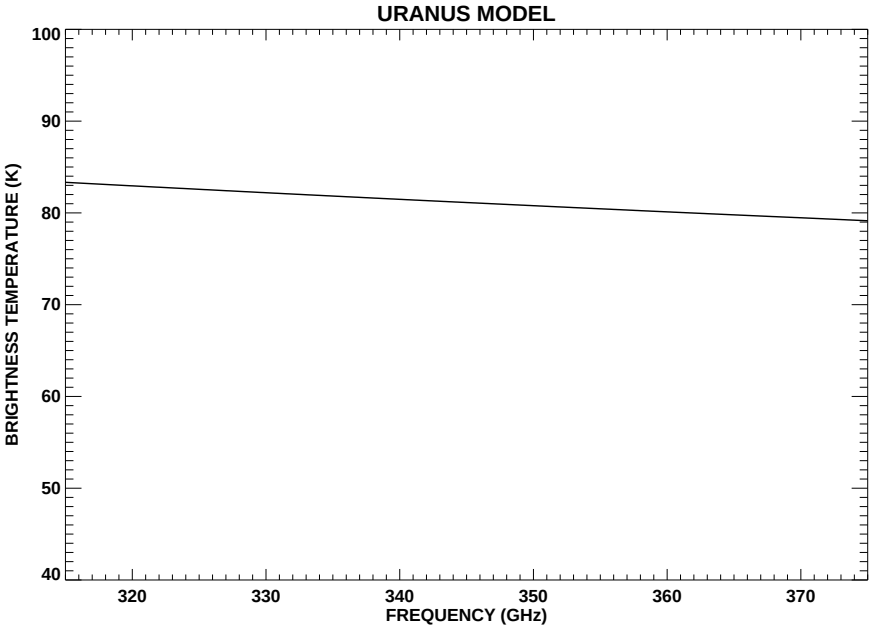

Figure 2.14: *The Uranus model.*

heavily cratered and elevated 1–4 km above the nominal surface level; the northern hemisphere is relatively smooth and lies at or below the nominal level. Mars has an average surface pressure of 6 mbar and a mean surface temperature of 215 K. The low atmospheric pressure, obliquity (25.19°), and eccentric orbit ($e = 0.093$) cause the surface temperature to display large latitudinal, diurnal and seasonal variations. The surface temperature at the equator varies from ∼200 K at night to ∼300 K during the day and the temperature at the winter pole is ∼130 K in comparison to ∼190 K at the summer pole (de Pater and Lissauer 2001).

Mars has a tenuous atmosphere composed of: 95.3% CO_2, 2.7% N_2, 1.6% Ar, 0.13% 0_2, 0.07% CO, and $< 0.03\%$ H_2O (de Pater and Lissauer 2001). The atmospheric temperature profile decreases above the surface and exhibits no stratosphere. The temperature can vary widely with the amount of dust in the atmosphere. When a dust storm arises, absorption of solar radiation by dust heats up the atmosphere (Fig. 2.15).

CO is present in Mars' atmosphere and exhibits an absorption line at 345.8 GHz (Fig. 2.16). Pressure broadening has minimal effect because of low atmospheric pres-

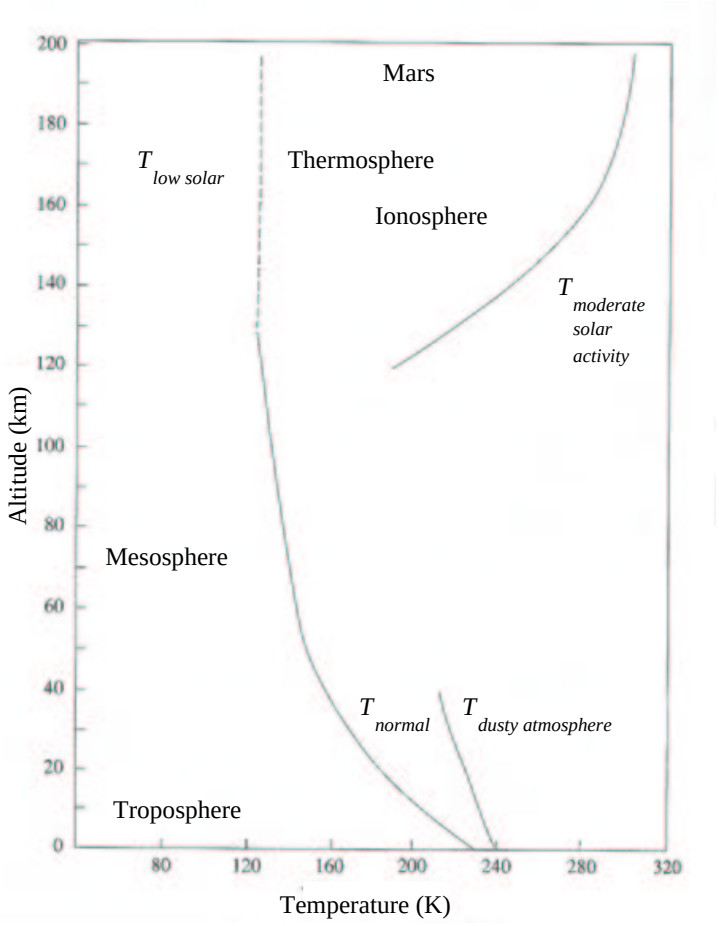

Figure 2.15: *The approximate temperature profile of Mars (de Pater and Lissauer 2001).*

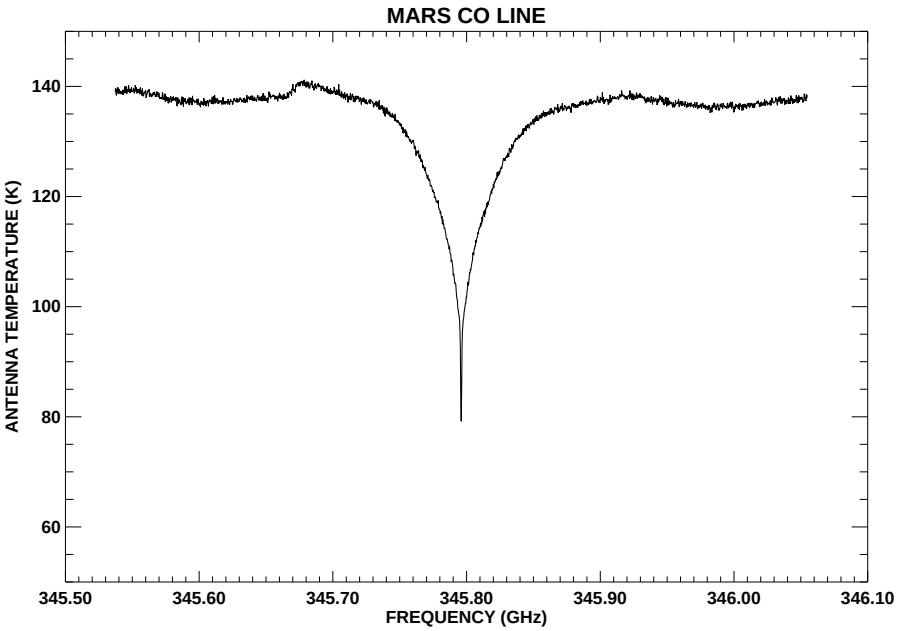

Figure 2.16: *The Mars J=3–2 CO line measured using RxB3. The line has a FWHM of ∼13 MHz. The FTS measurements use a resolution of 1.8 GHz which indicates that this line will not be measurable (Clancy* et al. *2003).*

sure. This results in a narrow absorption line (FWHM $\sim$ 13 MHz) which was not resolved by the FTS. The absorption was also not significant for the SCUBA observations; calculations performed showed that the line does not significantly alter the flux received from Mars ($< 0.1\%$) . RxB3 is capable of high resolution measurements, but calibration against an astronomical target was not required.

Mars was used as a calibrator because, at conjunction, it has an angular size less than $5''$. In addition, millimetre measurements (at 90 GHz) by Ulich (1981) and far-infrared model results (at 857 GHz) by Wright (1976) indicate that Mars is a near-blackbody in the submillimetre region (Griffin *et al.* 1986).

The Mars model was developed for the FLUXES program at the Joint Astronomy Centre (JAC) to predict planetary brightness temperatures based on the date of observation. Brightness temperatures for Mars at 345 GHz are derived by logarithmic interpolation between the 857 GHz results from Wright (1976) and the 90 GHz results from Ulich (1981). Ulich showed that the 90 GHz brightness temperature is given

by,

$$\begin{aligned} T(R) &= T(R_0)\left(\frac{R_0}{R}\right)^{\frac{1}{2}}, \\ T(R_0) &= 206.8 \pm 5.8K, \\ R_0 &= 1.524AU, \end{aligned} \tag{2.63}$$

where $T(R)$ is the brightness temperature at a heliocentric distance R, and $T(R_0)$ is the brightness temperature at a mean heliocentric distance R_0. The 857 GHz brightness temperatures are tabulated in 40 day increments; using the values on either side of the date in question, the brightness temperature is found by linear interpolation.

This model does not take into account the effect of dust storms; measurements during these times were avoided. The quoted uncertainty in this model, without accounting for error due to dust storms, is $\pm 5\%$ (Privett *et al.* 1998).

To calculate the Mars model a date and heliocentric distance must be provided. An example of the Mars model (Fig. 2.17) has been produced for a Universal Time (UT) of April 24, 2003 at 14:15. This corresponded to a heliocentric distance of $R = 1.480$ AU.

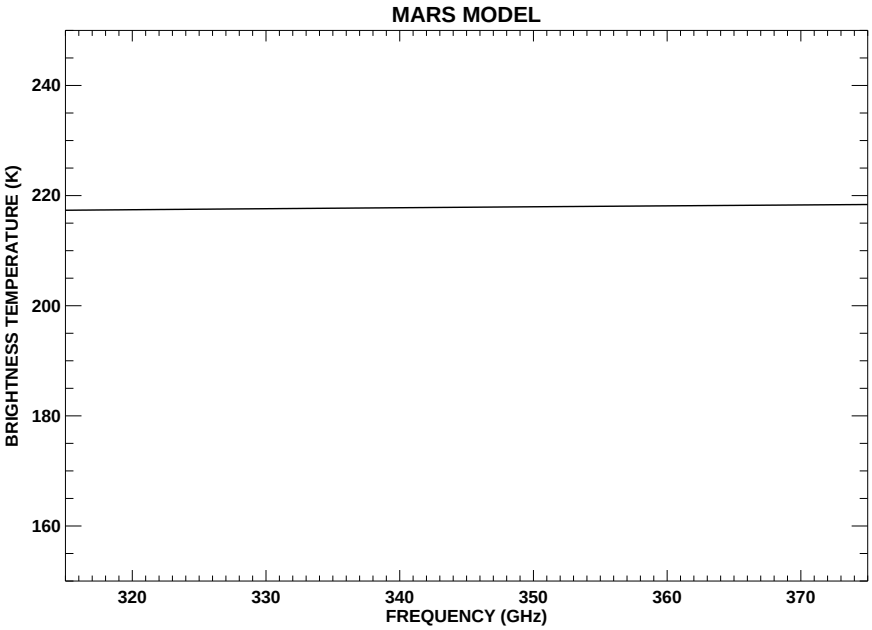

Figure 2.17: *The Mars model at 14:15 hrs on 2004-04-24 (UT).*

Chapter 3

Heterodyne Observations of Neptune

Spectroscopic observations of Neptune's J=3–2 CO line were conducted using the facility heterodyne receiver, B3, at the JCMT. RxB3's high resolution allowed a CO profile through the atmosphere to be determined by measuring the strong emission, originating in the upper stratosphere, and the broad absorption, from the lower stratosphere and troposphere simultaneously. This chapter starts with a general explanation of the operation of RxB3. Observations and data analysis follow. A summary of the results found using this method will end the chapter.

3.1 Heterodyne receivers

Receiver B3 is a facility receiver, by which is meant that it is operated and maintained by the JCMT staff for the benefit of visiting observers. Observers typically need only specify the instrument configuration required for their observations, and are provided with a calibrated data set. A brief overview of the operation of heterodyne receivers, and RxB3 in particular, is nevertheless provided in this section.

Heterodyne receivers measure the signal from an astronomical source by mixing the source radiation with radiation from a local oscillator (LO) by means of a non-linear mixer. Converting the high frequency source radiation to a lower frequency allows the use of low-noise radio-frequency electronics to amplify and process the signal. Fig 3.1 is a basic schematic of the optical layout of the heterodyne receiver, B3.

The first component in the receiver is a reflecting chopper wheel that allows the receiver to alternately view the astronomical and calibration sources. The source

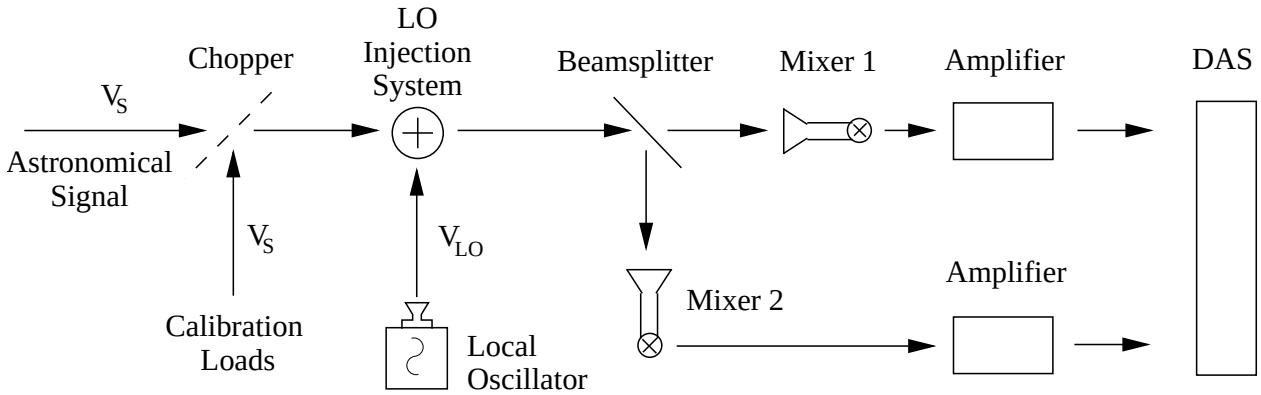

Figure 3.1: *A basic optical schematic of heterodyne receiver, B3.*

radiation then encounters the LO injection system. This is a dielectric (Mylar) sheet that has a high transmittance and low reflectance allowing both the source and LO signals to enter the receiver.

The source and LO signals travel from the LO injection system to a wire grid polarizing beamsplitter which transmits one polarization to the first mixer and reflects the other polarization to the second mixer. The radiation propagates in free space before reaching the mixers, which absorb energy from the incoming electromagnetic wave. The mixers are located inside waveguides to provide optimal signal conversion efficiency. Horns at the entrances to the waveguides serve to focus the free-space wave into the cavity.

Heterodyne receivers require a non-linear mixer, the simplest of which can be a diode. RxB3 uses the superconductor-insulator-superconductor (SIS) junction for its mixers. They are constructed using a thin insulating (oxide) layer sandwiched between two superconducting (niobium) layers. This type of mixer offers significant advantages in nonlinearity and sensitivity (Matthews *et al.* 2004). Fig. 3.2 shows the current-voltage (IV) response curve of a SIS junction. The "LO off" curve shows that the current flowing across the junction is virtually negligible until a large bias voltage is reached (V_g). This is the voltage required to break Cooper pairs of electrons and is given by,

$$V_g = \frac{2\Delta}{e}, \tag{3.1}$$

where 2Δ is the energy gap of the superconductor (Lazareff 2005). In the presence of electromagnetic radiation, "LO on" curve, photons are absorbed and their energy $h\nu$ allows the onset of conduction at a lower bias voltage, referred to as photon-assisted tunnelling. The result is the conversion of an incoming stream of photons to an electrical current across the junction (Phillips 1988).

Despite the complex form of the SIS mixer response, its basic operation can be demonstrated by considering instead the simplest possible example of a nonlinear mixer, a quadratic response,

$$I = \alpha V^2, \tag{3.2}$$

where α is a proportionality constant. The incoming signal from the LO V_{LO} and a

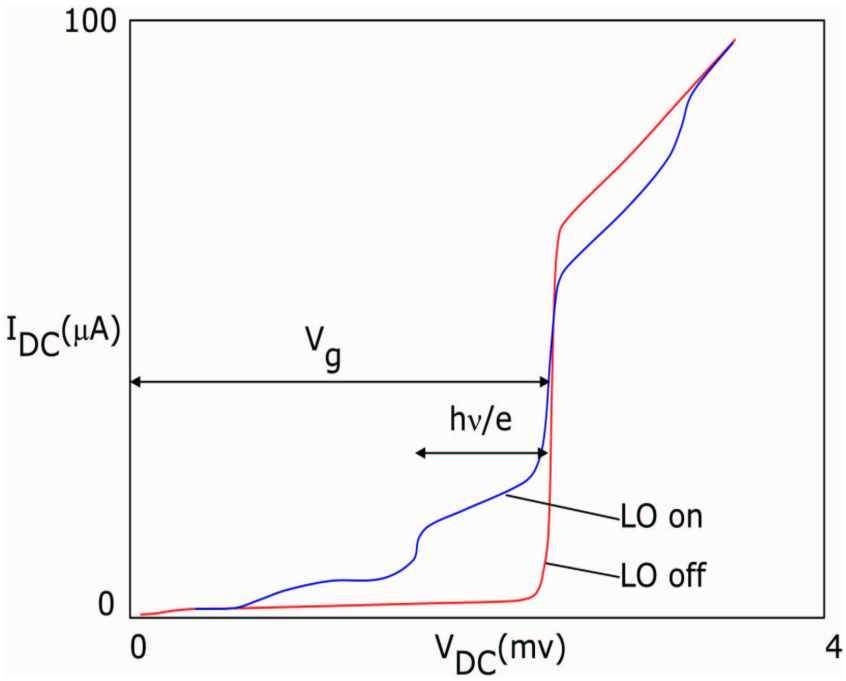

Figure 3.2: *A plot of the IV response curve for a SIS junction (Lazareff 2005).*

monochromatic source V_S can be represented as,

$$V_{LO} = V_{lo}\, cos\, \omega_{lo} t, \tag{3.3}$$

$$V_S = V_s\, cos\, \omega_s t, \tag{3.4}$$

where V_{lo} is the LO voltage, ω_{lo} is the angular frequency of the LO, V_s is the source signal voltage, and ω_s is the angular frequency of the source. The resulting current after the source and LO signals (Eqs. 3.3 and 3.4) are mixed is given by,

$$I = \alpha \left(V_s^2\, cos^2\, \omega_s t + V_{lo}^2\, cos^2\, \omega_{lo} t + 2 V_s V_{lo}\, cos\, \omega_s t\, cos\, \omega_{lo} t \right), \tag{3.5}$$

and expanding the last term gives,

$$2 V_s V_{lo}\, cos\, \omega_s t\, cos\, \omega_{lo} t = V_s V_{lo} \left[cos(\omega_s - \omega_{lo}) t + cos(\omega_s + \omega_{lo}) t \right]. \tag{3.6}$$

Eq. 3.6 shows that a component of the current will leave the mixer at a difference frequency of $\omega_s - \omega_{lo}$, referred to as the intermediate frequency (IF) (White 1988).

The source signal frequency and voltage can be recovered after the signal has been processed by holding the local oscillator frequency and voltage constant.

When the source is composed of many frequency components Eq. 3.4 is altered to give,

$$V_S = V_{s1}\, cos\, \omega_{s1} t + V_{s2}\, cos\, \omega_{s2} t + ... \tag{3.7}$$

Eq. 3.6 will then include terms of the form $V_{s1} V_{s2}\, cos(\omega_{s1} - \omega_{s2})t$. These cross-term signals will lie in the same band as the IF signal and will confuse the recovery of the source signal frequency and voltage. V_{lo} is set significantly higher than the source voltage to suppress the cross-term signals.

Radiation from an astronomical source can be represented as a series of frequency components higher and lower than the LO frequency. Source frequencies lower than the LO frequency lie in the lower sideband (LSB); similarly, source frequencies higher than the LO frequency lie in the upper sideband (USB) (Fig. 3.3). This presents some complications in extracting the original source signal as both the upper and lower sideband frequencies are mixed with the LO frequency. For example, input signals at $\nu = 100.1$ GHz and $\nu = 99.9$ GHz mixed with a 100 GHz LO frequency will each produce an IF at 100 MHz. The LSB components produce an IF spectrum which is a mirror image of the input signal. This can produce an IF output where it is not possible to determine which band the signal is originally from, or, if it is a combination of both. A single sideband filter can be employed to avoid this. In RxB3 this filter is incorporated into the LO injection system. This mode, referred to as single sideband (SSB), was chosen for these observations.

The signal is processed using the Digital Autocorrelation Spectrometer (DAS) (Fig. 3.4), which ultimately sets the spectral resolution and bandwidth of the observations. Each mixer signal is connected to 8 down-converter modules (DCM), which split the signal into 8 subbands each 160 MHz wide. Typically only 125 MHz of each is used which produces an output from the subbands that overlaps in frequency space. The DCM's are electronically connected to the 2048 DAS channels under software control in a configuration which is selectable by the observer. The set of DAS channels connected to each subband measures the autocorrelation of the signal,

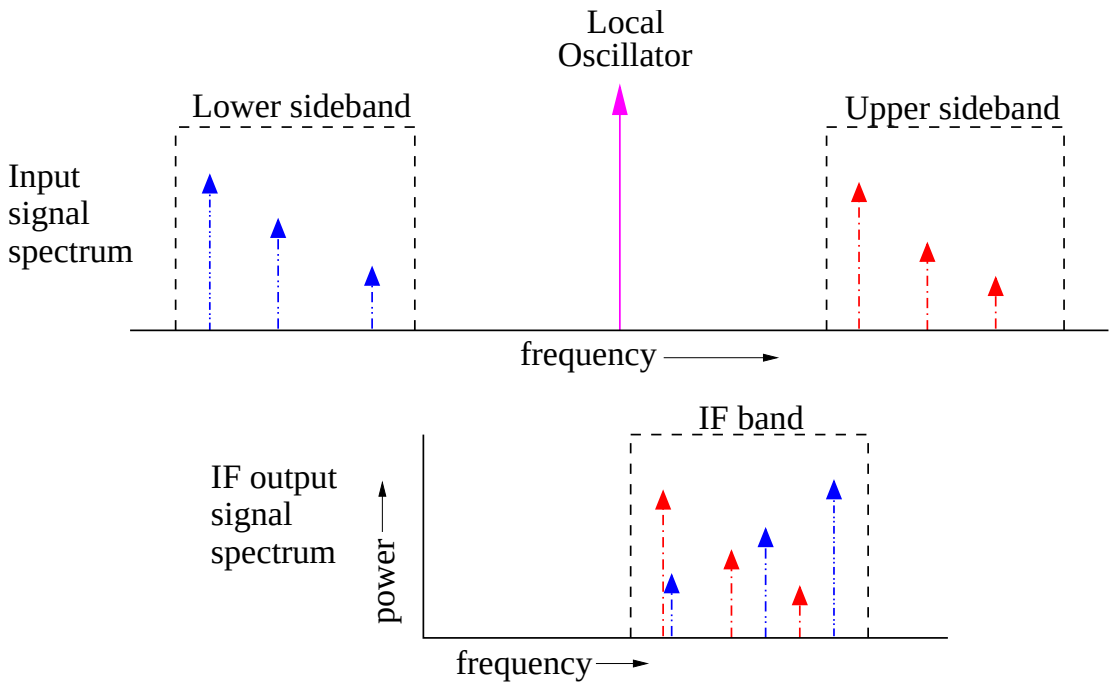

Figure 3.3: *A diagram of the resulting IF spectrum when the upper and lower SB source frequencies are measured(Lesurf 2005).*

the Fourier transform of which is the spectrum.

Each channel in the DAS is set to sample the autocorrelation at fixed, regular time intervals. When all 2048 channels are connected to one subband the autocorrelation is sampled over a long time period producing a resolution of 78 kHz for a bandwidth of 125 MHz. This is the highest spectral resolution and only one polarization can be measured in this mode. At the opposite extreme, 128 DAS channels are connected to each of the 16 DAS subbands. This results in a shorter sampling time, giving a resolution of 1.25 MHz and a total bandwidth of 920 MHz in each polarization. When both polarizations are utilized, two spectra are produced for each integration maximizing the observing efficiency (Matthews *et al.* 2004). The output to the telescope user is a spectrum that is contiguous in channel space but overlaps in frequency space. Analysis software allows the user to merge the spectra between subbands and average the polarizations if two mixers are used.

The observations conducted for this project required a large bandwidth to be

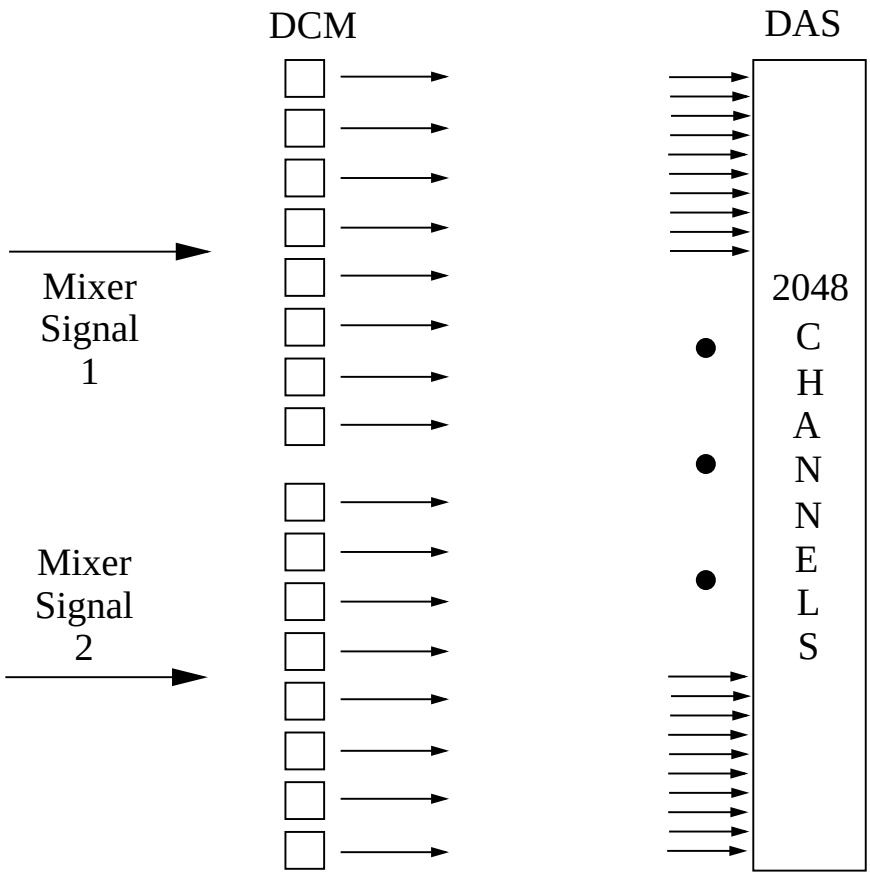

Figure 3.4: *A schematic of the DAS.*

covered (∼20 GHz). The DAS was configured for its maximum bandwidth (920 MHz) and lowest resolution (1.25 MHz) using dual mixers to ensure that a minimal amount of tunings were required.

3.2 Observations

Observations of the CO J=3–2 transition in Neptune were carried out on a series of dates in 2003 and 2004 (Table 3.1). The stratospheric emission core was easily measured at the selected spectral resolution. The tropospheric absorption feature, however, is strongly pressure-broadened and covers a large frequency range (∼ 20 GHz). This makes it significantly more difficult to measure with traditional heterodyne techniques. The line was therefore measured in 25 discrete segments with tunings spaced by 850 MHz, a resolution of 1.25 MHz, and a frequency overlap at each tuning of approximately 8%. The overlap between tunings was necessary to provide an indication of baseline continuity.

The receiver was operated in SSB mode with dual SIS mixers simultaneously detecting orthogonally-polarized radiation. This produced two spectra for each integration which were averaged during the processing stage. The target was observed using a standard beam-switching procedure with a beam throw of 60″ in azimuth. Calibration was performed using the standard hot/cold load method (Ulich and Haas 1976, Kutner and Ulich 1981). Frequent (approximately every 30 minutes) pointing checks were performed to maintain the pointing accuracy necessary for these measurements (within 1–2″). At each tuning frequency, 5-minute integrations were performed; many tunings were repeated more than once. Total integration times for each tuning therefore varied from 5 to 20 minutes.

The measured CO feature is shown in Fig. 3.5, with the tuning bands indicated by different colours. Baseline continuity was crucial in order to avoid post-processing baseline adjustments which would severely limit the accuracy of the data set. Fortunately, the instrument calibration stability was such that the data quality was excellent and no such adjustments were required.

Table 3.1: *Summary of B3 observations.*

Tuning Frequency (GHz)	**Date of Observations** (UT) YYYY/MM/DY	**Int. Time** (min)	**Tuning Frequency** (GHz)	**Date of Observations** (UT) YYYY/MM/DY	**Int. Time** (min)
335.60	2004/06/07	5	346.65	2003/10/15	5
				2004/05/26	5
336.45	2004/06/07	5	347.50	2003/10/15	5
				2004/05/26	5
337.30	2004/06/07	5	348.35	2003/10/15	5
				2004/05/26	5
338.15	2004/06/07	5	349.20	2003/10/15	5
				2004/05/26	5
339.00	2004/05/24	10	350.05	2003/10/15	5
	2004/06/07	5		2004/05/26	5
339.85	2004/05/24	10	350.90	2003/10/15	5
	2004/06/07	5		2004/05/26	5
340.70	2004/05/24	10	351.75	2003/10/15	5
	2004/06/07	5		2004/05/26	5
341.55	2004/06/07	5	352.60	2003/10/16	5
				2004/05/26	5
342.40	2003/10/16	5	353.45	2003/10/16	5
	2004/05/26	5		2004/05/26	5
	2004/06/07	5			

Table 3.1: *continued...*

Tuning Frequency (GHz)	**Date of Observations** (UT) YYYY/MM/DY	**Int. Time** (min)	**Tuning Frequency** (GHz)	**Date of Observations** (UT) YYYY/MM/DY	**Int. Time** (min)
343.25	2003/10/16	5	354.30	2003/10/16	5
	2004/05/26	5		2004/05/26	5
	2004/06/07	5			
344.10	2003/10/16	5	355.15	2003/10/16	5
	2004/05/26	5		2004/05/26	5
	2004/06/07	5			
344.95	2003/10/16	5	356.00	2003/10/16	5
	2004/05/26	5		2004/05/26	5
	2004/06/07	5			
345.80	2003/10/15	5			
	2003/10/16	5			
	2004/05/26	5			
	2004/06/07	5			

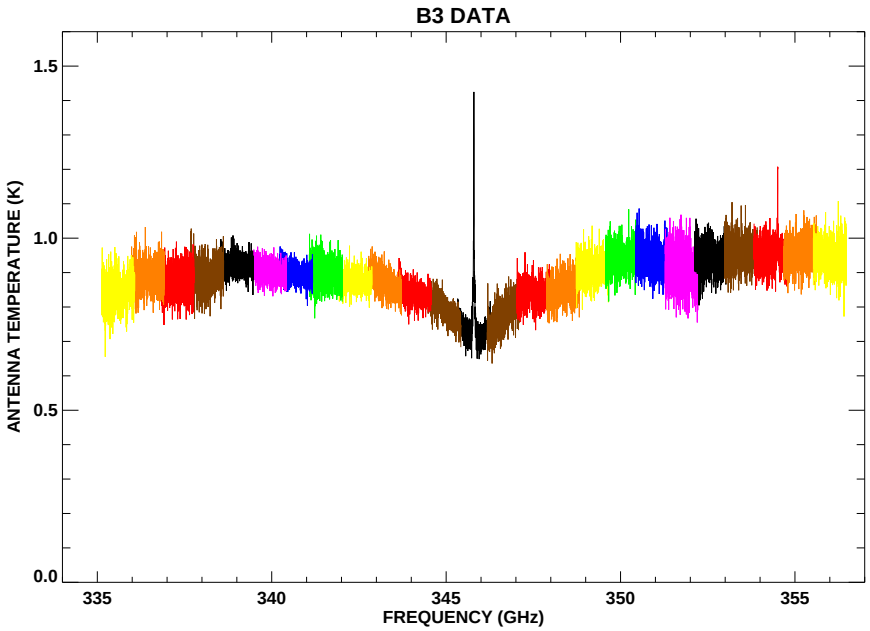

Figure 3.5: *The antenna temperature spectra of Neptune, measured using receiver B3 at the JCMT. Resolution, 1.25 MHz; band overlap, 70 MHz; bandwidth, 920 MHz. Each of the 25 tunings are indicated by a different colour.*

3.3 Data analysis

The observations resulted in spectra calibrated in antenna temperature, $T_A^\star$, and corrected for the Earth's atmospheric extinction and various telescope losses (spillover of the beam around the primary and secondary mirrors, imperfect reflectivity, scattering from the secondary mirror support structure). The model produces intensities which can be expressed as brightness temperature T_B through the Planck function. In order to compare the two, the measured spectrum was translated from antenna temperature to brightness temperature as follows,

$$T_B = T_A^\star \frac{1}{B_{eff}} \left[\frac{1}{(1 - 2^{-(\theta_s/B_w)^2})} \right], \tag{3.8}$$

which describes the coupling of the telescope beam to the source (Marten *et al.* 1993). The term in square brackets describes the coupling of an ideal Gaussian beam of width B_w (full width at half maximum) to a source of angular diameter θ_s; the beam efficiency B_{eff} is a known property of the telescope and characterizes the departure of the beam from the ideal Gaussian shape. The large frequency coverage of these observations required that B_w be parameterized as a function of frequency. A straight line was fit to the measured beam width at a variety of frequencies across this range,

$$B_w = -0.0396\nu + 27.524, \tag{3.9}$$

where ν is the observation frequency in GHz. The main beam efficiency (B_{eff}) at 345 GHz is 0.62±0.03 (Avery 1998).

Previous measurements were consistent with uniform CO profiles with abundances of approximately 1.2x10^{-6} (Marten *et al.* 1993). A model spectrum, calculated for a uniform profile with this abundance value, is compared with the measured spectrum in Fig. 3.6. The agreement between the shapes of the two spectra is visibly poor in the wings of the line, indicating that a uniform-abundance profile is inappropriate.

The inadequacy of the uniform CO profile fit required that the contribution functions (Fig. 2.12) be examined to determine which atmospheric pressure levels

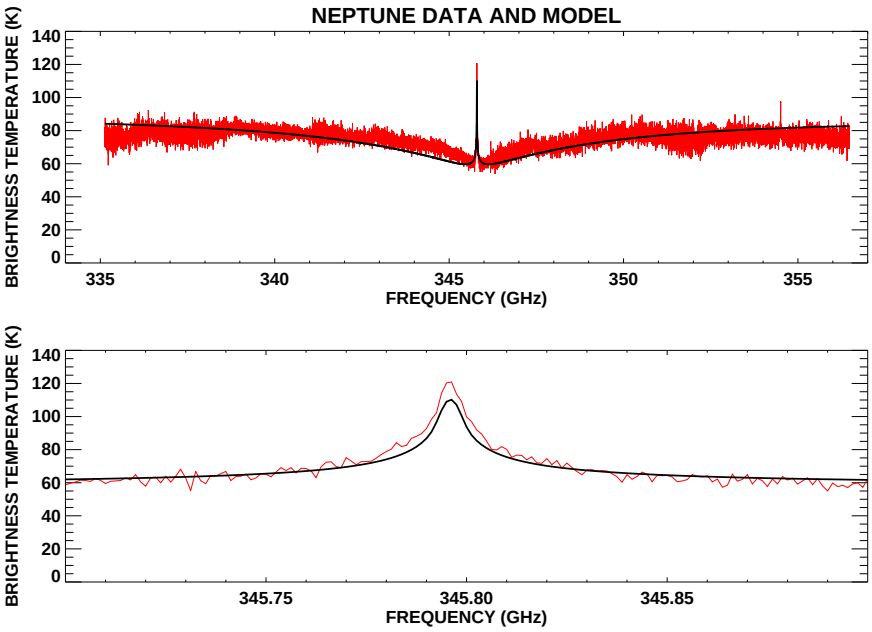

Figure 3.6: *The measured Neptune spectrum (red) overlaid with a model corresponding to a constant CO abundance of* $1.2\text{x}10^{-6}$ *(black).*

contribute most significantly to the absorption and emission components of the line. As the frequency displacement from line centre increases the contribution peaks at higher pressures. Examination of the width and overlap of the contribution functions constrained the number of parameters that could be fit using the measured spectrum. The red and violet curves of Fig. 2.12 show the least amount of overlap thereby allowing the upper stratosphere and troposphere CO values to be fit independently of each other. The contribution functions, calculated at frequencies that lie between 345.8 GHz (red curve) and 336.1 GHz (violet curve), show significant overlap allowing only an additional two parameters to be fit independently. These two parameters were chosen to be the top and bottom pressure levels of the transition region between the stratospheric and tropospheric CO.

A variable CO profile with constant values in the troposphere and in the upper stratosphere, and a transition region between them in which the CO abundance varied logarithmically with pressure was therefore adopted for the present analysis. The best-fit values of the four parameters (two abundances and the top and bottom

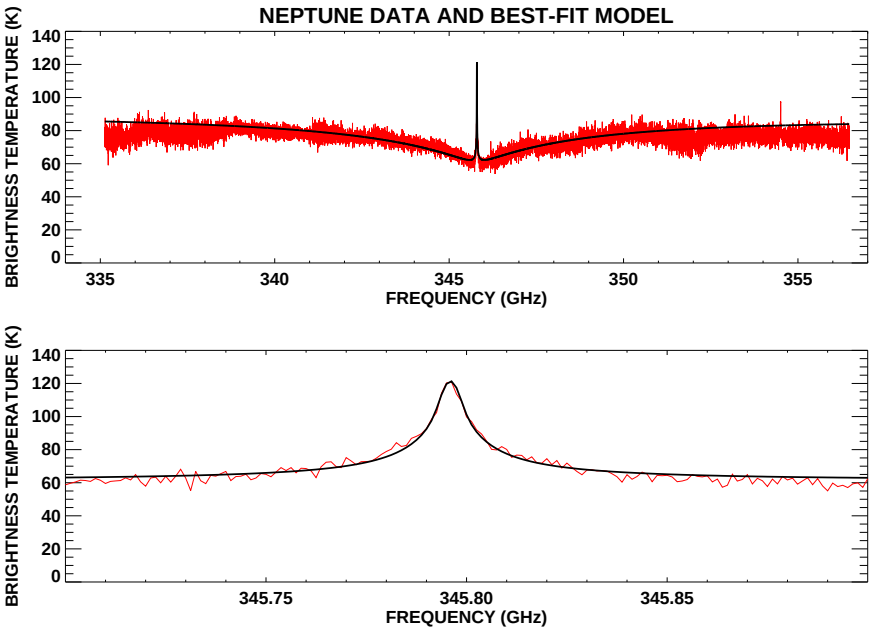

Figure 3.7: *The measured Neptune spectrum (red) overlaid with the best-fit model (black). This model was produced using the CO profile shown in Fig. 3.8.*

pressures of the transition region) were determined by the least-squares method in two stages in which the emission and the absorption components of the line were considered independently. The measured and modelled spectra are compared in Fig. 3.7. The drop off in the far-wings of the measured spectrum (red curve; Fig. 3.7) is likely due to calibration uncertainty and is taken into account when determining the uncertainty, due to the beam efficiency parameter (B_{eff}), in the CO profile. The best-fit CO profile corresponding to the model in Fig. 3.7 is shown in Fig. 3.8. The best-fit abundances were found to be $0.8\text{x}10^{-6}$ in the troposphere and lower stratosphere, increasing with altitude to $1.9\text{x}10^{-6}$ in the upper stratosphere.

To determine the error on the derived CO profile, the errors associated with each model input parameter were considered. This involved the following model components:

1. The HITRAN CO line parameters (Table 2.1),

2. The mole ratios of H_2, He, and CH_4 (§2.3.3), and

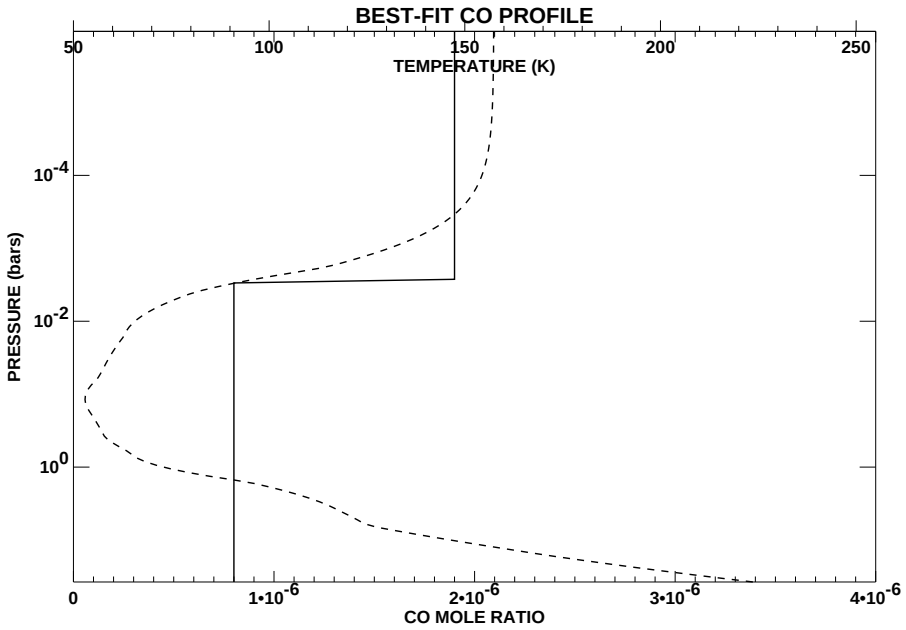

Figure 3.8: *The model temperature profile (dashed) and the CO profile (solid) required to produce the best-fit model of Fig. 3.7.*

3. The temperature profile (§2.3.1).

This analysis produced a best-fit CO profile to the data, using the same method as for the nominal model, for each of the upper and lower ranges of the parameters listed above. The errors in both the HITRAN line parameters and the mole ratios (H_2, He, CH_4) produced negligible differences from the nominal result. The temperature profile, however, has many regions in which the temperature is not well constrained (Fig.1.4). Applying these temperature ranges to the analysis resulted in significant changes to the derived CO abundance profile.

To determine the effect that variations in the temperature profile had on the derived CO abundance the errors on the temperature in each region of the atmosphere were considered. The temperatures, at pressures above 2 mbar, are well constrained by disk-averaged mid- and far-infrared spectra for which disk-averaged temperature profiles can be fit with an uncertainty of approximately ± 2 K (G.S. Orton, personal communication). At pressures lower than 2 mbar, however, the temperatures are not well constrained, with a value of 168 ± 20 K (Bishop *et al.* 1998, Roques *et al.*

1994). The nominal profile uses a value of 158 K, as used in Marten *et al.* (1993), and within the error of the value quoted above. The error in the derived CO profile has been estimated using four different temperature profiles: the first two profiles were chosen to deviate from the nominal profile by ±2 K, while the third and fourth profiles use the extreme values of 148 K and 188 K above 2 mbar.

The best-fit CO profiles corresponding to the nominal and ±2K temperature profiles are shown in Fig. 3.9. It can been seen that the lower atmosphere CO abundance changes along with the pressure levels of the transition region, but the upper atmosphere CO abundance is unaffected. The calculated spectra corresponding to these temperature profiles are shown in Fig. 3.10. The colder temperature profile produces a better fit to the data than the nominal and warmer temperature profiles. This may indicate that temperatures in the troposphere are better represented by a smaller increase over the Voyager radio occultation profile (4 - 8 K rather than 6 - 10 K). The best-fit CO profiles corresponding to the nominal, 148 K, and 188 K temperature profiles are shown in Fig. 3.11. While the upper atmosphere CO abundance is strongly dependent on the assumed temperature, the transition region moves by less than 1 mbar from the nominal result and the lower atmosphere CO abundance is completely unaffected.

The conversion of the data from antenna temperature to brightness temperature was also a source of error in the derived CO profile. To account for the uncertainty in the beam efficiency, a best-fit CO profile was determined for each spectrum resulting from low and high beam efficiencies of 0.59 and 0.65 respectively. The best-fit CO profiles resulting from the beam efficiency error calculation are shown in Fig. 3.12. A beam efficiency of 0.59 produces a better fit to the data than 0.62 and 0.65. Beam efficiency calculations, using Uranus as the reference source, gave no indication that a lower beam efficiency should be used in this present analysis.

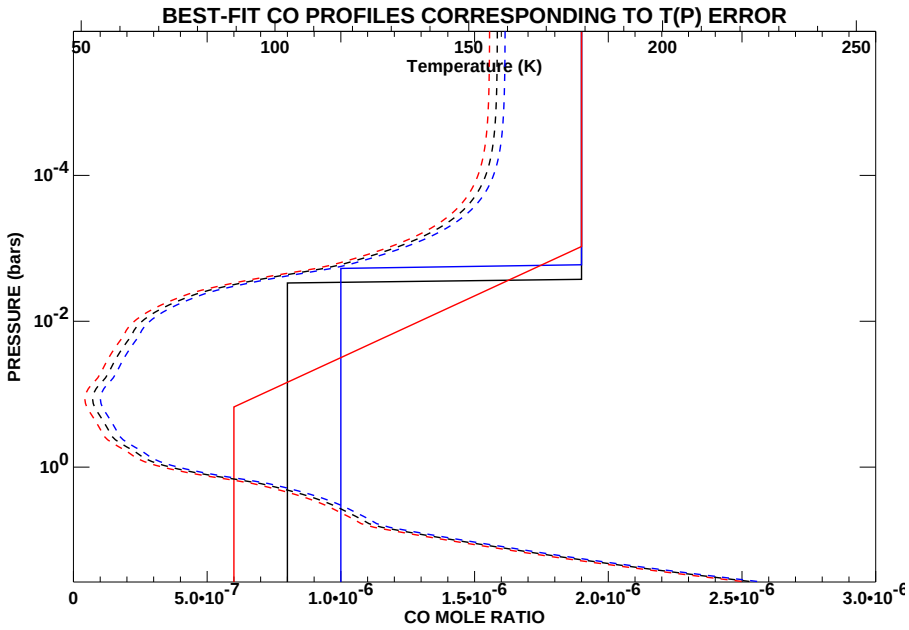

Figure 3.9: *The errors on the atmospheric profile (dashed curves) and their effect on the best-fit CO profile (solid curves). Nominal (black), −2K (red), +2K (blue).*

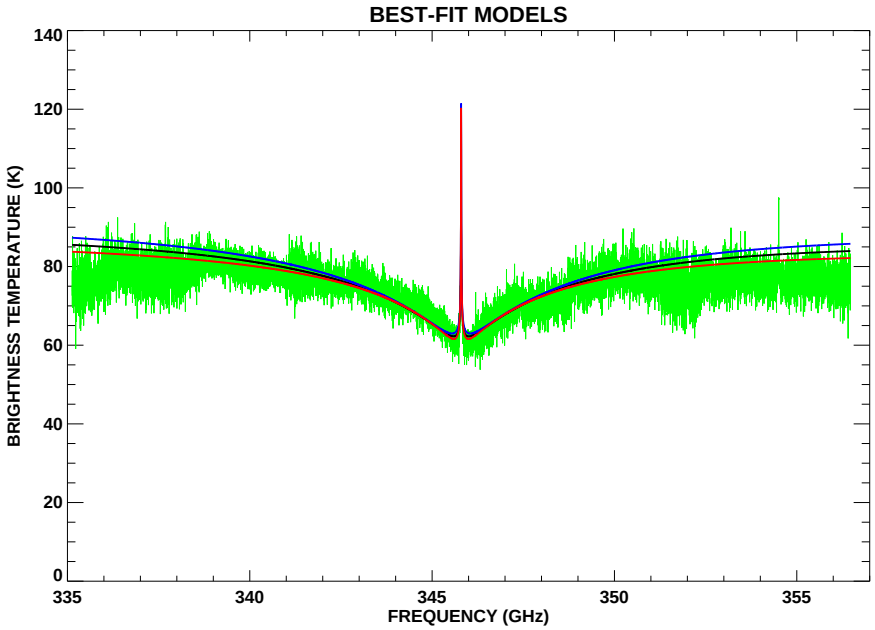

Figure 3.10: *The measured spectrum (green) overlaid with the model fits for the atmospheric profiles of Fig. 3.9.*

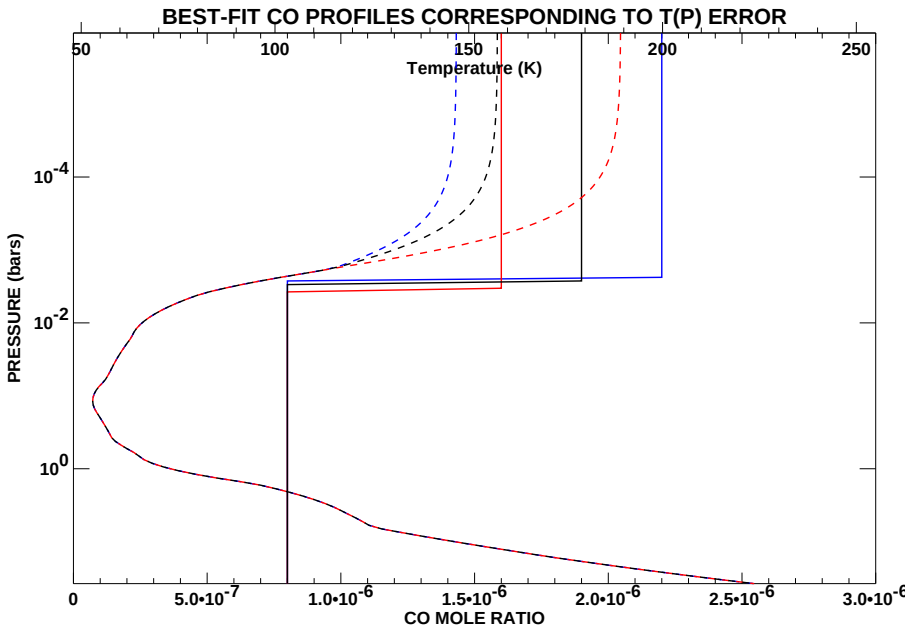

Figure 3.11: *The errors on the atmospheric profile (dashed curves) and their effect on the best-fit CO profile (solid curves). Nominal (black), upper atmosphere T=148 K (blue), upper atmosphere T=188 K (red).*

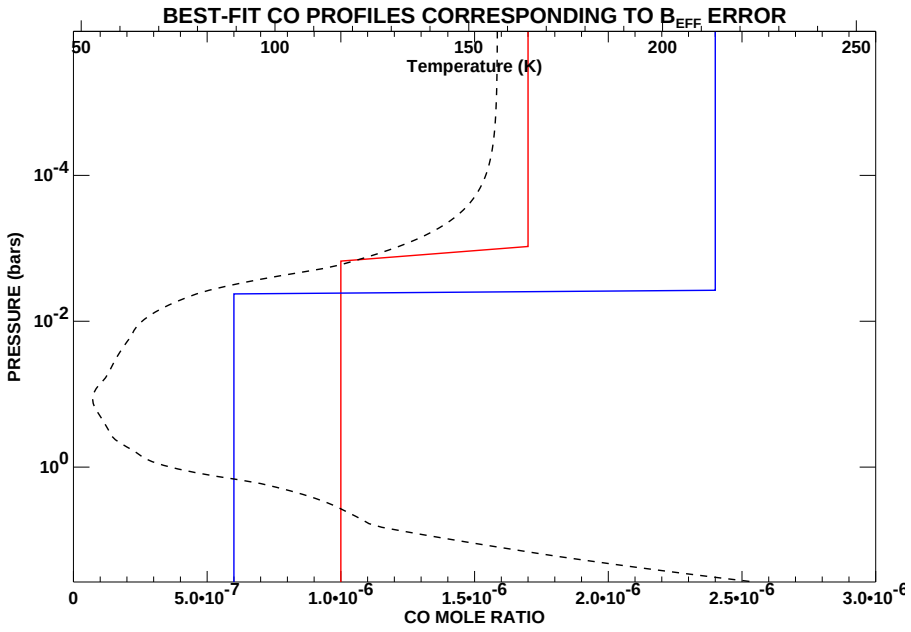

Figure 3.12: *The best-fit CO profiles that result from brightness temperature calibration using beam efficiencies of 0.59 (blue) and 0.65 (red).*

3.4 Summary

On the basis of the calculations performed in §3.3 the CO abundances are estimated to be $0.8 \pm 0.2\text{x}10^{-6}$ and $1.9^{+0.5}_{-0.3}\text{x}10^{-6}$ in the lower and upper regions respectively.

Chapter 4

Fourier Transform Spectroscopy Observations of Neptune

A Fourier Transform Spectrometer (FTS), of which the Michelson interferometer is a simple example, measures the two-beam interference pattern of the radiation from a source as the path difference is continuously varied, the Fourier transform of which is the spectrum. One of the main advantages of a FTS is that all of the radiation over an entire spectral region is used at all times in constructing the spectrum of the source; this is called the multiplex advantage. The spectral resolution of a FTS is however significantly lower than for a heterodyne receiver. Fig. 4.1 shows the tropospheric CO absorption line in Neptune convolved to a spectral resolution of 1.8 GHz, which is the resolution used for the measurements presented in this chapter. The broad spectral range of this absorption line makes it ideally suited to observation using a FTS. The intermediate spectral resolution of this type of spectrometer, however, does not allow a measurement of the stratospheric emission. Observations using a FTS and can therefore only be used to determine the lower atmosphere CO abundance in Neptune.

The J=3–2 CO line in Neptune was measured in 1993 using a polarizing FTS by Naylor *et al.* (1994) (Fig. 1.8). The large sinusoidal modulation in the data (solid curve, Fig. 1.8) was the result of multiple reflections from parallel surfaces within the detector optics; this limited the precision in the derived CO abundance. It was therefore decided that a repeat of this measurement, with improved instrumentation, was required to improve upon the 1993 results. The following were implemented for this purpose:

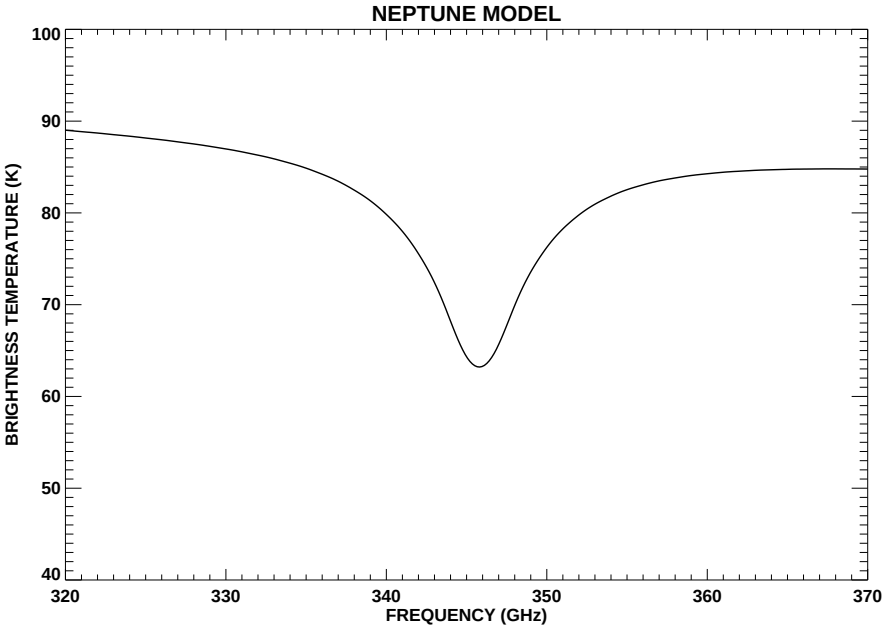

Figure 4.1: *The Neptune CO line model, for a uniform abundance of* $1\text{x}10^{-6}$*, convolved to the FTS resolution (1.8 GHz).*

1. A new detector with optics designed to minimize the effects of multiple reflections,

2. A new FTS, in the Mach-Zehnder (MZ) design and,

3. A data reduction pipeline, which allowed for correction due to the Earth's atmospheric transmission.

A successful observing run, using this new equipment, was undertaken in September 2002. The 1993 data analysis was also revisited because of the development of the data reduction pipeline.

This chapter is divided into two parts: the 2002 MZ FTS observations and the re-analysis of the 1993 data. The 2002 observations include a discussion of the operation and calibration of the MZ FTS, the observations, data analysis, and results. The 1993 re-analysis includes a brief summary of the operation of the polarizing FTS and the observations. A discussion of the re-analysis using Mars as the calibration source follows. The chapter ends with a summary of the results from the two data

sets.

4.1 2002 FTS observations

The FTS used for these observations was a visiting instrument at the JCMT. The entirety of the setup, maintenance, data collection and analysis rests on the visiting instrument team. This requires the observer to have extensive knowledge of the operation of the instrument to ensure that the observations and analysis are performed correctly. The JAC staff interacts with the visiting instrument team to provide telescope support during the observing run.

4.1.1 The Mach-Zehnder FTS

The Mach-Zehnder (MZ) FTS was designed and built at the University of Lethbridge by the Astronomical Instrumentation Group (Naylor *et al.* 2003). The FTS uses a Mach-Zehnder design employing two identical intensity beamsplitters allowing access to all four interferometer ports (two input and output ports). This design creates a differential instrument; one input port directed on the astronomical source and the other on a background sky position allowing instantaneous removal of the Earth's atmospheric emission. The signal from the astronomical source is reflected through the telescope optics to the tertiary mirror (Fig. 1.10). This mirror directs the radiation through the elevation bearing to the right Nasmyth platform where the FTS is located during an observing run (Fig. 4.2). An optical schematic of the FTS is shown in Fig. 4.3.

During the commissioning run of the MZ FTS (June 2001), it was discovered that the elevation bearing was, unfortunately, too small to allow dual beams to pass. This required a change in the observing strategy; only one port could be directed on the sky (input port 2, Fig. 4.3). A constant temperature calibration source (liquid nitrogen) was placed in input port 1. The Earth's atmospheric emission was therefore not instantaneously removed during the source observations.

The converging beam from the telescope enters through input port 2 and is

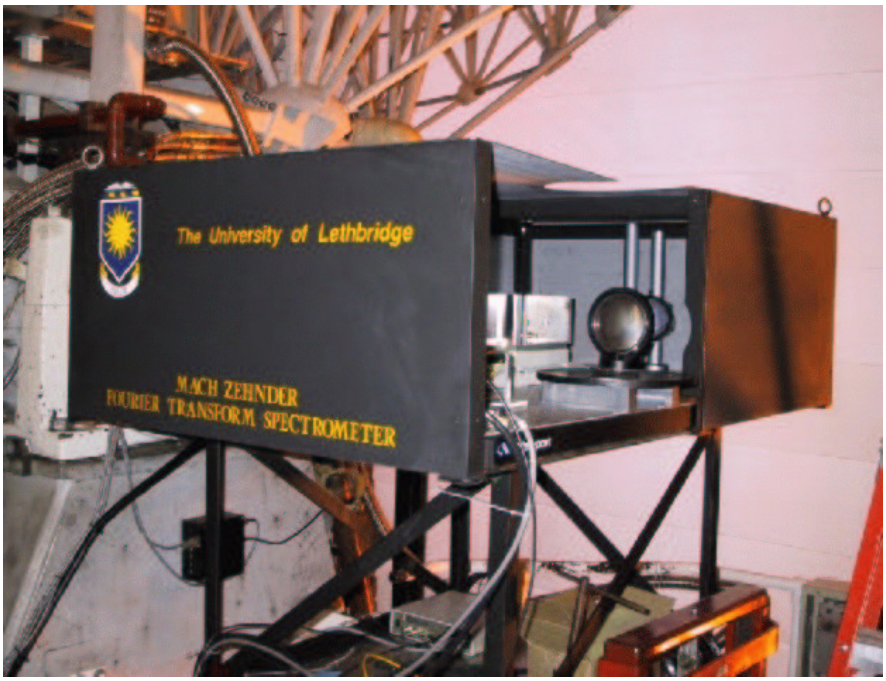

Figure 4.2: *The Mach-Zehnder FTS on the right Nasmyth platform at the JCMT.*

brought to a focus at the first beamsplitter (BS1) by two flat mirrors (M1 and M2). The beamsplitters (BS1 and BS2) are broadband intensity beamsplitters which exhibit equal transmission and reflection in addition to high and uniform beamsplitter efficiency over a broad spectral range (Ade *et al.* 1999). These properties give significant advantages over polarizing and dielectric beamsplitters. For example, both polarizations of the source radiation are processed in the MZ interferometer making it twice as efficient as a polarizing interferometer. Low beamsplitter efficiency and limited spectral range, known to plague dielectric beamsplitters, are not apparent.

After the radiation encounters the first beamsplitter, where half of the radiation is transmitted and the other half reflected, it then travels to the powered mirrors (M3), which collimate the beam. The four mirrors on the moving stage (RT) generate the path difference between the beams in the instrument. The translation stage travels a maximum of 30 cm which provides a maximum optical path difference between the interfering beams of 120 cm. The resolution of a spectrometer $\Delta\tilde{\nu}$ varies inversely

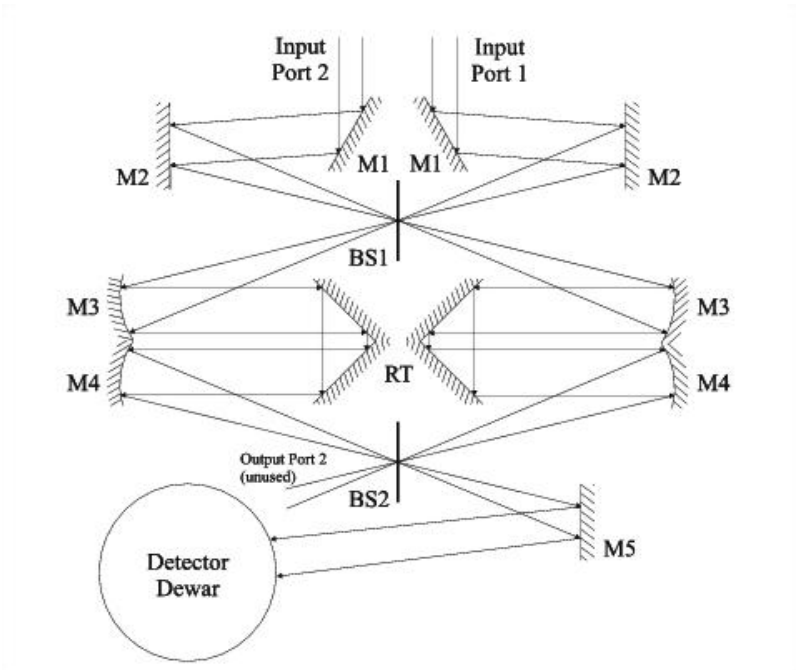

Figure 4.3: *The optical schematic of the Mach-Zehnder FTS (Naylor* et al. *2003). There are two errors in this diagram: the incoming beam from telescope is converging, and the second focus is at field lens in the detector, not BS2.*

with the maximum optical path difference L and is given by,

$$\Delta\widetilde{\nu} = \frac{1.21}{2L}, \tag{4.1}$$

(Bell 1972). The maximum resolution achievable by this FTS is therefore $\Delta\nu$ = 150 MHz.

The FTS was designed to allow spectra to be obtained as the travelling stage scanned in one direction and as the stage scanned in the reverse direction; these scans were labelled UP and DOWN and were treated separately during the analysis process. It was advantageous to be able obtain data in both scan directions because it increased the efficiency of the FTS.

After passing through the moving stage the beam reflects from the second set of powered mirrors (M4) that focus the radiation onto the second beamsplitter (BS2). The MZ FTS has two output ports; however, only one of the output ports was used for these measurements since only one detector was available.

Naylor *et al.* (1999) provide a thorough description of the design and operation of the detector used with the FTS; a brief summary is provided here. Radiation enters the detector dewar through a polypropylene window where it encounters an edge filter which efficiently blocks short wavelength radiation (Fig. 4.4). The next optical element is an adjustable iris which allows the optical beam to be matched to the diffraction-limited telescope beam. This element is manually adjustable and has set values for each of the filter passbands. The beam is then directed to one of the 6 filters in the filter wheel. These filters have passbands that are matched to the atmospheric windows accessible from the telescope (Fig. 1.11). Subsequently, the radiation is passed into the detector unit which concentrates the radiation onto the bolometer element. These observations required the use of the 850μm filter and an aperture of 50 mm to match the diffraction limit of the telescope beam.

Fig. 4.4 shows two detectors, but only one is used. The detector contains a single element bolometer that consists of a small semiconductor element mounted on a dielectric substrate. The dielectric serves as the absorber of the incident radiation while the semiconductor element serves as the thermometer that measures the

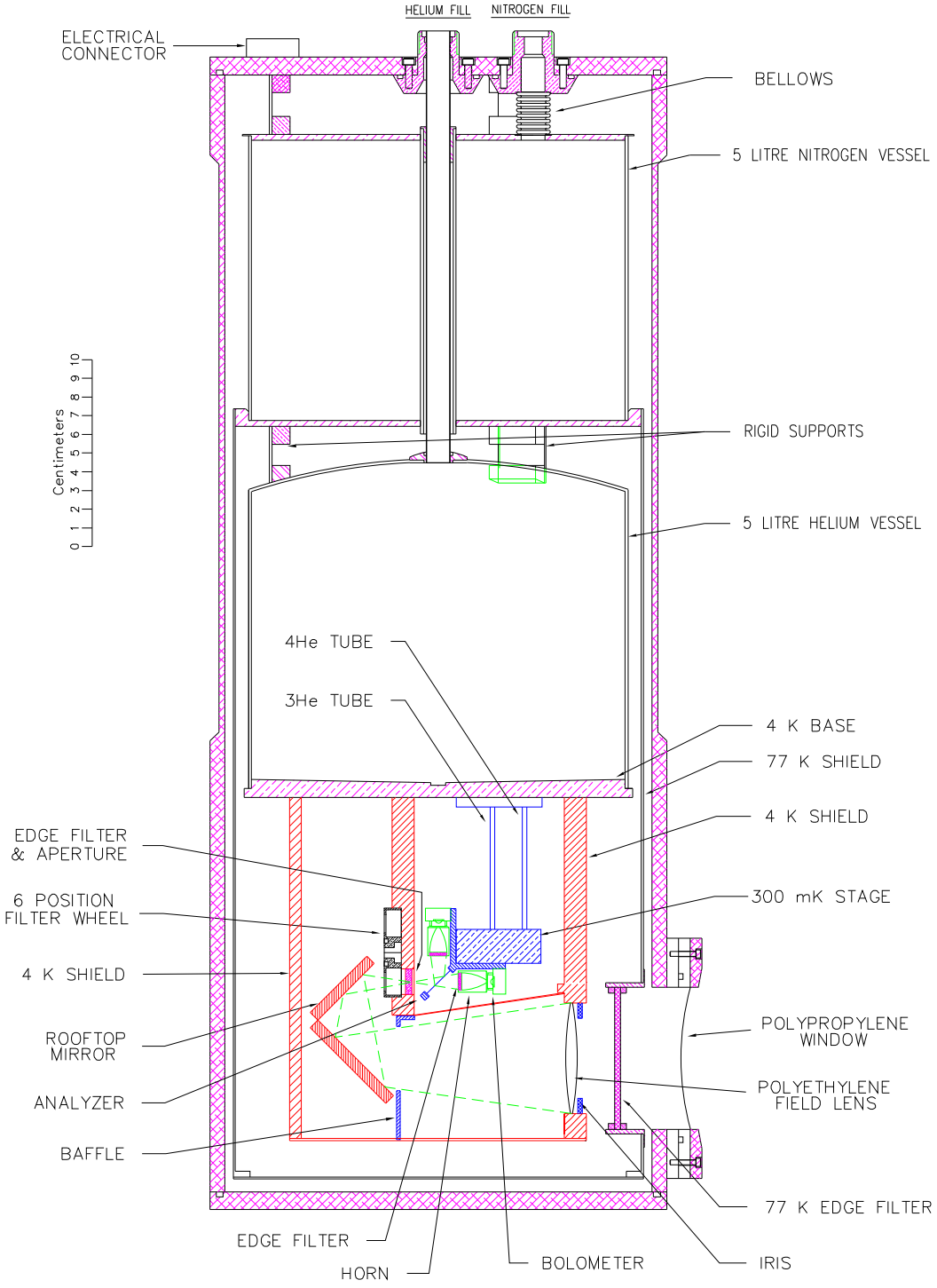

Figure 4.4: *The optical schematic of the FTS detector system (Naylor* et al. *1999).*

temperature fluctuations of the substrate. In order to suppress thermal noise which would otherwise mask these temperature fluctuations, the bolometer is cooled to 0.3 K using ^{3}He/^{4}He.

4.1.2 Calibration of FTS data

The output from the detector contains a record of the radiation intensity versus path difference, referred to as an interferogram. The signal at the detector output contains many components in addition to the source spectrum that can only be removed during the analysis stage using data from both the Earth's atmospheric emission and calibration source observations.

The signal received at the detector is derived by defining the signals in port 1 and 2. The emission due to a source (astronomical, the Earth's atmosphere, instrument) is represented using the source function $J(\nu)$ (§2.2.1). Port 1 continuously views a liquid nitrogen (LN_2) calibration source. The signal in this port is given by,

$$S_{port1} = G(J_{LN_2}\Omega_b\eta_I + J_I\Omega_b + O_1), \tag{4.2}$$

where G is the instrument responsivity, J_{LN_2} is the emission from the LN_2, Ω_b is the solid angle of the JCMT beam, η_I is the transmission of the instrument, J_I is the emission from the instrument, and O_1 is an offset term.

Port 2 sequentially views the astronomical source, calibration source, and the terrestrial atmosphere. When port 2 views an astronomical source the signal in the port is given by,

$$S^{source}_{port2} = G(J_S\Omega_S e^{-\tau A}\eta_I + J_A\Omega_b\eta_I + J_I\Omega_b + O_2), \tag{4.3}$$

where J_S is the emission spectrum from the astronomical source, Ω_S is the solid angle of the source, τ is the zenith optical depth of the Earth's atmosphere, A is the airmass of the observation, J_A is the emission from the atmosphere, and O_2 is an offset term. When port 2 views only the Earth's atmosphere the signal in the port is given by,

$$S^{sky}_{port2} = G(J_A\Omega_b\eta_I + J_I\Omega_b + O_2). \tag{4.4}$$

The FTS is a differential instrument; the signals received through port 1 and 2 are differenced in the interferometric measurement. The signal received by the detector when the source is in port 2 is therefore given by,

$$\begin{aligned} \Delta S_{source} &= S^{source}_{port2} - S_{port1} \\ &= G(J_S \Omega_S e^{-\tau A} \eta_I + J_A \Omega_b \eta_I - J_{LN_2} \Omega_b \eta_I + O_2 - O_1), \end{aligned} \tag{4.5}$$

and when the background sky is in port 2,

$$\begin{aligned} \Delta S_{sky} &= S^{sky}_{port2} - S_{port1} \\ &= G(J_A \Omega_b \eta_I - J_{LN_2} \Omega_b \eta_I + O_2 - O_1). \end{aligned} \tag{4.6}$$

The emission from the LN_2 and offset terms are constant and can be removed by subtraction of the sky signal from the source signal during the data analysis process. The atmospheric emission (J_A) is a variable quantity that can change significantly during the observation period. To guarantee that the term $J_A \Omega_b \eta_I$ is effectively removed from the source observations, source and atmospheric observations must be interleaved in small time intervals and the atmospheric emission must be relatively stable during the observing cycle. The observing procedure is described in §4.1.3.

To extract the source signal J_S from the source observations (Eq. 4.5) the following steps must be taken during the data analysis. Subtraction of the sky signal (Eq. 4.6) from the source signal (Eq. 4.5) gives the following source signal after subtraction,

$$S_{source} = \Delta S_{source} - \Delta S_{sky} = G(J_S \Omega_S e^{-\tau A} \eta_I). \tag{4.7}$$

Eq. 4.7 contains terms due to the Earth's atmospheric transmittance and the instrument. Observations of an astronomical source of known properties are required so that these terms can be removed from the source observations. A ratio of the source against the calibrator gives,

$$\begin{aligned} \frac{S_{source}}{S_{cal}} &= \frac{G(J_S \Omega_S e^{-\tau_S A_S} \eta_I)}{G(J_C \Omega_C e^{-\tau_C A_C} \eta_I)} \\ &= \frac{J_S \Omega_S e^{-\tau_S A_S}}{J_C \Omega_C e^{-\tau_C A_C}}, \end{aligned} \tag{4.8}$$

Table 4.1: *Coordinates and angular diameters of Neptune and Uranus for September 30, 2002.*

Source	Right Ascension HR MN	Declination ° ′	Angular Diameter ″
Neptune	20 42	-18 07	2.310
Uranus	21 51	-13 46	3.659

from which the source spectrum J_S can be recovered. In §2.5 the criteria for calibrator selection were discussed and Uranus and Mars were determined to be the best targets. Each set of observations with the FTS was accompanied with observations of one or both of these calibration sources.

4.1.3 Observations

The MZ FTS observations of Neptune were performed on September 30, 2002. Uranus was selected as the calibration source because it had similar rise and set times as Neptune and the two objects were separated in the sky by 17°. The coordinates and angular diameters of Neptune and Uranus for the date of observation are given in Table 4.1. The FTS was operated at a low resolution (1.8 GHz) because of the low spectral content of the tropospheric CO absorption line in Neptune (Fig. 4.1). This provided a significant advantage in observing efficiency since low resolution scans were short (∼10 s) compared with the scans at maximum resolution (∼1 min.).

Interferograms were obtained in groups: 5 scans on source (Neptune or Uranus) followed by 5 scans of the Earth's atmosphere (sky, hereafter). The telescope pointing offset for the sky observations was calculated such that each set of sky observations took place at nominally the same coordinates on the sky as the preceding set of source observations. This observing pattern was repeated over the entire observing period with pointing and focus checks interleaved approximately every 30 minutes.

Table 4.2: *FTS observing times of Neptune and Uranus*

Source	Start Date (HST) YYYY/MM/DY	Start Time HR:MN:SS	End Date (HST) YYYY/MM/DY	End Time HR:MN:SS
Neptune	2002/09/30	18:16:38	2002/09/30	21:39:40
Uranus	2002/09/30	21:47:54	2002/10/01	00:52:54

Table 4.2 gives the observing times for the Neptune and Uranus observations. These observing times include the time for pointing and focus checks, the sky observations, and the source observations. Approximately half of the time was spent observing the sky.

4.1.4 Cancellation of atmospheric emission

It was crucial, for effective removal of atmospheric emission from the source observations, to repeat the observing cycle (see §4.1.3) in short time intervals and to match the airmass of the sky and source observations. The former was required because the water vapour content in the atmosphere can very significantly over short time periods; the latter because the atmospheric emission varies significantly with airmass.

To determine the required atmospheric stability during each observation cycle the emission from the Earth's atmosphere and Neptune were compared. Using the Neptune model with a lower atmosphere CO abundance of $0.8\text{x}10^{-6}$ the model flux of Neptune F_N was calculated using the model intensity J_N and the solid angle subtended by Neptune,

$$F_N = J_N * \frac{\pi}{4} d_N^2, \tag{4.9}$$

where d_N is the angular diameter of Neptune, in radians, for the date of observation. It is conventional to express the flux in units of Janskys where 1 Jy = $1\text{x}10^{-26}$ $\text{Wm}^{-2}\text{Hz}^{-1}$. Fig. 4.5 shows that the CO line depth in Neptune is approxi-

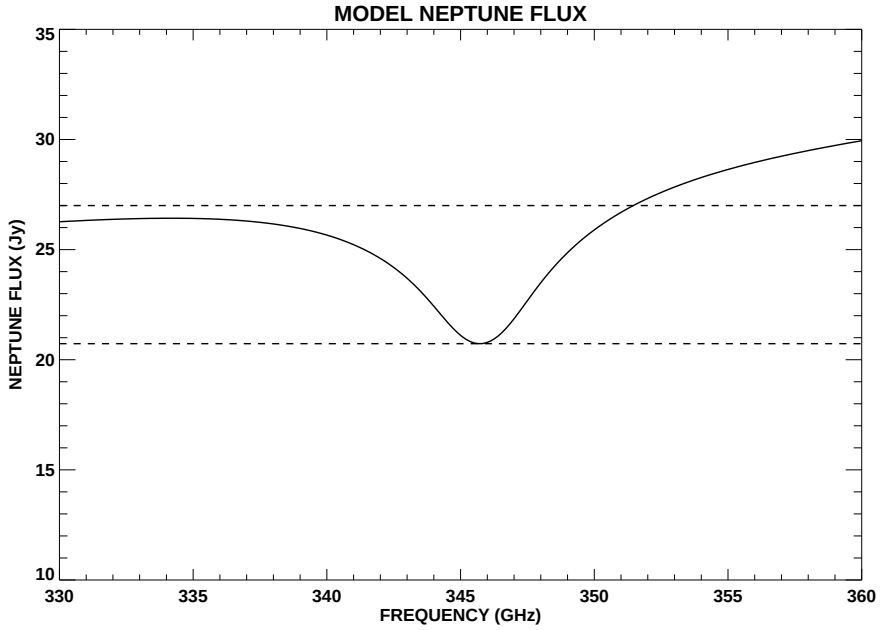

Figure 4.5: *The model Neptune flux calculated using a uniform CO abundance of* $0.8\text{x}10^{-6}$ *and an angular diameter of* $2.310''$.

mately 5 Jy. In order to measure the shape of the line it was considered necessary to achieve a precision of 10% of the line depth. The atmospheric emission must therefore not vary by more than 0.5 Jy between the source and sky observations for the line to be detected with sufficient precision.

The atmospheric emission, in the 850μm band, was estimated using the ULTRAM model developed by Chapman (2000). The output from this model is the atmospheric emission J_A as a function of frequency ν, airmass A, and zenith opacity τ. Davis *et al.* (1997) showed that τ varies linearly with pwv w at all frequencies,

$$\tau(\nu) = \tau_0(\nu) + \tau_1(\nu)w, \tag{4.10}$$

where τ_1 is the opacity per unit of pwv and τ_0 is the opacity due to all other absorbing gases. The model atmospheric emission for a specific pwv, airmass, and frequency could therefore be interpolated from the ULTRAM output.

Using similar viewing conditions as for the FTS observations, $w = 1.0$ mm and $A = 1.3$, the model atmospheric flux F_A was calculated using the ULTRAM atmo-

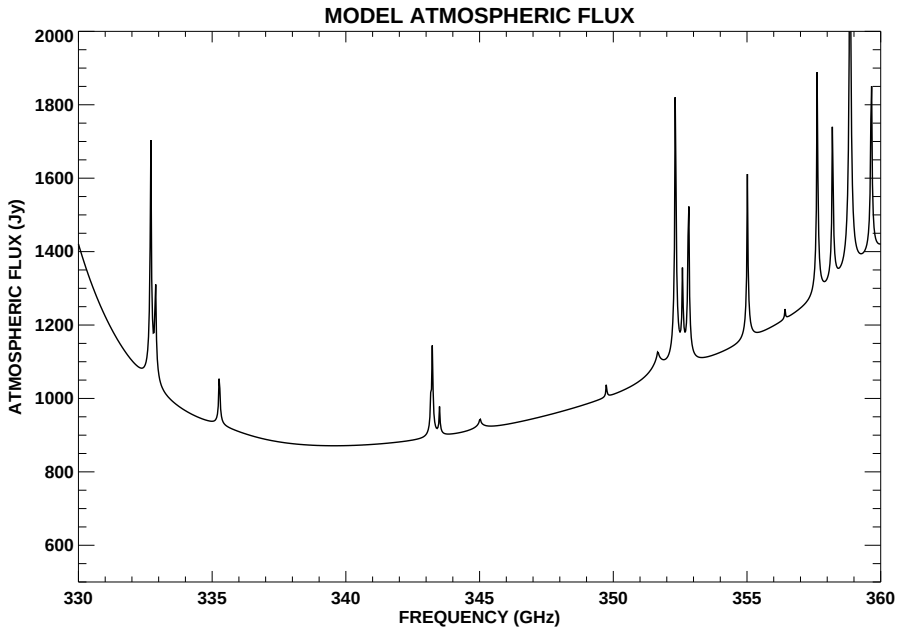

Figure 4.6: *The model atmospheric flux.*

spheric emission intensity J_A and the solid angle subtended by the 850μm beam,

$$F_A = J_A * \left[\frac{\pi B_w^2}{4\ln 2}\right], \tag{4.11}$$

where B_w is the beamwidth in radians at 850μm ($B_w \cong 14''$). The term in the square brackets results from computing the area of a Gaussian beam. The result of this calculation is shown in Fig. 4.6. The atmospheric emission at 345.8 GHz is approximately 44 times larger than the emission at that frequency from Neptune, indicating that this is a technically challenging measurement to make.

The criterion that the atmospheric emission must vary by less than $\pm$0.5 Jy during 1 cycle (5 source scans followed by 5 sky scans) corresponds to a pwv stability criterion of $\leq$ 0.0007 mm over approximately a 2 minute period. To determine if the atmospheric stability requirement was met in the 2002 observations the pwv during the observations was examined. The pwv was calculated with Eq. 1.17 using the zenith τ_{225} values as measured by the WVM. The pwv varied between 0.75 and 0.99 mm over the entire Neptune and Uranus observing period (Fig. 4.7).

The pwv values in each source-sky cycle of observations were used to calculate

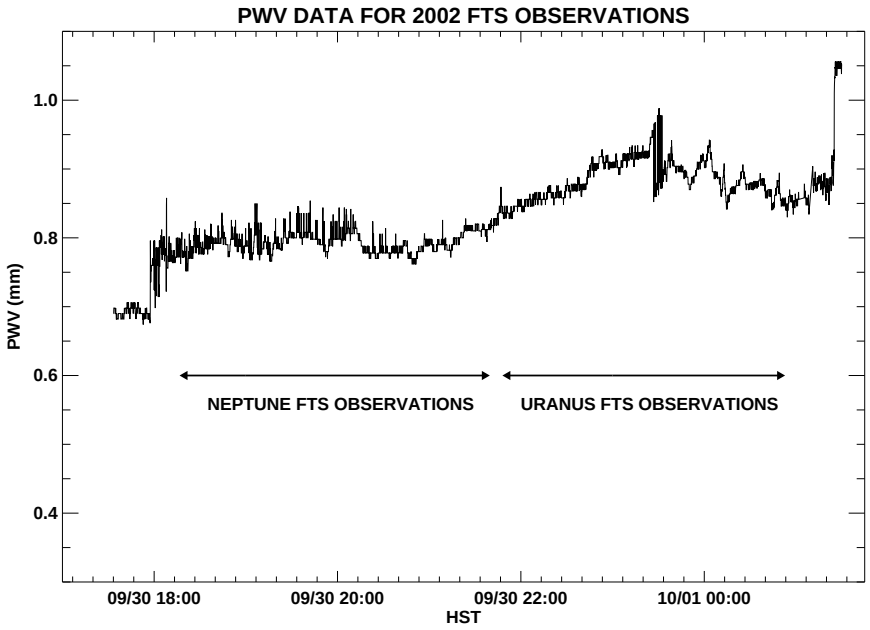

Figure 4.7: *The pwv during the Neptune and Uranus observations as measured by the WVM.*

the atmospheric stability. The mean pwv during the sky scans was subtracted from the mean pwv during the source scans to produce the results shown in Fig. 4.8. The data in each scan direction (UP and DOWN) were treated separately. The dashed curves in Fig. 4.8 indicate the pwv difference required to meet the emission stability requirement; only 7% and 3% of the Neptune and Uranus cycles respectively fall within this range. This indicates that the stability criterion was clearly not met, the implications of which will be discussed in §4.1.8.

4.1.5 Analysis

The analysis of the FTS data was performed using pipeline software written using the Interactive Data Language (IDL®). A schematic of the analysis pipeline is shown in Fig. 4.9.

UP and DOWN interferograms were produced for each scan of the FTS. These interferograms were treated separately for the analysis pipeline until step 5. In the interest of simplicity, the analysis pipeline shows the steps for analyzing only one set

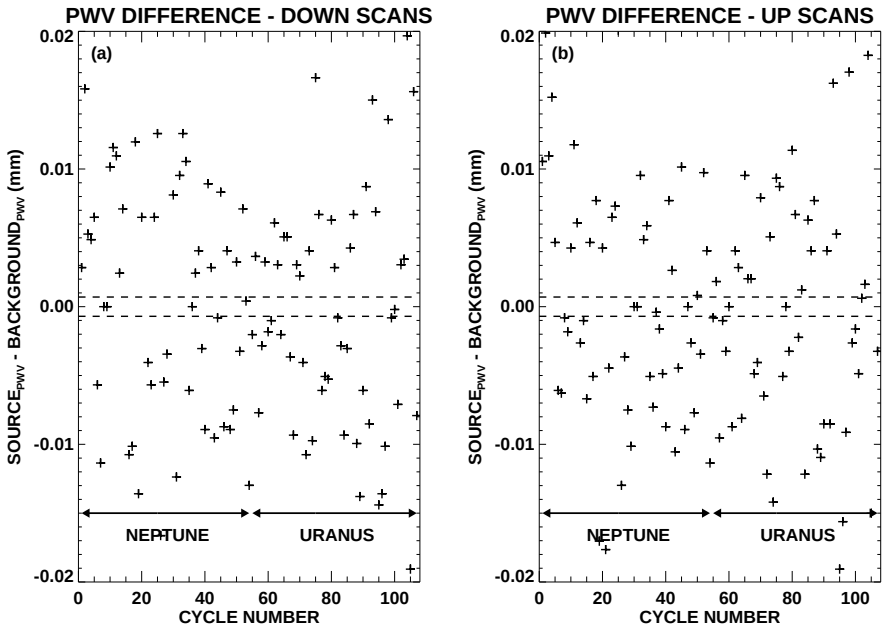

Figure 4.8: *The pwv difference, in each cycle, during the Neptune and Uranus observations. The pwv differences from the DOWN scans are shown in (a) and (b) gives the pwv differences for the UP scans.*

of data. In reality, steps 1 to 4 were repeated for both the UP and DOWN scans and at the average stage (step 5) all of the data were combined.

STEP 1: Each interferogram was manually inspected for transients such as cosmic rays.

When a cosmic ray intercepts the detector it deposits a large amount of energy causing a spike in the interferogram. Cosmic ray spikes occurred approximately once in 20 interferograms and were easily removed by linear interpolation between the data points before and after the transient. Whenever an extremely energetic cosmic ray intercepted the detector it took many data points for the detector to recover, resulting in a corrupted interferogram; these files were discarded. Very few interferograms in the 2002 data set were discarded at this stage.

STEP 2: The interferograms were Fourier transformed to spectra.

The interferogram is a record of the intensity versus path difference produced by the spectrometer (Fig. 4.10). It is related to the spectrum (intensity versus

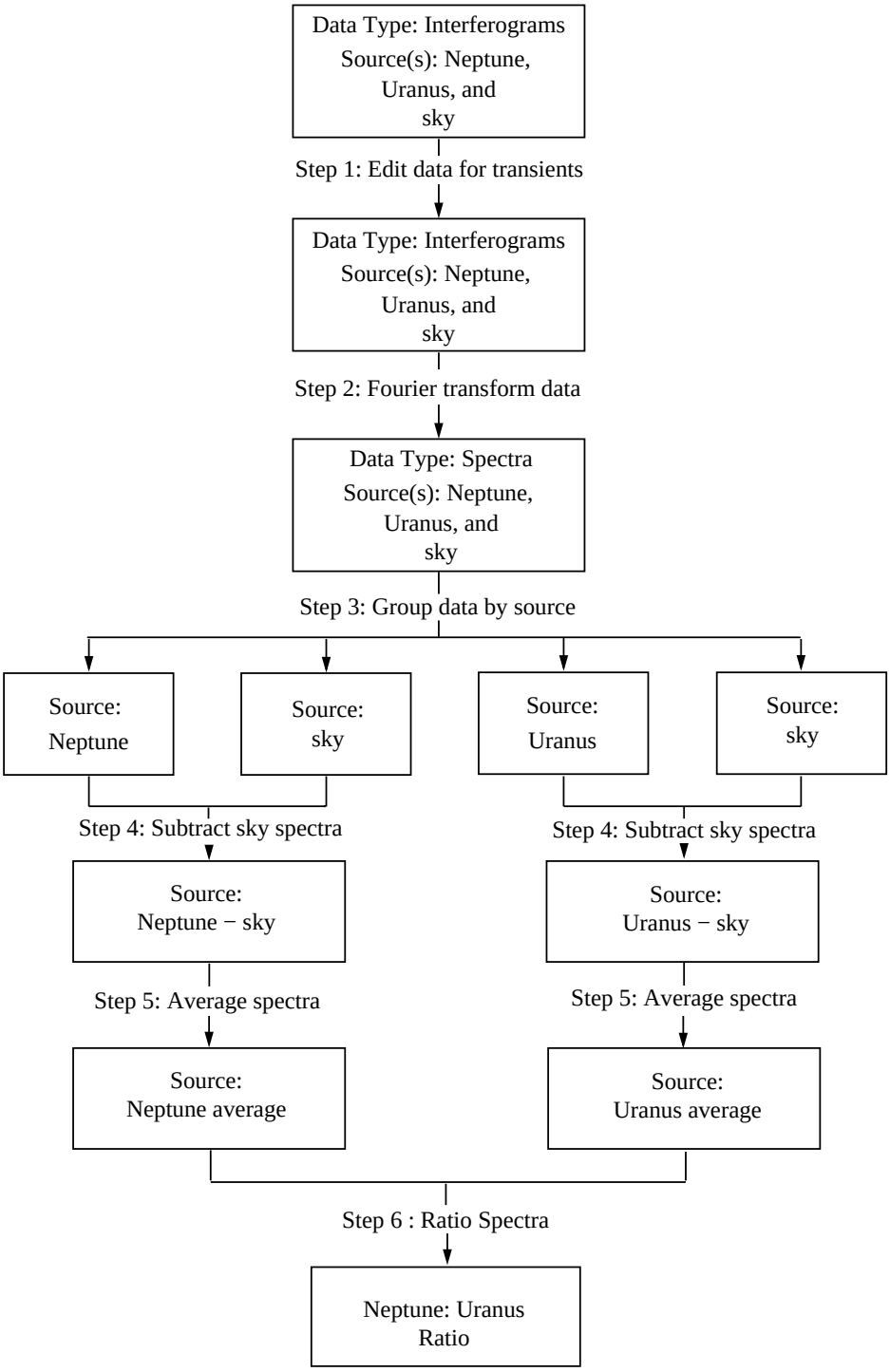

Figure 4.9: *Flow chart of the FTS analysis pipeline.*

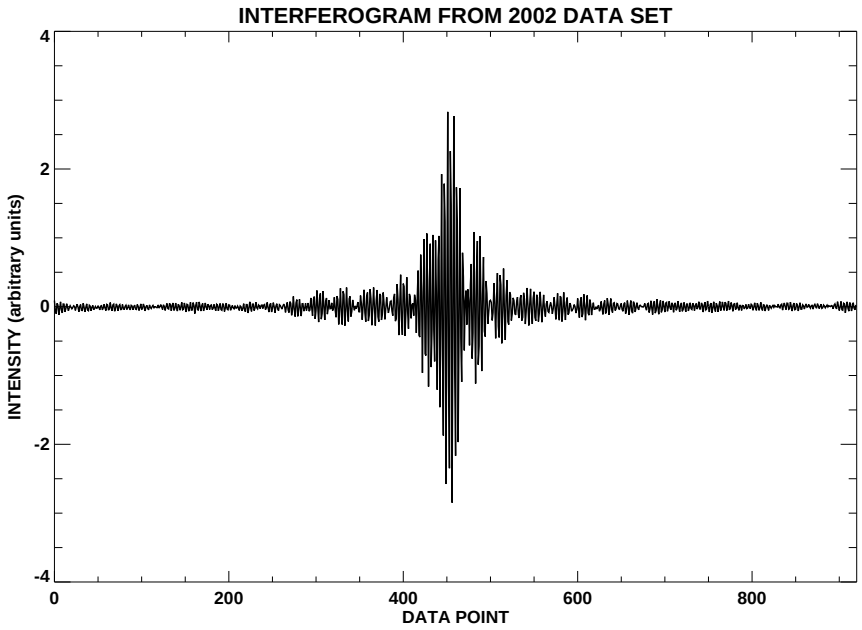

Figure 4.10: *An interferogram from the MZ FTS.*

wavenumber) through the Fourier transform,

$$S(\widetilde{\nu}) = \mathcal{F}\{i(x)\} = \int_{-\infty}^{+\infty} i(x) e^{-j2\pi\widetilde{\nu}x} dx, \tag{4.12}$$

where $j = \sqrt{-1}$, x is the path difference, $i(x)$ is the interferogram, and $S(\widetilde{\nu})$ is the spectrum. It is possible to recover $i(x)$ from $S(\widetilde{\nu})$ through the inverse Fourier transform,

$$i(x) = \mathcal{F}^{-1}\{S(\widetilde{\nu})\} = \int_{-\infty}^{+\infty} S(\widetilde{\nu}) e^{j2\pi\widetilde{\nu}x} d\widetilde{\nu}. \tag{4.13}$$

The quantities $i(x)$ and $S(\widetilde{\nu})$ are referred to as a Fourier transform pair because they are related through the Fourier transform ($i(x) \Leftrightarrow S(\widetilde{\nu})$) (Brigham 1974).

The interferogram is not recorded continuously over path length, but in discrete steps of path difference spaced by 32 μm. The continuous Fourier transform (Eq. 4.12) must therefore be converted to a discrete Fourier transform to compute the spectrum from the discrete interferogram. The discrete Fourier transform is given by the following relation,

$$S\left(\frac{n}{NX}\right) \equiv \sum_{k=0}^{N-1} i(kX) e^{-j2\pi nk/N} \quad n = 0, 1, ..., N-1, \tag{4.14}$$

where n and k are integers, N is the total number of samples in the interferogram, and X is the path difference sample interval. The computation time for Eq. 4.14 is proportional to N^2 and requires excessive machine time for large values of N, indicating that wide application of this method was historically not practical. Development of the fast Fourier transform algorithm (FFT) by Cooley and Tukey (1965) reduced the number of computations to $Nlog_2N$ (Brigham 1974). This algorithm was used to compute the Fourier transform of the FTS data.

The Fourier transform integral (Eq. 4.12) has infinite limits for the optical path difference. In reality, the spectrometer has a finite optical path length. It is therefore necessary to compare the transform of a monochromatic source using both infinite and finite limits to determine the effect this will have on the computed spectrum. The spectrum of the monochromatic source is represented using the Dirac delta function ($\delta(\widetilde{\nu})$) at $\widetilde{\nu} = 0$. Employing the properties of the delta function the interferogram is given by,

$$\begin{aligned} i(x) &= \int_{-\infty}^{+\infty} \delta(\widetilde{\nu}) e^{j2\pi\widetilde{\nu}x} d\widetilde{\nu} \\ &= e^{j2\pi(0)x} \\ &= 1, \end{aligned} \tag{4.15}$$

which indicates that $S(\widetilde{\nu}) = \delta(\widetilde{\nu})$ and $i(x) = 1$ are a Fourier transform pair ($1 \Leftrightarrow \delta(\widetilde{\nu})$) (Brigham 1974).

If the spectrometer can only scan from $x = -L$ to $x = L$, a different spectrum is produced,

$$\begin{aligned} S(\widetilde{\nu}) &= \int_{-L}^{+L} 1 \cdot e^{-j2\pi\widetilde{\nu}x} dx \\ &= 2L \,\mathrm{sinc}(2\pi\widetilde{\nu}L), \end{aligned} \tag{4.16}$$

where the sinc function is given by $\frac{\sin x}{x}$. The recovered spectrum has changed from a delta function at $\widetilde{\nu} = 0$ to a *sinc* function centred at $\widetilde{\nu} = 0$ (Fig. 4.11). Eq. 4.16 is called the instrument line shape function (ILS). The result of the finite limits of the spectrometer is to spread the energy over a finite frequency width and produce sidelobes that drop approximately 22% below zero (Bell 1972).

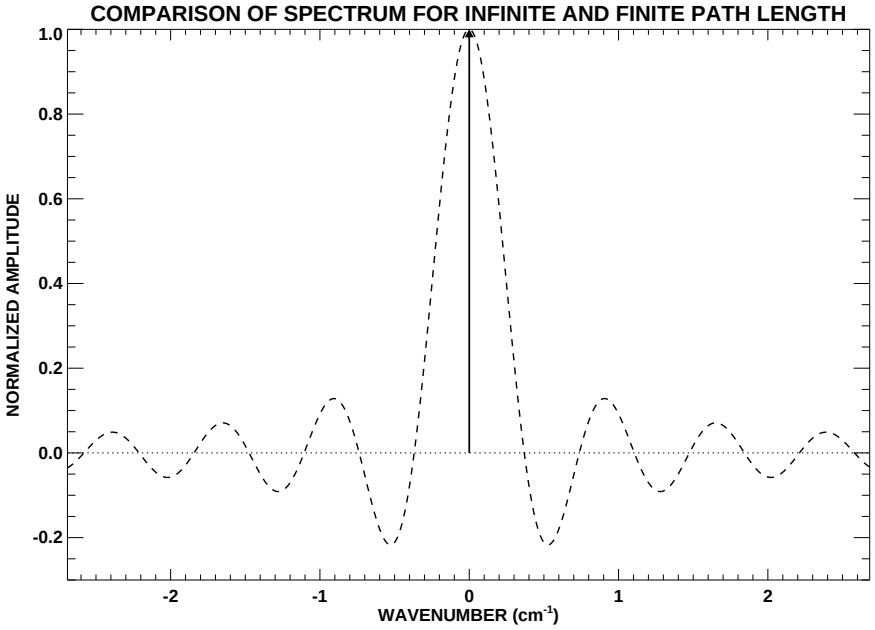

Figure 4.11: *The spectrum that results from a monochromatic source with interferogram $i(x) = 1$ with integration over infinite limits (solid) and finite limits (dashed).*

A process called apodization is applied to the interferogram before transformation to reduce the sidelobes. This involves multiplying the interferogram by an apodizing function. Apodizing functions are constructed so that the sidelobes in the resultant spectrum are reduced. A major drawback of apodization is that the FWHM of the peak intensity in the spectrum becomes broader, thereby reducing the resolution of the data being apodized. There are many apodization functions that reduce the sidelobes and resolution by various amounts. It was necessary, for this analysis, to reduce the sinusoidal modulation in the data as much as possible. This required an apodization function that significantly reduced the sidelobes in the ILS. The apodizing function chosen for the FTS analysis was therefore the modified Blackman-Harris function given by,

$$\begin{aligned} A(x) &= 0.355766 + 0.487395\ \cos\left(\frac{\pi x}{L}\right) + \\ &\quad 0.144234\ \cos\left(\frac{2\pi x}{L}\right) + \end{aligned}$$

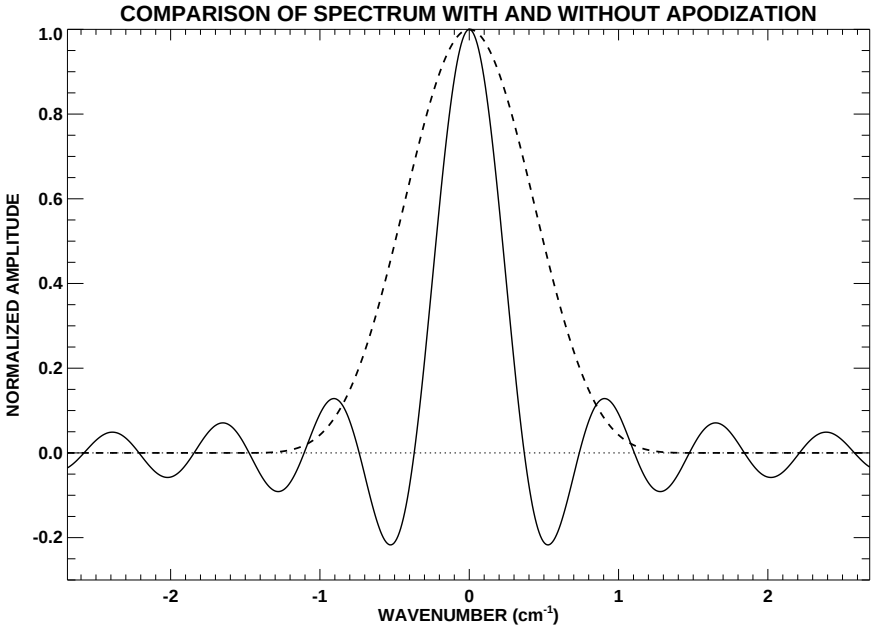

Figure 4.12: *The spectrum that results from Fourier transforming* $i(x) = 1$ *over finite limits (solid). The spectrum that results from Fourier transforming* $i(x) = 1$ *multiplied by Eq. 4.17 over finite limits (dashed).*

$$0.012605\ \cos\left(\frac{3\pi x}{L}\right), \tag{4.17}$$

(Learner *et al.* 1995). This function was added to the suite of apodizing functions available in the pipeline after a review of the literature by Tahić (2004). Multiplication of this function by $i(x) = 1$, and transforming, gives the following apodized instrument line shape,

$$S(\widetilde{\nu}) = \frac{2L\ \mathrm{sinc}(2\pi\widetilde{\nu}L)(3.201894 - 1.134000\widetilde{\nu}^2L^2 + 0.095616\widetilde{\nu}^4L^4)}{(1 - 4\widetilde{\nu}^2L^2)(1 - \widetilde{\nu}^2L^2)(9 - 4\widetilde{\nu}^2L^2)}. \tag{4.18}$$

Fig. 4.12 compares the result of transforming $i(x) = 1$ over finite limits with and without apodization. Eq. 4.18 produces a broader central peak, by a factor of 2.24, but has minimal sidelobes. By applying this function to the data the resolution is degraded from 1.8 GHz to 4 GHz.

Phase errors in the interferogram will corrupt the spectrum and must therefore be removed before transformation. The interferogram, in the ideal case, is a symmetric function of the path difference. The spectrum is calculated using the Fourier

transform over a finite path difference,

$$S(\widetilde{\nu}) = \int_{-L}^{+L} i(x) e^{-j2\pi\widetilde{\nu}x} dx. \tag{4.19}$$

Using Euler's equation, Eq. 4.19 is rewritten as,

$$S(\widetilde{\nu}) = \int_{-L}^{+L} i(x)\cos(2\pi\widetilde{\nu}x)dx - j\int_{-L}^{+L} i(x)\sin(2\pi\widetilde{\nu}x)dx. \tag{4.20}$$

The sine function is odd and $i(x)$, in the ideal case, is even, indicating that the second term of Eq. 4.20 is zero. The resulting spectrum is a real function of the form,

$$S(\widetilde{\nu}) = \int_{-L}^{+L} i(x)\cos(2\pi\widetilde{\nu}x)dx. \tag{4.21}$$

In actuality, the interferogram is usually asymmetric. The asymmetry results from not precisely sampling the zero path difference point and misalignments in the instrument. The asymmetry of the interferogram causes the second term of Eq. 4.20 to be non-zero. The spectrum that results from this transformation has real and imaginary parts,

$$S(\widetilde{\nu}) = Re(\widetilde{\nu}) + jIm(\widetilde{\nu}). \tag{4.22}$$

An example of the real and imaginary output from Fourier transforming the interferogram in Fig. 4.10 is shown in Fig. 4.13. The amplitude $|S(\widetilde{\nu})|$ and phase $\phi(\widetilde{\nu})$ of the transformation are given by,

$$|S(\widetilde{\nu})| = \sqrt{Re(\widetilde{\nu})^2 + Im(\widetilde{\nu})^2}, \tag{4.23}$$

$$\phi(\widetilde{\nu}) = \tan^{-1}\left[\frac{Im(\widetilde{\nu})}{Re(\widetilde{\nu})}\right], \tag{4.24}$$

(Brigham 1974).

When a phase error $\phi(\widetilde{\nu})$ is introduced into the data it has the following effect,

$$\begin{aligned} i(x) &= \int_{-\infty}^{+\infty} S(\widetilde{\nu}) e^{j[2\pi\widetilde{\nu}x + \phi(\widetilde{\nu})]} d\widetilde{\nu} \\ &= \int_{-\infty}^{+\infty} S_c(\widetilde{\nu}) e^{j2\pi\widetilde{\nu}x} d\widetilde{\nu}, \end{aligned} \tag{4.25}$$

where $S(\widetilde{\nu})$ is the spectrum that results when there is no phase error and the computed spectrum $S_c(\widetilde{\nu})$ is given by,

$$S_c(\widetilde{\nu}) = S(\widetilde{\nu}) e^{j\phi(\widetilde{\nu})}. \tag{4.26}$$

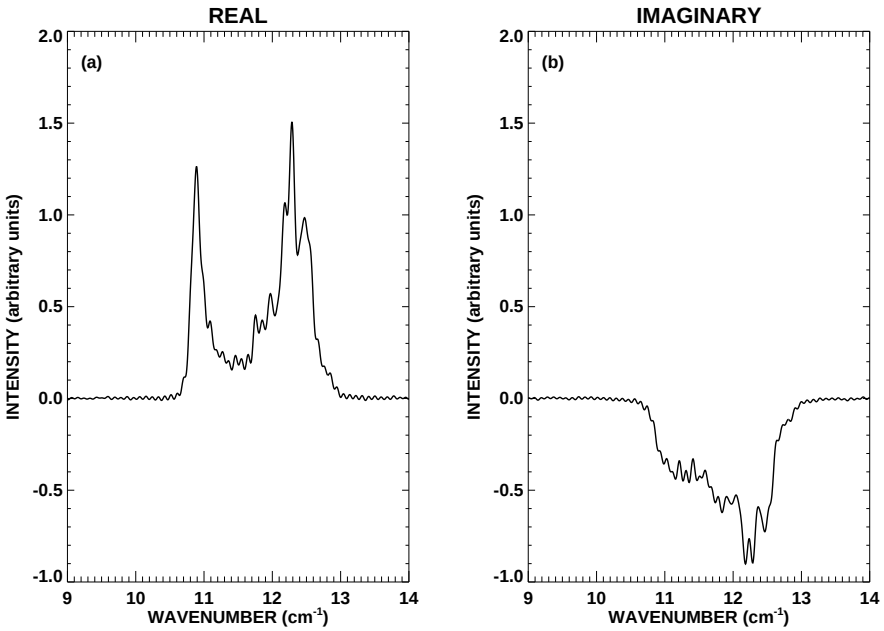

Figure 4.13: *The real (a) and imaginary (b) parts of the transformation of the interferogram shown in Fig. 4.10.*

An example of the phase error inherent in FTS data is shown in Fig. 4.14. The spectrum corrected for the phase error is found using,

$$S(\widetilde{\nu}) = S_c(\widetilde{\nu})e^{-j\phi(\widetilde{\nu})}, \tag{4.27}$$

(Bell 1972). This phase correction method effectively removes the imaginary component of the spectrum. Fig. 4.15 shows the real and imaginary components of the transformation after phase correction.

The transformation from interferograms to spectra was therefore a three step process in which:

(a) The interferogram was apodized using the selected apodizing function;

(b) The fast Fourier transform was used to compute the transform of the apodized interferogram; and,

(c) A phase correction was applied to the real and imaginary parts of the Fourier transformed interferogram.

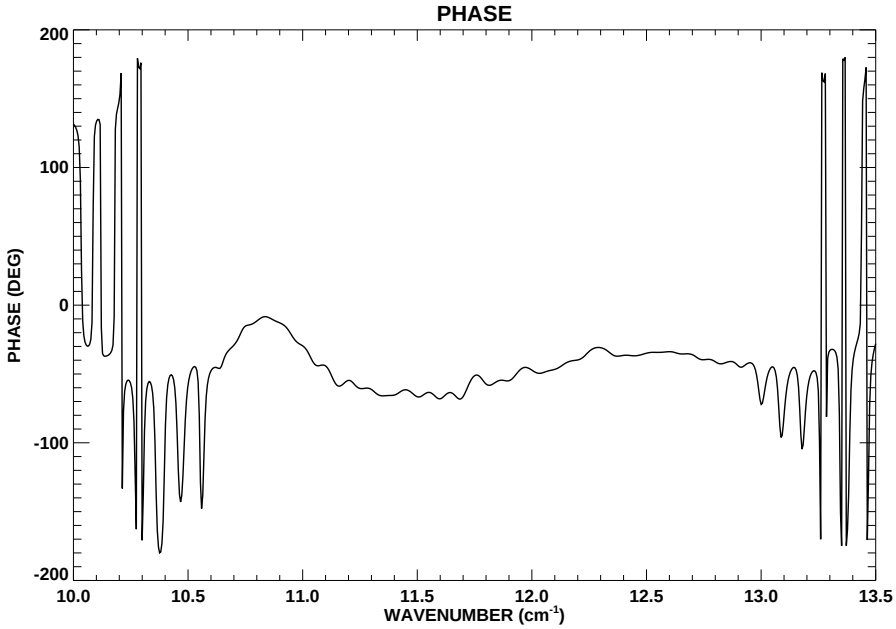

Figure 4.14: *The phase error inherent in the interferogram shown in Fig. 4.10.*

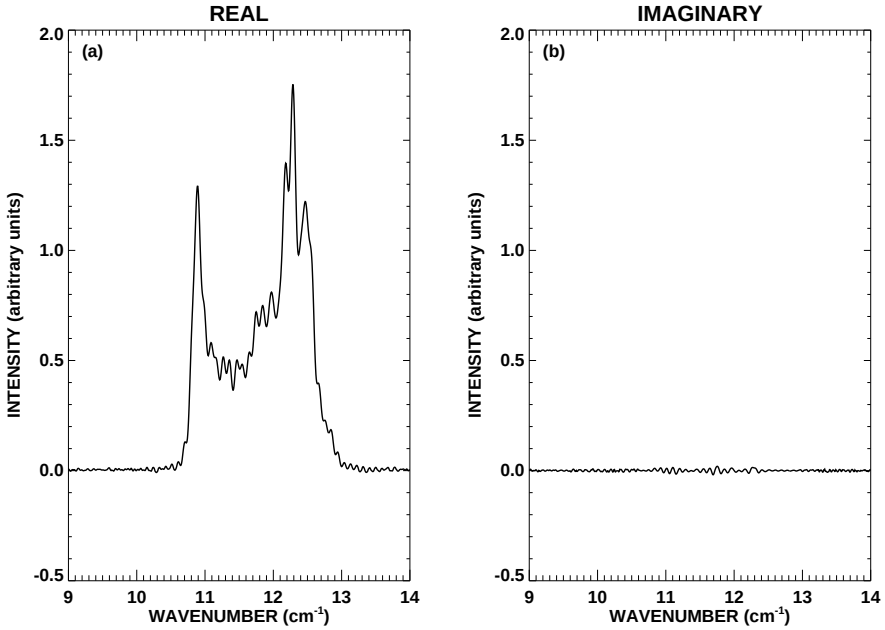

Figure 4.15: *The real (a) and imaginary (b) parts of the transformation after the phase correction is applied.*

This produced a phase corrected, apodized spectrum for each interferogram in the data set.

STEP 3: The spectra were group-averaged by source.

Before the data were group-averaged each spectrum was assigned airmass and pwv values to allow correction for the atmospheric transmittance at later stages of the pipeline. The airmass was assigned to each scan by linear interpolation, in time, from airmass values recorded approximately every minute while at the telescope. The pwv was monitored during the observations using the WVM (Fig. 4.7). In 2002, the τ_{225} was measured in the telescope line-of-sight approximately every 6 s. The FTS scans were approximately 10 s in duration indicating that there were at most two WVM measurements per scan. In most cases there was one measurement per scan, but in the instance of two measurements per scan the WVM data were averaged and the average value was assigned to the scan. The τ_{225} values were converted to pwv using Eq. 1.17.

The sources were observed in a cycle of 5 scans on source, followed by 5 scans on a sky position. There were a total of 54 Neptune cycles followed by 53 Uranus cycles during the observing period. The spectra at this stage were group-averaged by source to produce one spectrum for each source in each cycle of the observations,

$$\overline{N_i} = \frac{\sum_{j=1}^{j=n} N_{ij}}{n} \qquad i = 1, 2, ..., 54 \tag{4.28}$$

$$\overline{NB_i} = \frac{\sum_{j=1}^{j=n} NB_{ij}}{n} \qquad i = 1, 2, ..., 54 \tag{4.29}$$

$$\overline{U_i} = \frac{\sum_{j=1}^{j=n} U_{ij}}{n} \qquad i = 1, 2, ..., 53 \tag{4.30}$$

$$\overline{UB_i} = \frac{\sum_{j=1}^{j=n} UB_{ij}}{n} \qquad i = 1, 2, ..., 53, \tag{4.31}$$

where $\overline{N_i}$, $\overline{NB_i}$, $\overline{U_i}$, $\overline{UB_i}$ are respectively, for cycle i, the averaged Neptune spectra, the averaged sky spectra for Neptune, the averaged Uranus spectra, and the averaged sky spectra for Uranus; N_{ij}, NB_{ij}, U_{ij}, UB_{ij} are the j^{th} Neptune, Neptune sky, Uranus, and Uranus sky spectra in cycle i; and n is the number of spectra for each source in the cycle ($n \leq 5$). The error in each grouping was calculated and

propagated through the analysis procedure to assist in statistically filtering out data of poor quality. The group error was determined using the standard deviation in the mean given by,

$$\delta\overline{N_i} = \sqrt{\frac{1}{n(n-1)}\sum_{j=1}^{j=n}(N_{ij}-\overline{N_i})^2} \qquad i=1,2,...,54 \tag{4.32}$$

$$\delta\overline{NB_i} = \sqrt{\frac{1}{n(n-1)}\sum_{j=1}^{j=n}(NB_{ij}-\overline{NB_i})^2} \qquad i=1,2,...,54 \tag{4.33}$$

$$\delta\overline{U_i} = \sqrt{\frac{1}{n(n-1)}\sum_{j=1}^{j=n}(U_{ij}-\overline{U_i})^2} \qquad i=1,2,...,53 \tag{4.34}$$

$$\delta\overline{UB_i} = \sqrt{\frac{1}{n(n-1)}\sum_{j=1}^{j=n}(UB_{ij}-\overline{UB_i})^2} \qquad i=1,2,...,53, \tag{4.35}$$

The average pwv and airmass for each cycle of Eqs. 4.28, 4.29, 4.30, and 4.31 were calculated and assigned to each group averaged spectrum.

STEP 4: The sky spectra were subtracted from the source spectra.

This step removed the Earth's atmospheric sky emission J_A from the source spectra (§4.1.4). Using the procedure described by Eq. 4.7 the sky spectrum was subtracted from the source spectrum in each cycle,

$$N_i = \overline{N_i} - \overline{NB_i} \qquad i=1,2,...,54 \tag{4.36}$$

$$U_i = \overline{U_i} - \overline{UB_i} \qquad i=1,2,...,53, \tag{4.37}$$

where N_i and U_i are respectively the Neptune and Uranus sky subtracted spectra in each cycle i. The errors of the two spectra were added in quadrature to propagate the error through this stage of the pipeline. The pwv and airmass were propagated by averaging the values from the two spectra being subtracted.

The atmospheric emission sometimes varied significantly over the 2 minute period of a cycle, resulting in some negative differences at this stage. An average intensity was computed for spectral points between 327 and 372 GHz and spectra that had an average value below zero were removed. Of the Neptune and Uranus spectra, 14% and 3% were removed respectively.

STEP 5: The Neptune and Uranus spectra (both UP and DOWN scans) were averaged.

The remaining spectra were sorted by the increasing average of their error between 327 and 372 GHz (UP and DOWN scans included together). A running average was computed, which involved calculating the average and average error as spectra were added in order of their increasing error.

The spectra had to be corrected to a mean airmass and pwv before they could be averaged. This was accomplished using the ULTRAM model of the Earth's atmospheric transmittance (Chapman (2000); §4.1.4). Each spectrum S_i had, therefore, to be multiplied by a ratio of the Earth's atmospheric transmittance at an average pwv and airmass ($e^{-\tau_{AVG}A_{AVG}}$) and the Earth's atmospheric transmittance at the pwv and airmass ($e^{-\tau_i A_i}$) of the spectrum,

$$S_i^{corr} = S_i \left(\frac{e^{-\tau_{AVG}A_{AVG}}}{e^{-\tau_i A_i}} \right). \tag{4.38}$$

The average spectra for Neptune and Uranus were then calculated by,

$$\overline{N} = \frac{\sum_{i=1}^{n} N_i^{corr}}{n} \tag{4.39}$$

$$\overline{U} = \frac{\sum_{i=1}^{n} U_i^{corr}}{n}, \tag{4.40}$$

where $\overline{N}$ and $\overline{U}$ are the average spectra of the Neptune and Uranus data respectively, and n is the number of spectra included in the average. The error in the averaged spectrum was calculated by adding the errors, from the spectra included in the average, in quadrature.

A second quality filter was applied to the data at the average step. This was accomplished by recording the error in the average as spectra were incrementally added to the average. The average error continued to fall, as spectra were added, but eventually reached a point where adding new spectra to the average increased the error in the resultant averaged spectrum. Any files that increased the error in the averaged spectrum were removed at this point. This resulted in 11% and 9% of the remaining Neptune and Uranus spectra respectively being removed.

The remaining files were averaged to produce one spectrum for each of Neptune and Uranus. The pwv and airmass for each of the Neptune and Uranus averages

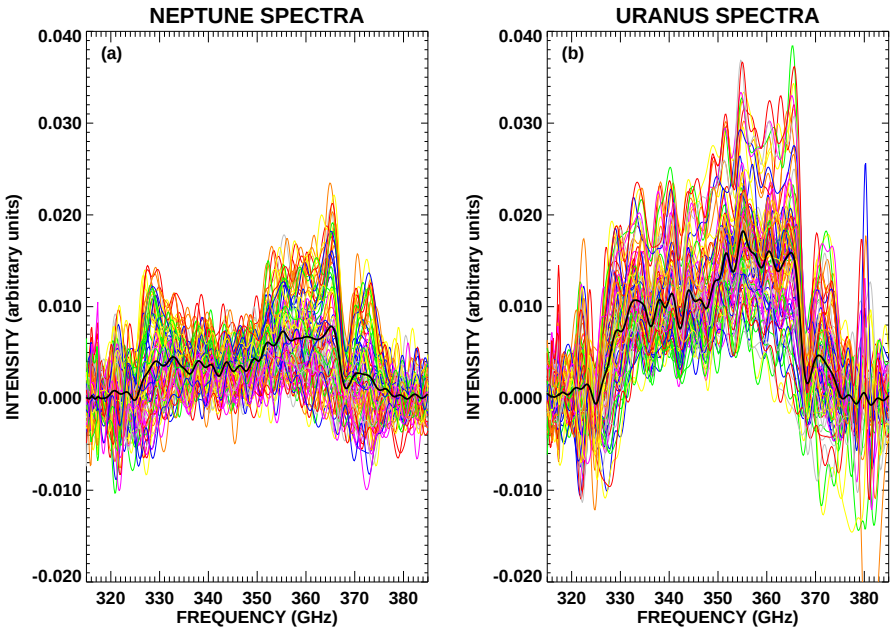

Figure 4.16: *The Neptune (a) and Uranus (b) spectra corrected to a mean airmass and pwv (coloured curves). The averaged spectrum for Neptune and Uranus are shown in black.*

were calculated by averaging the pwv and airmass from each of the spectra included in the average. Fig. 4.16 shows the corrected Neptune and Uranus spectra that were used in the average. The scatter in the spectra was used as a measure of the error in the data set, computed using the standard deviation,

$$\delta\overline{N} = \sqrt{\frac{1}{n-1}\sum_{i=1}^{n}(N_i^{corr} - \overline{N})^2} \tag{4.41}$$

$$\delta\overline{U} = \sqrt{\frac{1}{n-1}\sum_{i=1}^{n}(U_i^{corr} - \overline{U})^2}. \tag{4.42}$$

STEP 6: The ratio of the Neptune and Uranus spectra was calculated.

Eq. 4.7 contains terms due to the Earth's atmospheric transmittance and the instrument. These terms were eliminated by calculating a ratio against Uranus (Eq. 4.8) and correcting for the atmospheric transmittance in the direction of each source given by,

$$Ratio_{N:U} = \frac{\overline{N}}{\overline{U}} * \frac{e^{-\tau_U A_U}}{e^{-\tau_N A_N}}. \tag{4.43}$$

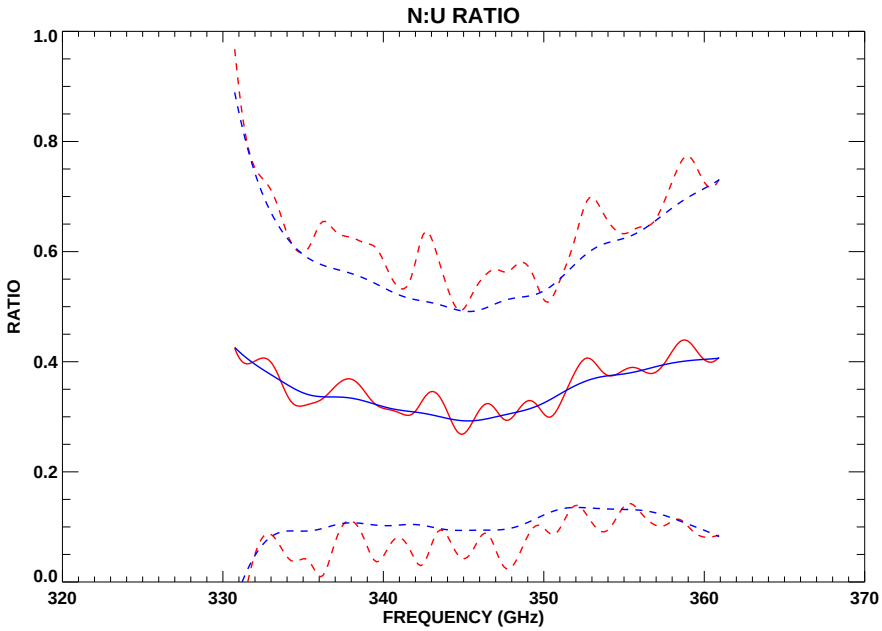

Figure 4.17: *The ratio of Neptune to Uranus with the modified Blackman-Harris apodization applied (blue) and without (red). The error in the ratio is shown with the dashed curves.*

Fig. 4.17 shows the ratio of Neptune to Uranus with the modified Blackman-Harris apodization function (Eq. 4.17) applied (dashed curve) and without (solid curve). The error in the ratio was calculated by propagating the standard deviation determined at the average stage ($\delta\overline{N}, \delta\overline{U}$) using,

$$\delta Ratio_{N:U} = Ratio_{N:U} * \sqrt{\left(\frac{\delta\overline{N}}{\overline{N}}\right)^2 + \left(\frac{\delta\overline{U}}{\overline{U}}\right)^2}. \tag{4.44}$$

4.1.6 Flux calibration

Using the calibrator model, the source spectrum was derived from the computed ratio using the following relation, which follows from Eqs. 4.8 and 4.43,

$$I_S = Ratio_{S:C} * I_C * \frac{d_C^2}{d_S^2}, \tag{4.45}$$

where I_C is the model intensity of the calibrator , d_C and d_S are respectively the angular diameters of calibrator and source, and I_S is the calculated intensity of the

source. In this situation the calibrator was Uranus and the source was Neptune. The error was determined using the following relation,

$$\delta I_S = I_S \sqrt{\left(\frac{\delta Ratio_{S:C}}{Ratio_{S:C}}\right)^2 + \left(\frac{\delta I_C}{I_C}\right)^2}, \tag{4.46}$$

where δI_C is the error in the calibrator model. This value was determined by calculating the Uranus model using temperatures profiles of ± 2 K from the nominal profile (§2.5.1). Calculations showed that the error in the Uranus model was insignificant in comparison to the error in the ratio and it was therefore neglected.

The source intensity I_S was converted to brightness temperature T_B by inverting the Planck function,

$$T_B = \frac{h\nu}{k_b}\left[\ln\left(\frac{2h\nu^3}{c^2 I_S} + 1\right)\right]^{-1}, \tag{4.47}$$

and the error in the brightness temperature δT_B was calculated using the following relation,

$$\delta T_B = \delta I_S \frac{dT_B}{dI_S}. \tag{4.48}$$

Fig. 4.18 shows the resultant Neptune brightness temperature spectrum with and without apodization applied.

4.1.7 Calibration against Mars

The detection of CO in the atmosphere of Uranus by Encrenaz *et al.* (2004), while this project was in progress, prompted an analysis of the 2002 Neptune and Uranus data using Mars as the calibration source. Mars was, unfortunately, not observed during the 2002 observing run, prompting use of the Mars observations from a different run in April 2003 for this purpose.

The 2003 Mars observations were taken at the highest resolution of 150 MHz. At this resolution the scans are $\sim$60 s in duration; to attain adequate atmospheric emission removal the observing strategy was to perform one scan on source followed by one scan on the sky. There were a total of 8 scans on Mars and 8 scans on the sky in an observing period of 24 minutes. By reducing the resolution of this data set to 1.8 GHz the integration time on source was reduced to approximately 6 minutes.

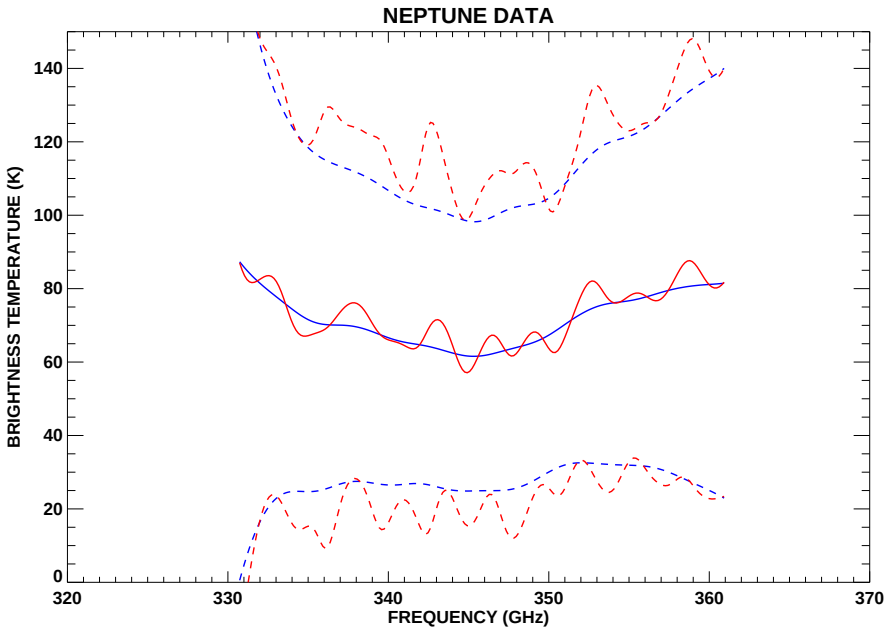

Figure 4.18: *The resultant Neptune brightness temperature spectrum with the modified Blackman-Harris apodization applied (blue) and without (red). The error in the brightness temperature is shown with the dashed curves.*

Table 4.3: *Coordinates and angular diameter of Mars for April 24, 2003.*

Source	Right Ascension HR MN	Declination ° ′	Angular Diameter ″
Mars	20 16	-21 02	8.973

The coordinates and angular diameter of Mars for the date of observation are given in Table 4.3.

The weather during the Mars observations was dry and stable with pwv values that ranged between 0.89 and 1.0 mm (Fig. 4.19).

The analysis of the Mars data proceeded in a similar fashion to the analysis pipeline used for Uranus and Neptune, the only difference being that the Mars data had to be degraded to the resolution of the Neptune and Uranus data sets. Fig. 4.20 shows the Mars spectra at the average step.

The Neptune and Uranus averages were divided by the Mars average to produce a ratio of Neptune to Mars $Ratio_{N:M}$ and Uranus to Mars $Ratio_{U:M}$. Using the Mars model (§2.5.3), the Neptune and Uranus spectra were derived from the computed ratios using Eq. 4.45. The error in the intensity spectra followed as in Eq. 4.46 with the error in the Mars model being ±5% (§2.5.3). The brightness temperature spectra of Neptune and Uranus and their associated errors were then computed using Eqs. 4.47 and 4.48 respectively. Figs. 4.21 and 4.22 show the resultant Neptune and Uranus brightness temperature spectra with and without apodization applied.

4.1.8 Results

The Neptune and Uranus model intensity spectra were convolved with the ILS to the resolution of the data set,

$$I(\nu) \star S(\nu) \equiv \int_{-\infty}^{+\infty} I(u)S(\nu - u)du, \tag{4.49}$$

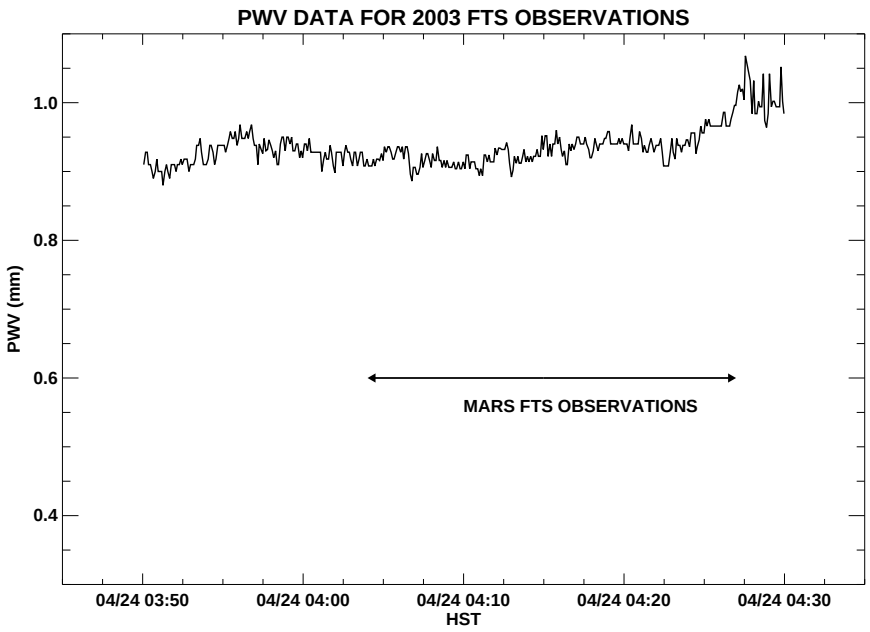

Figure 4.19: *The pwv during the 2003 Mars observations as measured by the WVM.*

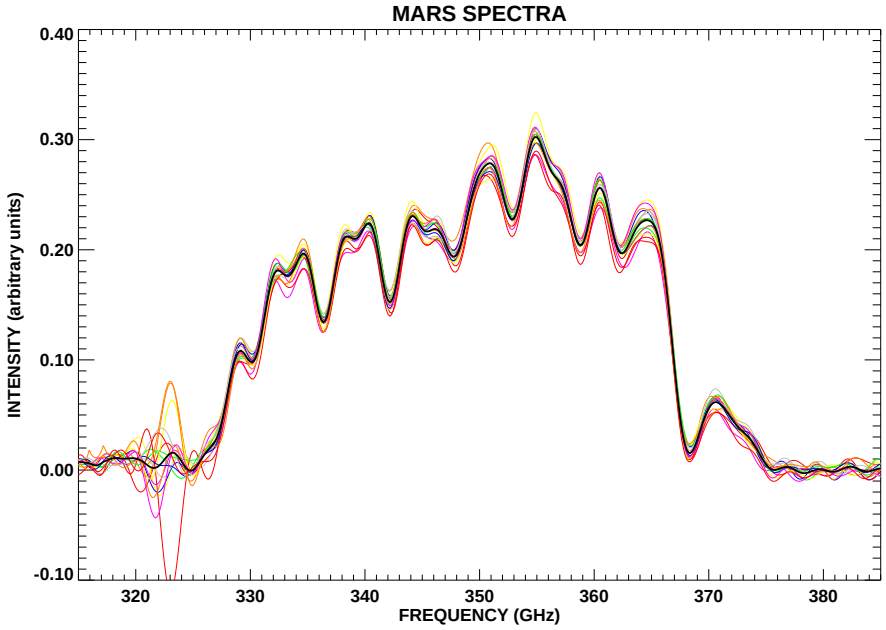

Figure 4.20: *The Mars spectra corrected to a mean airmass and pwv (coloured curves). The averaged spectrum for Mars is shown in black.*

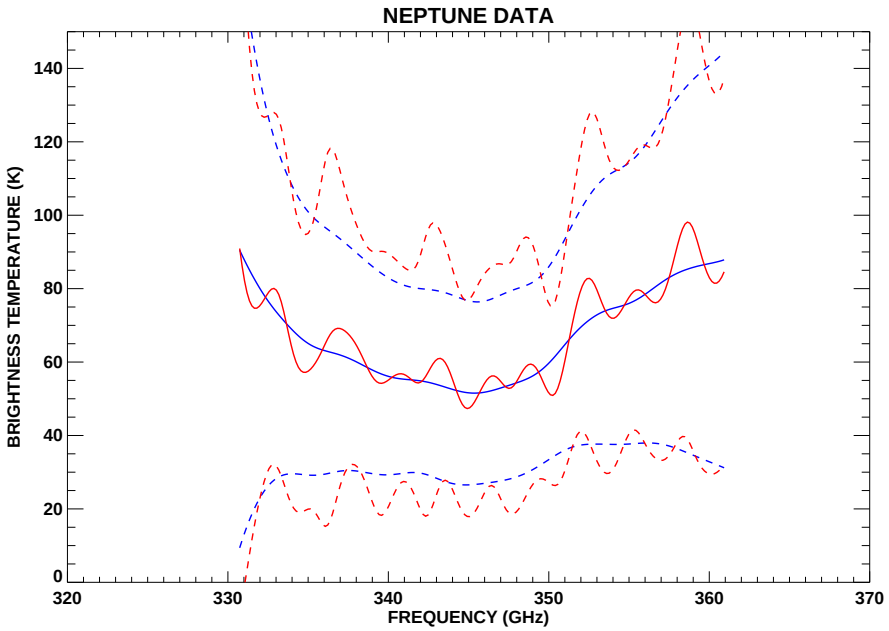

Figure 4.21: *The resultant Neptune brightness temperature spectrum with the modified Blackman-Harris apodization applied (blue) and without (red). The error in the brightness temperature is shown with the dashed curves.*

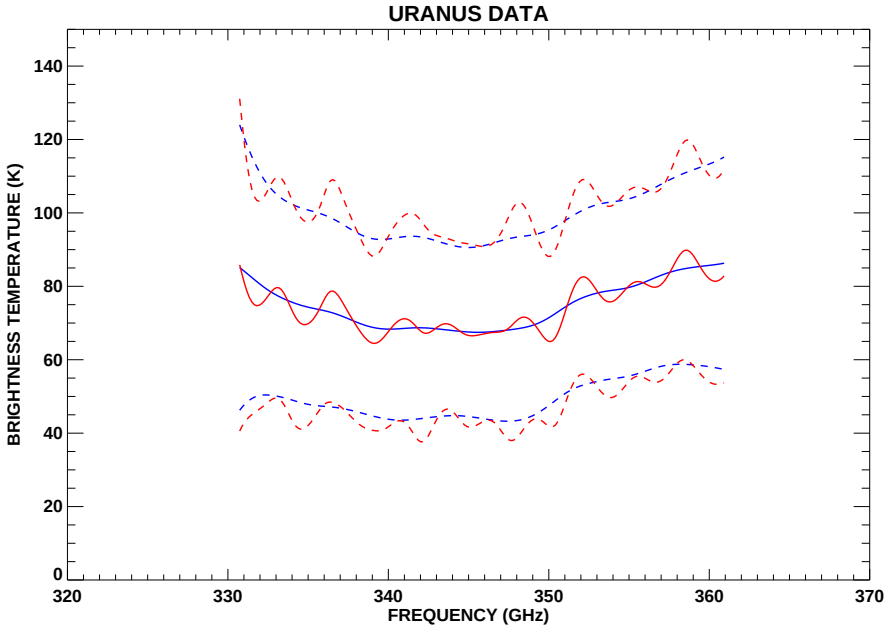

Figure 4.22: *The resultant Uranus brightness temperature spectrum with the modified Blackman-Harris apodization applied (blue) and without (red). The error in the brightness temperature is shown with the dashed curves.*

where $I(\nu)$ is the model intensity spectrum, and $S(\nu)$ is the ILS of the apodization function; in this case the ILS function was given by Eq. 4.18. The extreme uncertainty associated with the spectra of Neptune and Uranus indicate that a range of models can be fit to the data. Figs. 4.23 and 4.24 show models of various uniform CO abundances overlaid on the data.

Comparison of the Neptune data against the models indicates that the CO abundance must be higher than $0.3\text{x}10^{-6}$ (yellow curve, Fig. 4.23), but the large error prevents establishing an upper limit. In addition to the significant error in this data set, the data also exhibit a poor lineshape; the high-frequency and low-frequency wings could not be fit simultaneously. A CO abundance greater than $0.3\text{x}10^{-6}$ can therefore be established using this data set.

For the Uranus data (Fig. 4.24), all of the curves, including the case for no CO, fit within the error bars of this result. It is therefore not possible constrain the CO abundance in Uranus from this measurement.

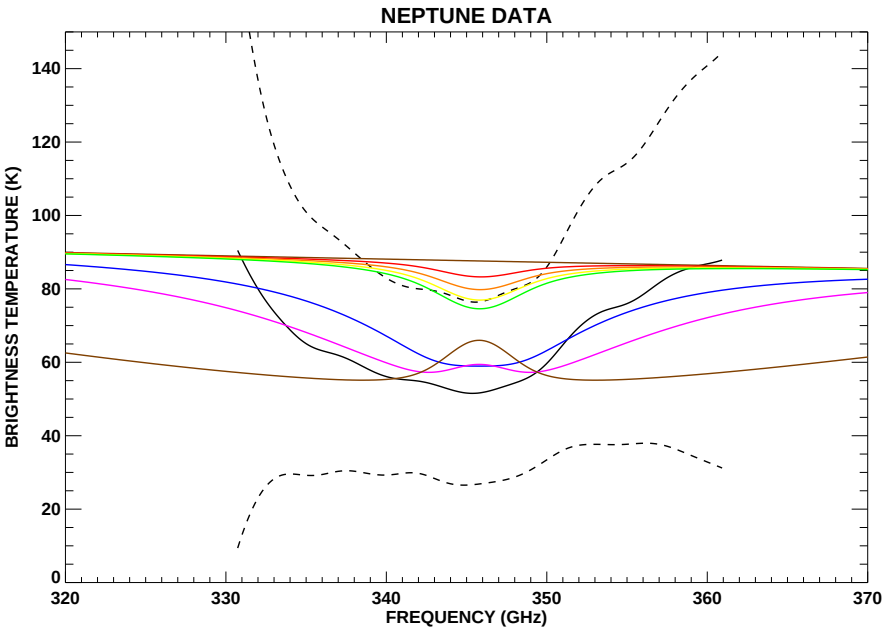

Figure 4.23: *The resultant Neptune brightness temperature spectrum with modified Blackman-Harris apodization (black). The error in the brightness temperature is shown with the dashed curves. Eight uniform CO abundance models are overlaid:* 0 *(upper brown),* $1\text{x}10^{-7}$ *(red),* $2\text{x}10^{-7}$ *(orange),* $3\text{x}10^{-7}$ *(yellow),* $4\text{x}10^{-7}$ *(green),* $4\text{x}10^{-6}$ *(blue),* $1\text{x}10^{-5}$ *(violet), and* $1\text{x}10^{-4}$ *(lower brown).*

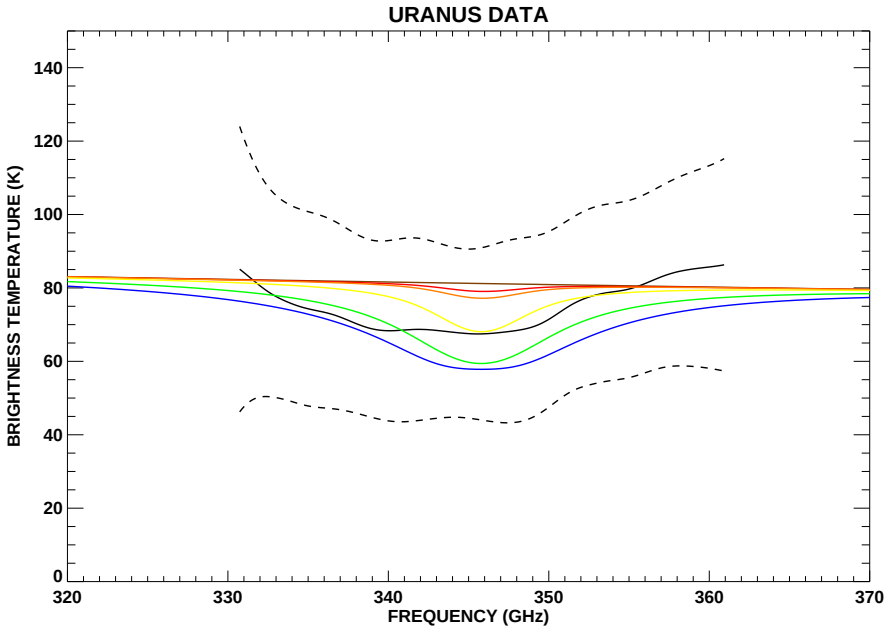

Figure 4.24: *The resultant Uranus brightness temperature spectrum with modified Blackman-Harris apodization (black). The error in the brightness temperature is shown with the dashed curves. Six uniform CO abundance models are overlaid:* 0 *(brown),* 5.0x10^{-8} *(red),* 1.0x10^{-7} *(orange),* 5.0x10^{-7} *(yellow),* 2.0x10^{-6} *(green), and* 4x10^{-6} *(blue).*

Table 4.4: *The measured and expected SNR values. The parameters used in calculating the expected SNR values for the Neptune, Uranus, and Mars data are also included. The integration times for Neptune and Uranus include the time spent observing the source and background sky (time due to pointing and focus checks was removed). The integration time listed for Mars results from the reduced resolution.*

Source	Measured SNR	T_S K	t_S hrs	d_S $''$	d_b $''$	$\Delta\nu_S$ GHz	Expected SNR
Neptune	1.2	80	2.7	2.310	14	1.8	139
Uranus	2.2	81	2.6	3.659	14	1.8	146
Mars	24.4	218	0.1	8.973	14	1.8	1099

The large errors of these data sets prompted a signal-to-noise analysis of the 2002 data. The signal-to-noise ratio (SNR) was determined by dividing the mean signal between 330 and 375 GHz by the mean noise over the same range. The mean signal was calculated using the average spectrum while the mean noise was derived from the standard deviation in the averaged spectra (see Fig. 4.16). The measured SNR values for the Neptune, Uranus, and Mars data sets are given in Table 4.4.

Observations of the Orion nebula at a resolution of 150 MHz using the MZ FTS in October 2002 produced excellent results and were used as a reference to calculate the expected SNR values for the Neptune, Uranus, and Mars observations. The Orion nebula fills the $14''$ JCMT beam and exhibits the J=3–2 CO line in emission with a brightness temperature of 21 K. A SNR of 31 was achieved in 25 minutes of observations. The SNR is defined using the following relation,

$$SNR = \frac{P}{NEP}\sqrt{t}, \tag{4.50}$$

where P is the power received in a spectral element $\Delta\nu$, *NEP* is the noise-equivalent-power, and t is the integration time (Phillips 1988). The NEP is defined as the rms, full-beam signal power for a SNR of unity in one second. The power received P per spectral element $\Delta\nu$ is given by,

$$P = IA_e\Omega\Delta\nu, \tag{4.51}$$

where I is the intensity of the source, A_e is the effective aperture of the antenna, and Ω is the solid angle of the source (Kraus 1966). In the Rayleigh-Jeans approximation,

$$I \propto T, \tag{4.52}$$

where T is the brightness temperature of the source. Applying Eq. 4.52 and $\Omega \propto d^2$, where d is the diameter of the source, to Eq. 4.51 gives,

$$P \propto T d^2 \Delta\nu, \tag{4.53}$$

and combining Eqs. 4.53 and 4.50 gives,

$$SNR \propto \frac{T d^2 \Delta\nu}{NEP}\sqrt{t}. \tag{4.54}$$

The NEP for the planetary and Orion measurements is assumed to be constant and the expected SNR for each source was found using,

$$SNR_S = \sqrt{2}\; SNR_{Or} \frac{T_S}{T_{Or}} \frac{\Delta\nu_S}{\Delta\nu_{Or}} \sqrt{\frac{t_S}{t_{Or}}} \left(\frac{d_S}{d_b}\right)^2, \tag{4.55}$$

where the variables for each planetary source and the expected SNR are given in Table 4.4. The $\sqrt{2}$ in Eq. 4.55 accounts for the planetary observations being double-sided interferograms. In all cases the expected SNR values are significantly higher (2 orders of magnitude) than the measured values.

If the dominant source of noise in this experiment is the fluctuations in the atmospheric emission over the two-minute period of a cycle of observations, then this incomplete cancellation indicates that the signal from the sky observations (Eq. 4.6) should be altered to give,

$$\Delta S_{sky} = G\left[(J_A + J')\Omega_b \eta_I - J_{LN_2}\Omega_b \eta_I + O_2 - O_1\right]. \tag{4.56}$$

where $J_A + J'$ is the atmospheric emission during the source observations plus the change in the atmospheric emission. Subtracting Eq. 4.56 from Eq. 4.5 gives,

$$S_{source} = G\eta_I (J_S \Omega_S e^{-\tau A} - J'\Omega_b). \tag{4.57}$$

An estimate of $J'\Omega_b$ is necessary to understand why the measured SNR values were so low.

In §4.1.4 the airmass values during each source-sky cycle were assumed to be identical. The fluctuation in the atmospheric emission during a source-sky cycle was therefore only due to fluctuations in pwv. Fig. 4.25 shows the airmass difference during each source-sky cycle indicating that imperfect airmass matching cannot be disregarded. This can occur because the telescope pointing for background scans is calculated on the basis of the elapsed time for the source scans, and this can vary slightly from cycle to cycle for various reasons. The variation in the model atmospheric emission at 345.8 GHz was therefore calculated using the pwv and airmass during each source and sky observation (Fig. 4.26). In §4.1.4 it was shown that the atmospheric emission could fluctuate by no more than ± 0.5 Jy between source and sky scans to ensure that Neptune was measured with sufficient precision. Fig. 4.26 shows that only 6% and 2% of the Neptune and Uranus cycles respectively fall within this range and also provides an estimate of $J'\Omega_b$ (Eq. 4.57); values as large as 20 Jy are indicated with a mean difference of ∼6.5 Jy and a standard deviation of ∼5 Jy. Fig. 4.5 indicates that the value of $J_S\Omega_S$ for Neptune is ∼21 Jy at 345.8 GHz which is reduced to ∼17 Jy when the atmospheric transmittance ($e^{-\tau A} \cong 0.8$ for Neptune observing conditions) is applied. The SNR for Neptune should therefore be approximately 3, which is comparable with the measured SNR. Incomplete cancellation of the atmospheric emission between source and background scans was therefore the cause of the poor measured SNR.

4.2 Re-analysis of 1993 FTS observations

The re-analysis of the 1993 data was prompted by the following:

1. The development of the data reduction pipeline, which allowed for correction of the Earth's atmospheric transmittance;

2. The discovery of CO in Uranus by Encrenaz *et al.* (2004) indicating that the Neptune data should be calibrated against a different source; and,

3. The high error in the 2002 results.

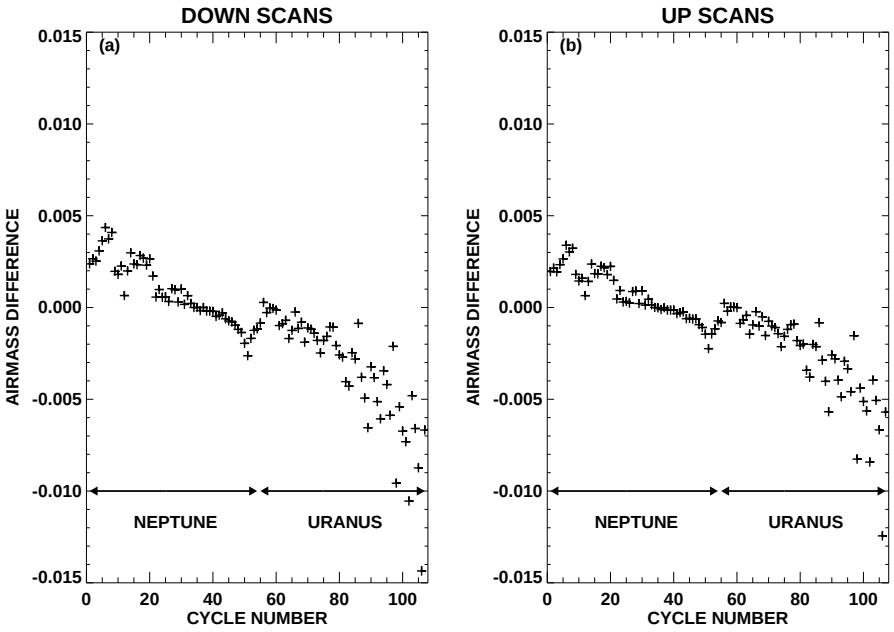

Figure 4.25: *The difference in airmass between the source and sky observations in each cycle of the Neptune and Uranus observations.*

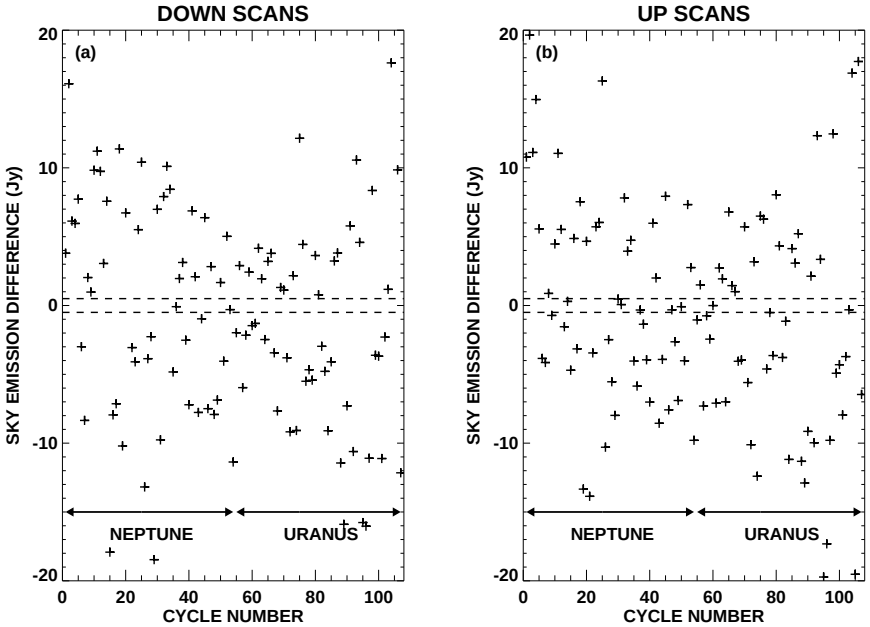

Figure 4.26: *The difference in model atmospheric emission at 345.8 GHz between the source and sky observations in each cycle of the Neptune and Uranus observations. The atmospheric stability criterion is shown as the dashed curves.*

For the re-analysis, Mars was chosen as the new calibration source allowing both the Neptune and Uranus data to be examined for CO absorption.

4.2.1 Polarizing FTS

Previous to the development of the MZ FTS a polarizing FTS, developed and built at the University of Lethbridge, was in use as a visiting instrument at the JCMT. The design of the polarizing FTS was based on the two-beam Martin-Puplett interferometer (Martin and Puplett 1969) which allowed access to two input ports. The polarizing FTS was mounted on the left Nasmyth platform to utilize the bolometric facility detector UKT14 (Duncan *et al.* 1990); at the time there was no detector system dedicated to FTS use.

The interferometer shown in Fig. 4.27 has its optical components mounted on 2 levels. Components M1, P1, M5, P2 are on the upper level, while the remaining components are on the lower level. Half of the radiation from port 1 reflects from the input polarizer P1 down to the concave mirror M2. Radiation entering port 2 reflects from the plane mirror M1 and the orthogonal component of polarization is transmitted by P1 down to M2. M2 collimates the beam and directs it to the polarizing beamsplitter BS which has its polarization axis oriented to reflect 50% and transmit 50% of the incident radiation. The reflected component is directed to the fixed mirror FM; the transmitted component is sent to the moving mirror MM. FM and MM are rooftop mirrors oriented to rotate the plane of polarization of the radiation by 90°. When the radiation encounters the beamsplitter for the second time, the opposite effect to the first encounter results (reflected is now transmitted). The resulting two beams of orthogonal polarization are directed by the plane mirror M3 to the concave mirror M4 which focuses the beam, after refection from the plane mirror M5, at the detector. The last component is the analyzer P2, whose polarization axis combines the two orthogonal beams so that maximum interference occurs (Naylor *et al.* 1994).

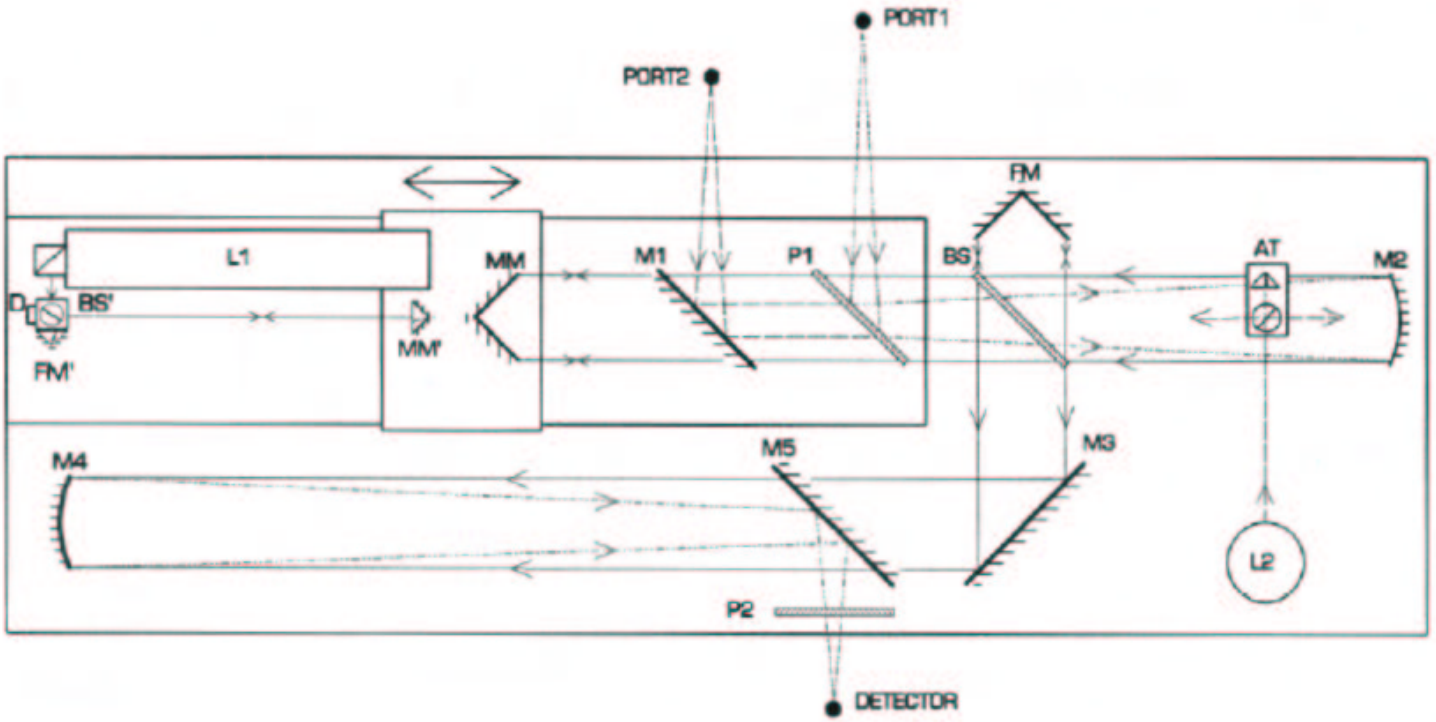

Figure 4.27: *The optical layout of the polarizing FTS (Naylor* et al. *1994).*

4.2.2 Calibration of polarizing FTS data

Input beams for both ports of this FTS were able to pass unobstructed through the telescope optics, allowing the astronomical source and the background sky to be viewed simultaneously. This was accomplished by directing one port on the source and the other port on a nearby sky position (ports separated by 65″) allowing instantaneous removal of the Earth's atmospheric sky emission.

When the astronomical source was in port 1 the signal in that port was given by,

$$S_{port1}^{source} = G(J_S \Omega_S e^{-\tau A} \eta_I + J_A \Omega_b \eta_I + J_I \Omega_b + O_1), \tag{4.58}$$

and the signal of the sky in port 2 was,

$$S_{port2}^{sky} = G(J_A \Omega_b \eta_I + J_I \Omega_b + O_2). \tag{4.59}$$

The polarizing FTS was a differential instrument; the signal received by the detector was the difference of the signal between the two ports given by,

$$\begin{aligned} \Delta S_{source}^{P1} &= S_{port1}^{source} - S_{port2}^{sky} \\ &= G(J_S \Omega_S e^{-\tau A} \eta_I + O_1 - O_2). \end{aligned} \tag{4.60}$$

The offset terms arise in part from additional optical contributions, and are in general different for the two ports. The source was therefore alternately viewed through both ports (a process known as "nodding"). The signal at the detector when the source was in port 2 and the sky was in port 1 was given by,

$$\begin{aligned} \Delta S_{source}^{P2} &= S_{port1}^{sky} - S_{port2}^{source} \\ &= G(-J_S \Omega_S e^{-\tau A} \eta_I + O_1 - O_2). \end{aligned} \tag{4.61}$$

The source had to be observed for equal amounts of time, in each port, to guarantee the offsets in both ports were well monitored. The offset signals O_1 and O_2 were removed during the analysis stage through subtraction of Eq. 4.61 from Eq. 4.60 to give,

$$S_{source} = \Delta S_{source}^{P1} - \Delta S_{source}^{P2} = 2G J_S \Omega_S e^{-\tau A} \eta_I. \tag{4.62}$$

Table 4.5: *Coordinates and angular diameters of Neptune, Uranus, and Mars for the 1993 observations.*

Source	Date (HST) MN/DY/YYYY	Integration Time hrs	Right Ascension HR MN	Declination ° ′	Angular Diameter ″
Neptune	05/10/1993	1.0	19 30	-21 05	2.300
Uranus	05/10/1993	0.4	19 35	-22 03	3.690
Mars	05/09/1993	2.0	08 35	+20 30	5.920

An astronomical source of known properties had to be observed to remove the terms G, $e^{-\tau A}$, and η_I (using Eq. 4.8). The original observations were performed using Uranus as the calibration source, but, fortuitously, data were also taken for Mars allowing either source (Uranus or Mars) to be used as the calibrator in the analysis process.

4.2.3 Observations

The observations of Neptune were performed on May 10, 1993. Uranus was the selected calibration source, because it had similar rise and set times as Neptune and the two objects were separated in the sky by only 1.5°. The later discovery of CO in Uranus by Encrenaz *et al.* (2004) indicated that a different calibration source was required for this re-analysis. The Mars observations from May 9, 1993 were therefore selected. The coordinates and angular diameters of Neptune, Uranus, and Mars for the date of observation are given in Table 4.5. The polarizing FTS was operated using the 850μm filter and an aperture of 47 mm.

The observing strategy for the Neptune and Uranus observations was to spend 70% of the observing period on Neptune and 30% on Uranus. Observations were interleaved between the two sources because of the proximity of Neptune and Uranus on the sky. The Uranus observations proceeded with three scans of Uranus in port 1 followed by three scans in port 2. The telescope was then moved to Neptune

for 10 scans of Neptune in port 2 followed by 10 scans in port 1. This procedure was repeated over the 1.4 hour observing period. A pointing and focus check was completed half way through the observations.

The observing strategy for Mars was to perform 5 scans of Mars in port 1 followed by 5 scans in port 2. This cycle was repeated over the 2 hour observing period. A pointing and focus check was completed half way through the observations.

The Neptune and Uranus data were collected at a low resolution of 1.2 GHz. Their scans took ∼10 s in comparison to the high resolution (125 MHz) scans of Mars that took ∼60 s: 264 scans on Neptune and Uranus were completed in 1.4 hrs where only 78 scans on Mars were completed in 2 hrs. The integration time on Mars was reduced to 0.4 hrs by reducing the resolution of the data to 1.2 GHz.

The weather during this run was exceptionally dry and stable. In 1993, the pwv was monitored using the CSO radiometer. This system measured the atmospheric emission at 225 GHz, every 20 minutes, at a set azimuth on the sky. The pwv was calculated with Eq. 1.17 using the zenith τ_{225} values as measured by the radiometer. The pwv varied between 0.54 and 0.62 mm over the entire Neptune and Uranus observing period (Fig. 4.28). The weather was even drier for the Mars observing period, with pwv values between 0.46 and 0.54 mm (Fig. 4.29).

4.2.4 Analysis

The analysis of the 1993 Neptune, Uranus, and Mars data proceeded using the same steps as described in §4.1.5. The major differences in this analysis procedure were:

1. The data were transformed using the Norton-Beer medium apodization function given by,

$$\begin{aligned} A(x) &= 0.26 - 0.154838\left(1-\left(\frac{x}{L}\right)^2\right) + \\ &\quad 0.894838\left(1-\left(\frac{x}{L}\right)^2\right)^2, \end{aligned} \tag{4.63}$$

   which has the following ILS,

$$S(\widetilde{\nu}) = 0.26\,\mathrm{sinc}a -$$

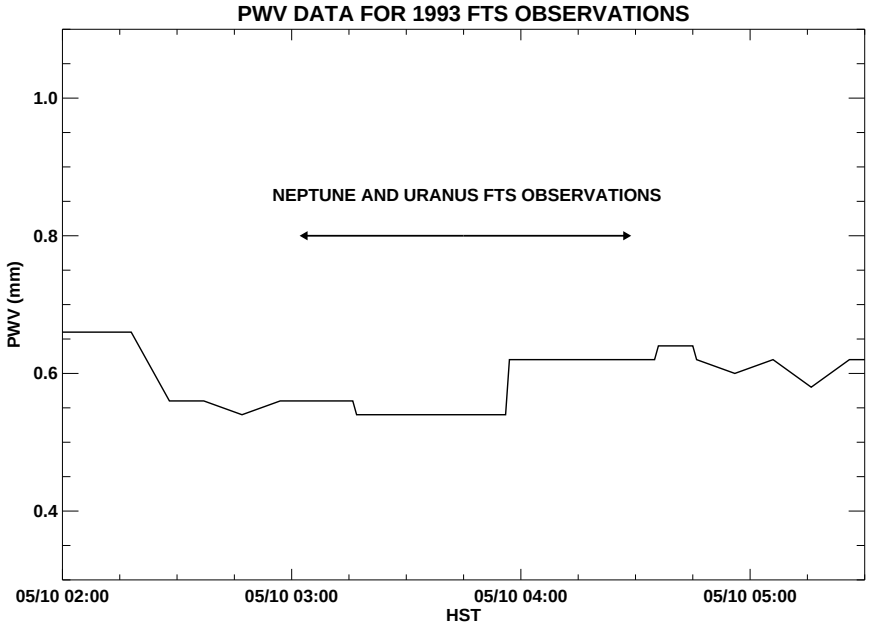

Figure 4.28: *The pwv during the Neptune and Uranus observations.*

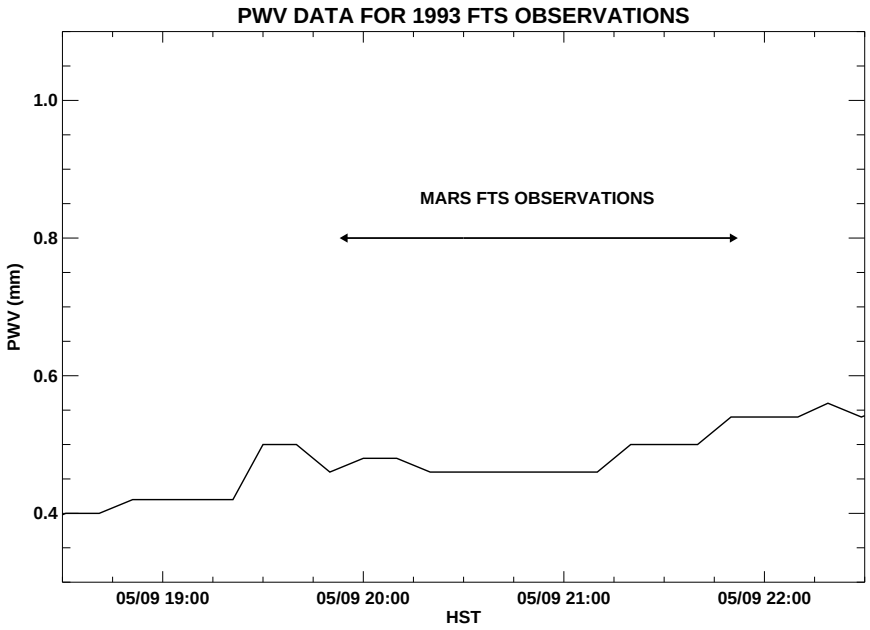

Figure 4.29: *The pwv during the Mars observations.*

$$0.154838\left(\frac{3(\mathrm{sinc}a-\cos a)}{a^2}\right)+$$
$$0.894838\left(\frac{-15((1-\frac{3}{a^2})\mathrm{sinc}a+\frac{3}{a^2}\cos a)}{a^2}\right), \qquad (4.64)$$

where $a = 2\pi\tilde{\nu}L$ (Norton and Beer 1976). This function reduced the resolution of the data from 1.2 GHz to 1.8 GHz.

During the original analysis the modified Blackman-Harris function (Eq. 4.17) had not been developed yet and the Norton-Beer functions were the standard apodizing functions used in Fourier transform spectroscopy. The function was not changed during the re-analysis because the Mars data were only available as spectra; the interferograms could not be located.

2. The subtraction stage involved subtracting the two ports (Eq. 4.62) rather than subtracting background scans from source scans; this removed the offset terms O_1, O_2 from Eqs. 4.60 and 4.61.

3. A statistical filter to remove poor-quality spectra was not applied to this data set.

At the averaging step (step 5), all the data for Neptune and Uranus were combined to produce the averages shown in Fig. 4.30. Initial inspection of the raw Mars data showed that some scans exhibited inconsistent intensities and 2 of the subtractions were removed to avoid contamination of the final average. The averaged Mars spectra are shown in Fig. 4.31.

The ratios of Neptune to Mars ($Ratio_{N:M}$) and Uranus to Mars ($Ratio_{U:M}$) were then computed as in §4.1.5. Fig. 4.32 shows the ratios that result from the analysis. The error in the ratio was determined by the propagation of the standard deviation in the averaged data (as in §4.1.5).

4.2.5 Flux calibration

The intensity spectra of Neptune and Uranus were computed as in Eq. 4.45 and then converted to brightness temperatures using the Planck function (Fig. 4.33). The

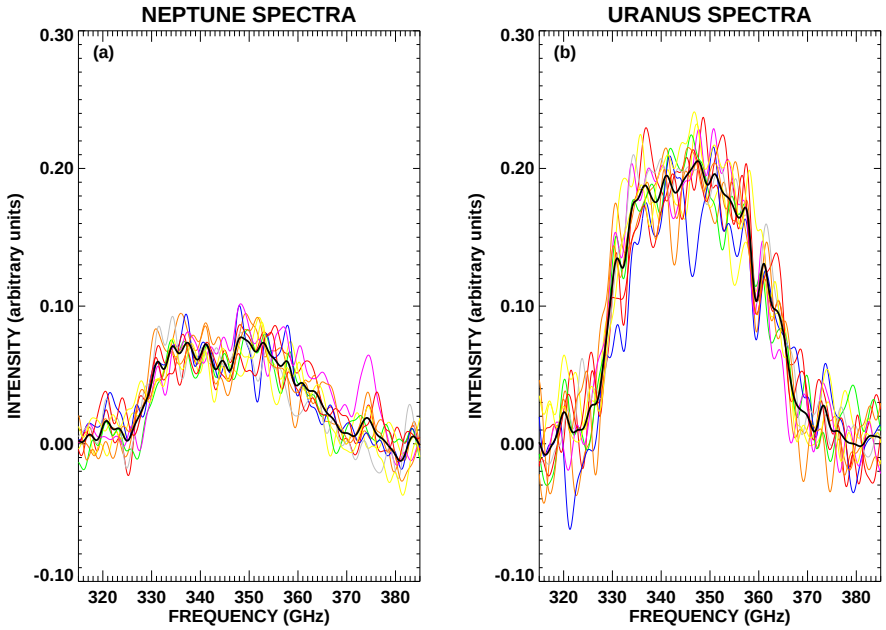

Figure 4.30: *The Neptune (a) and Uranus (b) spectra corrected to a mean airmass and pwv (coloured curves). The averaged spectrum of Neptune and Uranus are shown in black.*

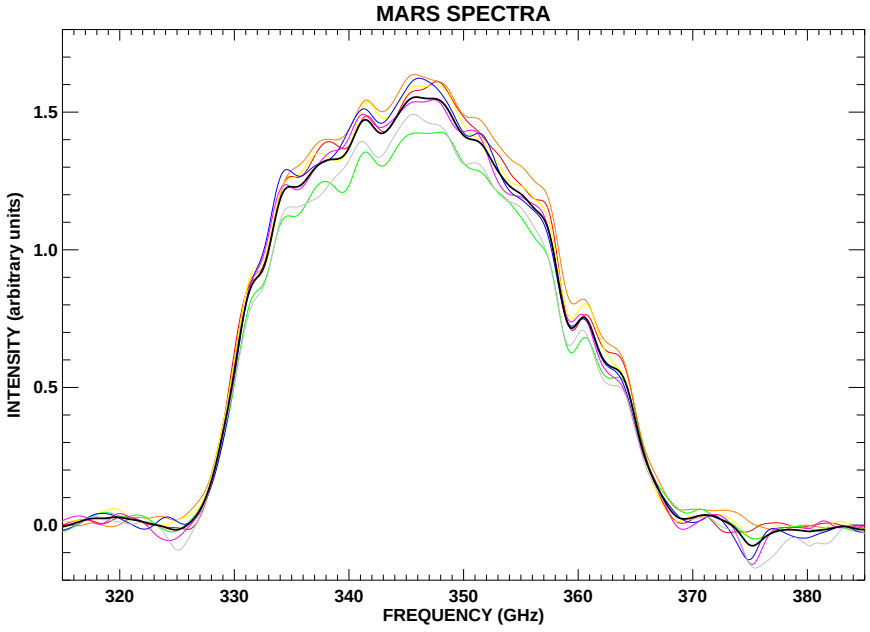

Figure 4.31: *The Mars spectra corrected to a mean airmass and pwv (coloured curves). The averaged spectrum of Mars is shown in black.*

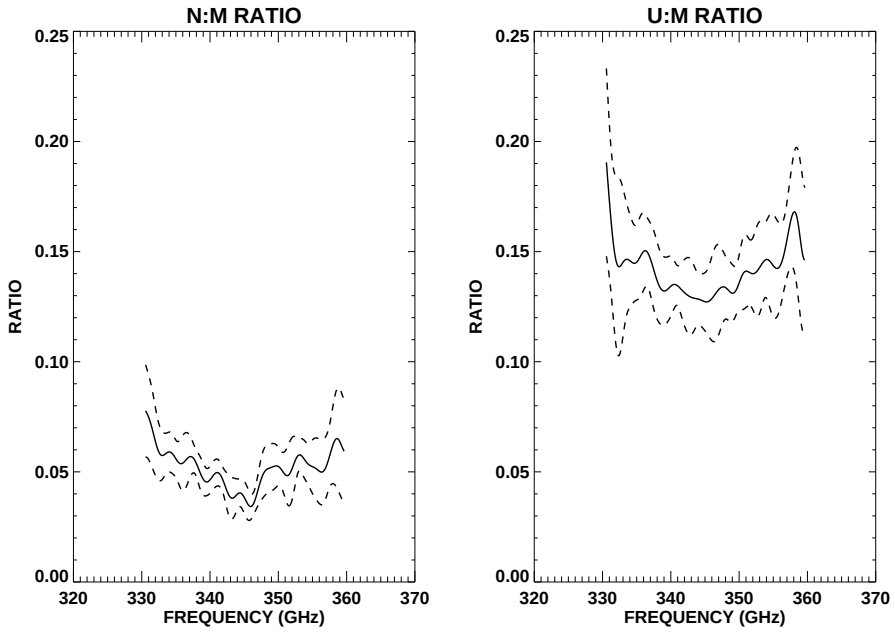

Figure 4.32: *(a) The ratio of N:M (solid) along with the error on the derived result (dashed); (b) The ratio of U:M (solid) along with the error on the derived result (dashed).*

error computed at the average stage was propagated using Eqs. 4.44, 4.46, and 4.48.

4.2.6 Results

The error in the 1993 results is significantly less than in the 2002 data. The lower error can be attributed to the instantaneous removal of atmospheric emission producing less scatter in the spectra at the average step. The remaining error in the results (Neptune and Uranus) and the sinusoidal modulation (channel fringing) in the data still make computing a best-fit model extremely difficult. A range of models was therefore produced for comparison against the data. The model was convolved to the resolution of the data set with the Norton-Beer medium ILS (Eq. 4.64). Figs. 4.34 and 4.35 show models of various CO abundances overlaid on the Neptune and Uranus data.

Comparison of the Neptune data against the models indicate that the CO abun-

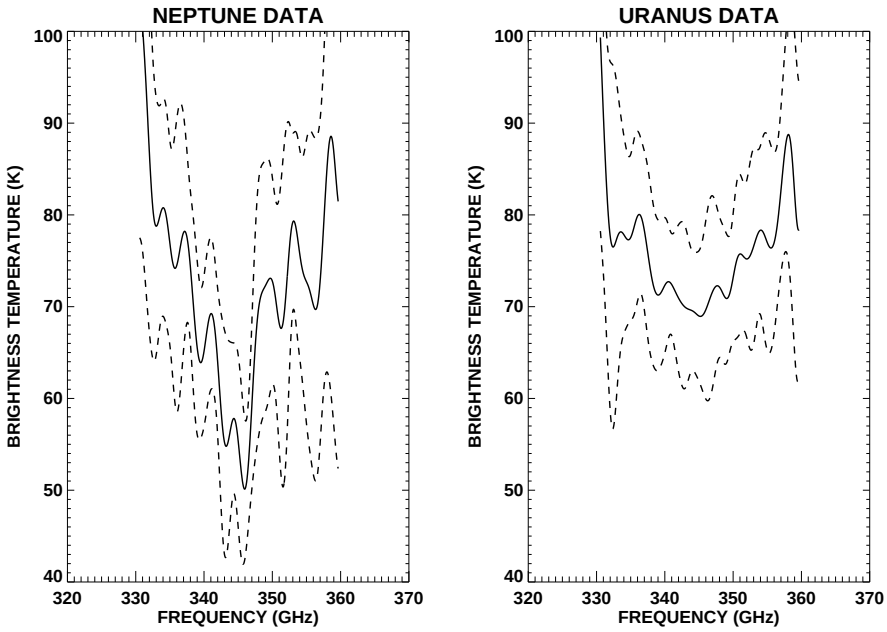

Figure 4.33: *(a) The brightness temperature spectrum of Neptune (solid) with the error in the result (dashed); (b) The brightness temperature spectrum of Uranus (solid) with the error in the result (dashed).*

dance must be higher than 0.8x10^{-6} (orange curve, Fig. 4.34) and lower than approximately 2x10^{-5} (lower brown curve). A tentative detection of CO in Uranus is shown in Fig. 4.35. Comparison of the Uranus data against the models indicate that the CO abundance is higher than approximately 1x10^{-7} (orange curve, Fig. 4.35) and lower than 4x10^{-6} (blue curve).

The uniform CO abundance models in Fig. 4.35 show very poor agreement with the measured lineshape of the Uranus data. Non-uniform CO abundance profiles were therefore used in model calculations to determine if the model fit could be improved. Fig. 4.36 shows the 1993 Uranus spectrum (solid curve) with a model (dash-dot curve) produced using the CO profile shown in Fig. 4.37. This abundance profile was determined by calculating a least-squares fit of the model to the data for which the upper atmosphere CO abundance was set to zero and the lower atmosphere CO abundance along with the pressure levels of transition were allowed to vary. The dash-dot curve of Fig. 4.36 produces an overall better fit to the data than the curves

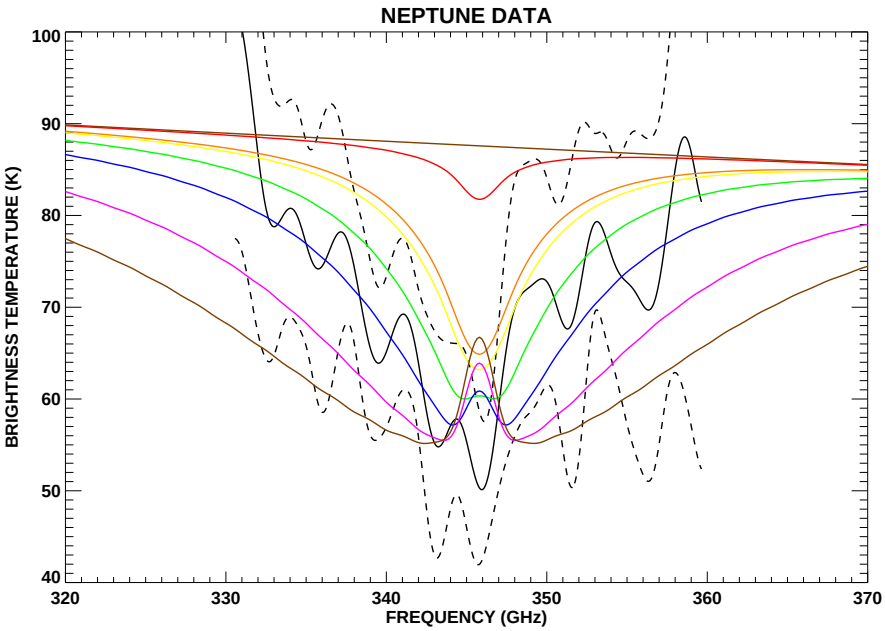

Figure 4.34: *The resultant Neptune brightness temperature spectrum with Norton-Beer medium apodization (black). The error in the brightness temperature is shown with the dashed curves. Eight uniform CO abundance models are overlaid:* 0 *(upper brown),* $1\text{x}10^{-7}$ *(red),* $8\text{x}10^{-7}$ *(orange),* $1\text{x}10^{-6}$ *(yellow),* $2\text{x}10^{-6}$ *(green),* $4\text{x}10^{-6}$ *(blue),* $1\text{x}10^{-5}$ *(violet), and* $2\text{x}10^{-5}$ *(lower brown).*

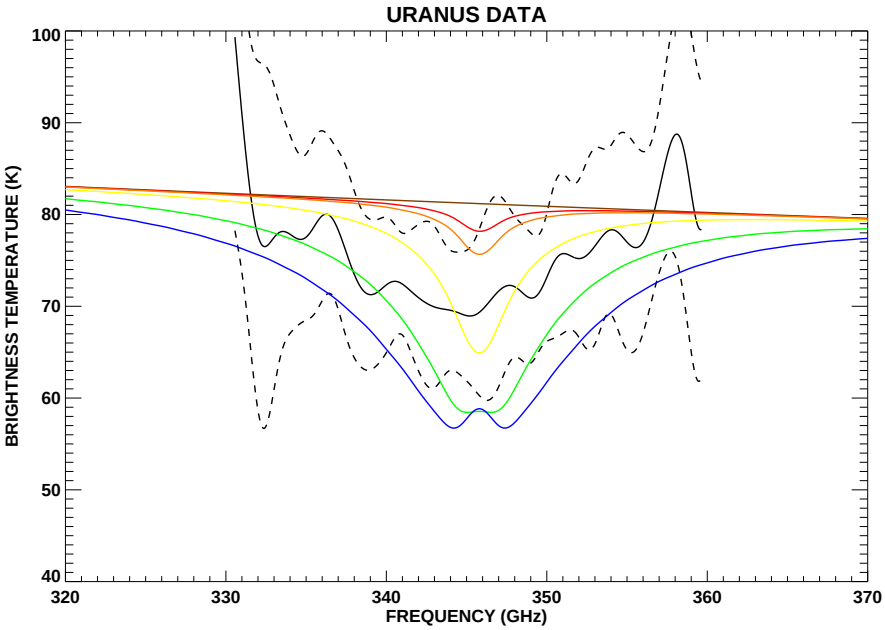

Figure 4.35: *The resultant Uranus brightness temperature spectrum with Norton-Beer medium apodization (black). The error in the brightness temperature is shown with the dashed curves. Six uniform CO abundance models are overlaid:* 0 *(brown),* $5\text{x}10^{-8}$ *(red),* $1\text{x}10^{-7}$ *(orange),* $5\text{x}10^{-7}$ *(yellow),* $2\text{x}10^{-6}$ *(green), and* $4\text{x}10^{-6}$ *(blue).*

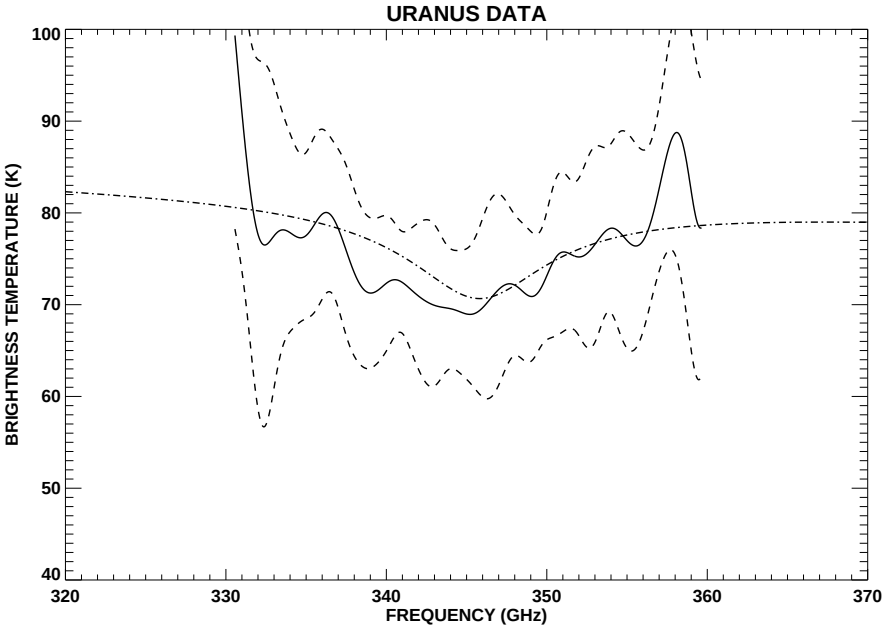

Figure 4.36: *The Uranus brightness temperature spectrum (black). A model calculated using a CO abundance of* $1.5\text{x}10^{-6}$ *confined to the lower troposphere (see Fig. 4.37) is shown with the dash-dot curve.*

shown in Fig. 4.35. To establish the uncertainty in this result a range of models were calculated using the profile in Fig. 4.37 with a variable lower atmosphere CO abundance. Fig. 4.38 shows that the lower atmosphere Uranus CO abundance is between $5\text{x}10^{-7}$ (orange curve) and $1\text{x}10^{-5}$ (blue curve).

A signal-to-noise analysis, using the procedure described in §4.1.8, was performed on this data set. The observed SNR values for Neptune, Uranus, and Mars are given in Table 4.6 along with the 2002 measured SNR scaled for resolution, integration time, source size, and brightness temperature where necessary.

The 1993 observed SNR values for Neptune and Uranus are respectively ~ 8 and 11 times larger than the scaled 2002 results (Table 4.6). This is due to the instantaneous removal of atmospheric emission in the dual-port configuration. A clear detection of the CO line in Neptune is a result of the smaller uncertainty in the data. A tentative detection of CO in Uranus is due to the significant uncertainty in the data. Smaller uncertainties would have been achieved for the Neptune and

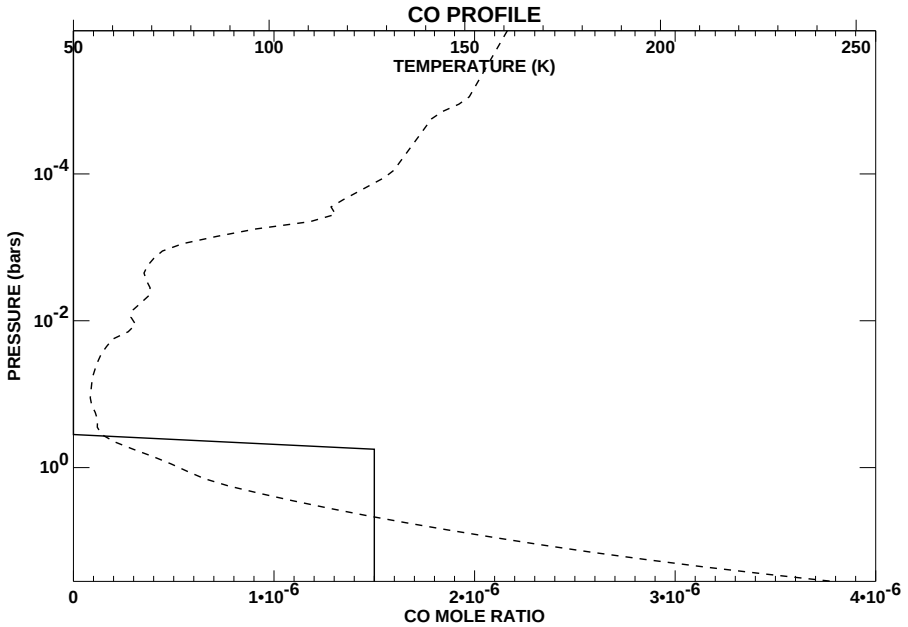

Figure 4.37: *The CO profile (solid curve) corresponding to the dash-dot curve in Fig. 4.36. The temperature profile of Uranus is shown with the dashed curve.*

Table 4.6: *The measured SNR values the parameters of the Neptune, Uranus, and Mars observations.*

Source	Measured SNR	T_S K	t_S hrs	d_S $''$	d_b $''$	$\Delta\nu_S$ GHz	Scaled 2002 SNR
Neptune	4.1	80	1.0	2.300	14	0.04	0.5
Uranus	6.6	81	0.4	3.690	14	0.04	0.6
Mars	17.9	195	0.4	5.920	14	0.04	12.7

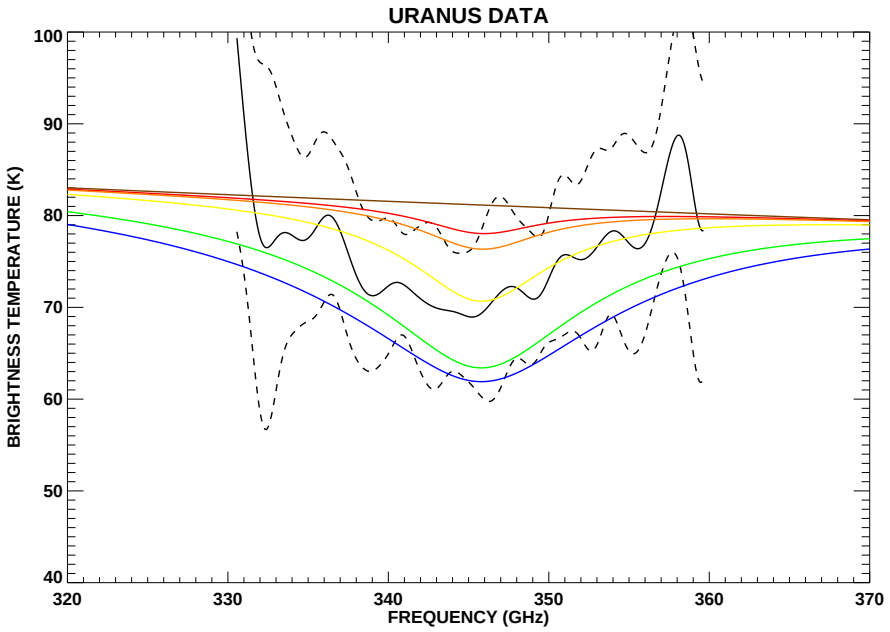

Figure 4.38: *The Uranus brightness temperature spectrum (black). The error in the brightness temperature is shown with the dashed curves. Six models using the profile of Fig. 4.37 are overlaid:* 0 *(brown),* $3\text{x}10^{-7}$ *(red),* $5\text{x}10^{-7}$ *(orange),* $1.5\text{x}10^{-6}$ *(yellow),* $6\text{x}10^{-6}$ *(green), and* $1\text{x}10^{-5}$ *(blue).*

Uranus spectra if Mars had been measured to a higher SNR. The 1993 SNR of Mars is only 1.4 times larger than the scaled 2002 SNR which may indicate that there was an additional source of noise in the Mars data. In these observations, 5 high-resolution scans were performed before the source was switched to the other port. The noise may be due to poor monitoring of the offsets in each port and these observations may have benefited from shorter time scales between nodding. The noise may also be due to imperfect cancellation of atmospheric emission because of the 65″ separation of the ports on the sky.

4.3 Summary

The results produced here show conclusive evidence of CO in Neptune and a tentative detection of CO in Uranus. While the 2002 data show significant uncertainty it is interesting to compare the 2002 and the re-analyzed 1993 data. Figs. 4.39 and 4.40 show excellent agreement between the two data sets considering that the observations were separated by ten years, applied different observing strategies, and used different instruments and detectors.

Extremely low SNR values were achieved in the Neptune and Uranus 2002 observations even though almost 3 hours were spent observing each source (Table 4.4). Increasing the integration time on source would not have necessarily lead to higher SNR values because the Earth's atmospheric emission was removed during the analysis. Sky emission variations in short time intervals preclude this method of observation from producing meaningful results. A dual port system which allows for instantaneous removal of the Earth's atmospheric emission is therefore absolutely required to measure the absorption lines in Neptune and Uranus.

The 1993 spectra produce better results over the 2002 data because of the instantaneous removal of sky emission. The uncertainties are still significant in the 1993 spectra, indicating that longer integration times on Neptune, Uranus, and Mars were required. In addition, shorter time scales between nodding would have monitored the offset terms in each port to greater accuracy and allowed these terms to be more

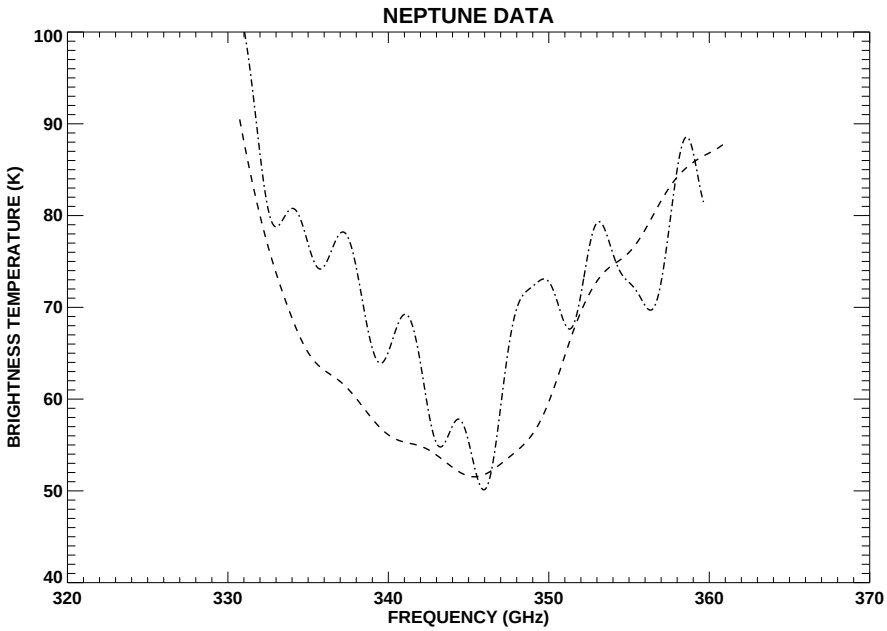

Figure 4.39: *The resultant 1993 Neptune brightness temperature spectrum (dash-dot) and the 2002 spectrum without apodization (dashed).*

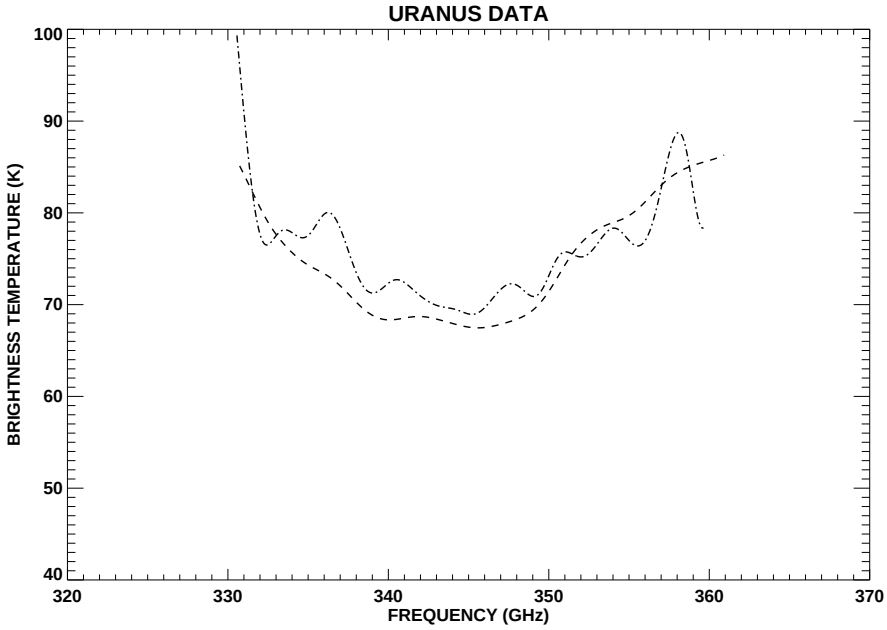

Figure 4.40: *The resultant 1993 Uranus brightness temperature spectrum (dash-dot) and the 2002 spectrum without apodization (dashed).*

accurately removed from the source data.

The lower uncertainties in the 1993 spectra produce the best CO abundance results for Neptune and Uranus. For Neptune, a uniform CO abundance between $0.8\text{x}10^{-6}$ and $2\text{x}10^{-5}$ is indicated, while a profile with CO constrained to the lower atmosphere with an abundance between $5\text{x}10^{-7}$ and $1\text{x}10^{-5}$ is indicated for Uranus.

Chapter 5

Photometric Observations of Neptune

Photometric observations of Neptune were conducted using the Submillimetre Common User Bolometer Array (SCUBA), a facility instrument at the JCMT. Photometric observations measure the integrated flux of a source within a filter bandpass. Photometry is an important technique in submillimetre astronomy because the brightness of faint sources, whose continua vary smoothly with frequency, can be measured to better signal-to-noise than would be possible with a spectrometer.

Photometry was attempted on Neptune to determine if the reduction in integrated flux due to a broad CO absorption line could be detected using SCUBA. Fig. 5.1 is a comparison of the SCUBA 850μm filter profile and the Neptune model with CO mole ratios of zero (dashed) and 1x10^{-6} (solid). This figure shows that the SCUBA 850μm profile is well matched to the width of the CO feature at this wavelength. Photometric calculations using the Neptune model with a mole ratio of 1x10^{-6} in comparison to the Neptune model with no CO show a $\sim$10% reduction in the flux received.

Griffin and Orton (1993) performed precision photometry on Uranus and Neptune in order to fully characterize these planets as submillimetre calibration sources. Their measured fluxes were consistent with models which did not include any effects of CO absorption. The detection of tropospheric CO by Naylor *et al.* (1994), however, contradicted this result. One motivation for repeating the photometric observations of Neptune was to resolve this discrepancy. Whereas the Griffin and Orton measurements were made using UKT14, a single-pixel facility photometer at the JCMT which was retired in 1997, the observations reported in this chapter were made with SCUBA, the JCMT's facility photometric imaging system. This chapter

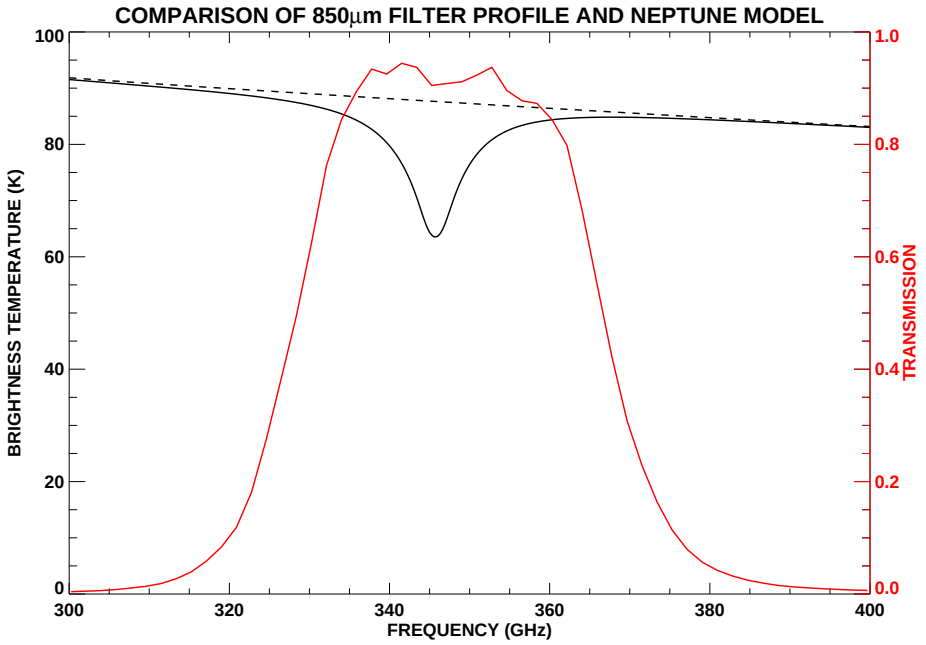

Figure 5.1: *The Neptune model for uniform CO abundances of 0 (black, dashed) and* $1\text{x}10^{-6}$ *(black, solid) at a resolution of 1.8 GHz. The transmission of the 850μm SCUBA filter (red).*

starts with a brief overview of the SCUBA system, including a discussion of the calibration of SCUBA data; observations, data analysis, and results follow. Calibration of the Neptune and Uranus data against Mars is briefly discussed and the chapter ends with a summary of the results.

5.1 Submillimetre Common User Bolometer Array

SCUBA is the facility continuum instrument at the JCMT and is mounted on the left Nasmyth platform. SCUBA is a detector system with 2 arrays of bolometers; 91 bolometers (pixels, hereafter) in the short-wavelength (SW) array, and 37 pixels in the long-wavelength (LW) array (Fig. 5.2). The coupling efficiency of the SW array is optimized for use at 450μm while the LW array is optimized for 850μm. Both arrays have a field of view on the sky of 2.3′ (Holland *et al.* 1999). Fig. 5.3 is an optical

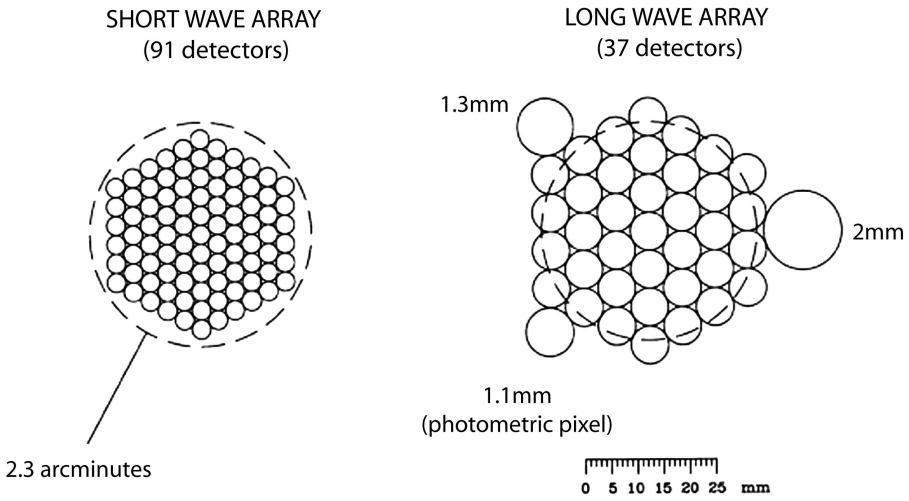

Figure 5.2: *The arrangement of the bolometers in the SW and LW arrays (Holland* et al. *1999).*

schematic of the SCUBA system. The telescope beam reflects from the tertiary mirror, which relays the beam through the telescope bearing, to the left Nasmyth platform. The beam is transmitted into the detector dewar using the external optics (mirrors M1, M2, and M3). An external chopper lies outside of the detector dewar which allows the array bolometers to alternately view the beam from the telescope, the emission from an ambient temperature blade covered in Eccosorb[1], and the reflection of the cold internal optics from the back of a polished blade. Eccosorb is a synthetic material of high emissivity used to simulate blackbody emission. These different loads are used to provide diagnostics of the behaviour of the system.

Upon entering the detector dewar, mirrors M4, M5, and M6 fold the telescope beam into the compact volume and direct the radiation to the dichroic beamsplitter which transmits the LW radiation and reflects the SW radiation. This allows the LW and SW arrays to be used simultaneously. The radiation is passed through a filter which defines the bandpass of the observation before it enters either the LW or SW arrays; the bandpass filters are designed to match the transmission windows

[1]Emerson & Cumins Microwave Products, Inc., 28 York Avenue, Randomly, MA 02368, USA.

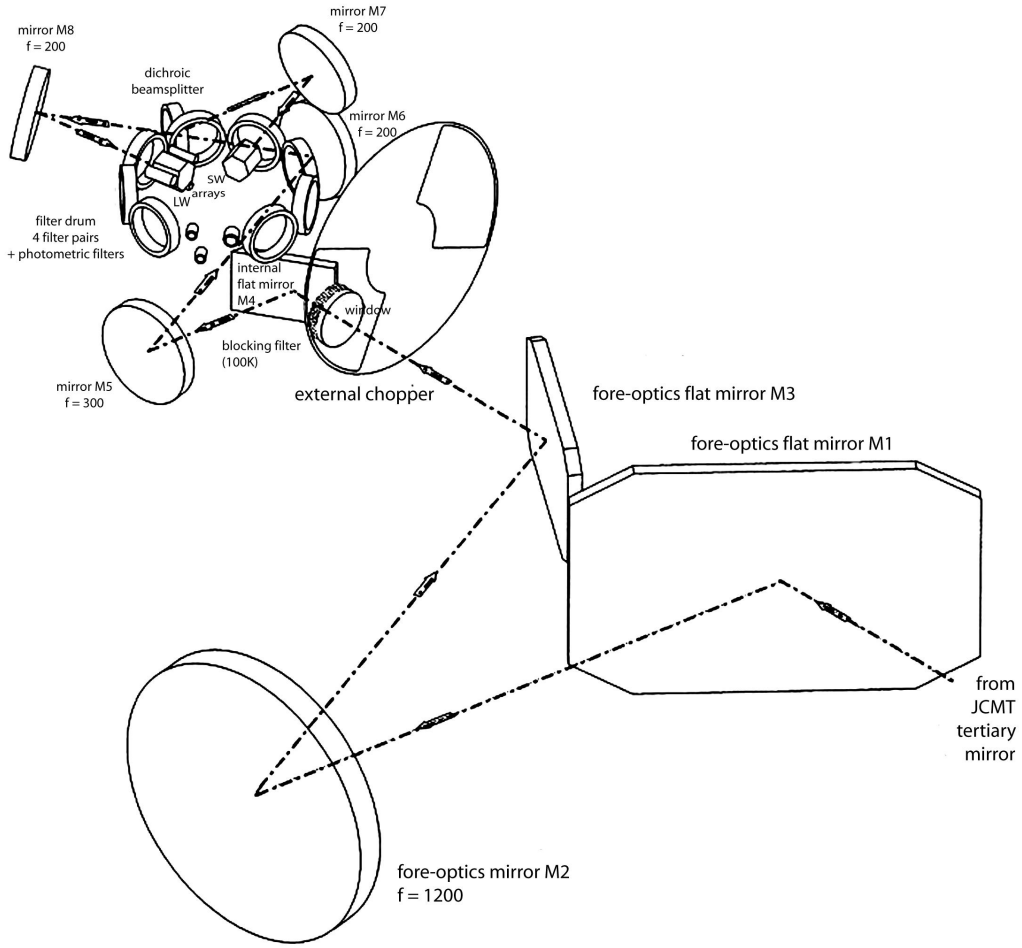

Figure 5.3: *The optical schematic of the SCUBA system (Holland* et al. *1999).*

available from Mauna Kea (Fig. 1.11). Fig. 5.1 shows the transmission profile for the SCUBA 850μm filter. This was the only filter used in this project because the CO line lies near the centre of the atmospheric window. There are spaces for 9 filters in the rotating drum which is maintained at a temperature of approximately 4 K (Holland *et al.* 1999). The mechanism by which the drum rotates has unfortunately not worked for several years; therefore, only the 450 and 850μm filters are accessible.

The bolometers are constructed and function similarly to the FTS bolometer detector (§4.1.1). The arrays are cooled to an operating temperature of 0.1 K using a dilution refrigerator.

5.2 Calibration of SCUBA observations

When a source with intensity $J_s(\nu)$ is viewed by SCUBA the signal received S_{beam1}^{source} is given by,

$$S_{beam1}^{source} = G\left[\int_{\nu_1}^{\nu_2}\left(J_s(\nu)e^{-\tau(\nu)A}\Omega_s\eta_I(\nu) + J_A(\nu)\Omega_b\eta_I(\nu) + J_I(\nu)\Omega_b\right)d\nu + O_1\right], \quad (5.1)$$

where G is the instrument responsivity, ν_1 and ν_2 are the integration limits set by the filter being used, $e^{-\tau(\nu)A}$ is the transmittance of the atmosphere, Ω_s is the solid angle of the source, $\eta_I(\nu)$ is the coupling efficiency of the telescope system, $J_A(\nu)$ and $J_I(\nu)$ are the emission intensities from the atmosphere and telescope system respectively, Ω_b is the solid angle of the beam, and O_1 is an offset term. The telescope system includes the Gore-Tex membrane, telescope, instrument, and detector system.

Several techniques are applied during the observations and analysis to remove components of Eq. 5.1 that mask the source signal $J_s(\nu)$. The secondary mirror is moved by a user-specified distance, called the chop throw, to view the terrestrial atmosphere (sky, hereafter) in order to remove the atmospheric and telescope system emission ($J_A(\nu), J_I(\nu)$). The signal received when the sky is observed S_{beam2}^{sky} is given by,

$$S_{beam2}^{sky} = G\left[\int_{\nu_1}^{\nu_2}\left(J_A(\nu)\Omega_b\eta_I(\nu) + J_I(\nu)\Omega_b\right)d\nu + O_2\right], \quad (5.2)$$

where O_2 is an offset different from O_1 because the secondary has moved causing the

detector beam to fall on slightly different parts of the telescope optics. Subtraction of Eq. 5.2 from Eq. 5.1 gives,

$$\Delta S_{beam1} = S^{source}_{beam1} - S^{sky}_{beam2} = G\left[\int_{\nu_1}^{\nu_2}\left(J_s(\nu)\Omega_s e^{-\tau(\nu)A}\eta_I(\nu)\right)d\nu + O_1 - O_2\right]. \quad (5.3)$$

The atmospheric and telescope system terms will only be removed by this method if they do not change over the time period of the secondary mirror motion. Chopping must be fast because the atmosphere is known to vary in water vapour content on sub-second times scales (Archibald *et al.* 2002). The secondary mirror is therefore chopped at a rate of 7.8 Hz so that the telescope beam moves rapidly between the source and sky.

In order to remove the offset term $O_1 - O_2$ the telescope "nods" during the observations (Fig. 5.4). This involves moving the telescope by an amount equal to the chop throw to bring the source into the reference beam (beam 2). The observations continue in this mode with the secondary mirror chopping to give the following signal,

$$\Delta S_{beam2} = S^{sky}_{beam1} - S^{source}_{beam2} = -G\left[\int_{\nu_1}^{\nu_2}\left(J_s(\nu)\Omega_s e^{-\tau(\nu)A}\eta_I(\nu)\right)d\nu + O_1 - O_2\right]. \quad (5.4)$$

During analysis the signals from the two modes (Eqs. 5.3 and 5.4) are subtracted to remove the offset terms,

$$\Delta S_{source} = \Delta S_{beam1} - \Delta S_{beam2} = 2G\int_{\nu_1}^{\nu_2} J_s(\nu)\Omega_s e^{-\tau(\nu)A}\eta_I(\nu)d\nu. \quad (5.5)$$

It is convenient to split the telescope coupling efficiency $\eta_I(\nu)$ into a frequency-independent component η_I and a frequency-dependent component $\eta_f(\nu)$,

$$\eta_I(\nu) = \eta_I\eta_f(\nu), \quad (5.6)$$

where $\eta_f(\nu)$ is the transmittance of the selected filter. Applying Eq. 5.6 to Eq. 5.5 and re-arranging gives,

$$\Delta S_{source} = 2G\eta_I\int_{\nu_1}^{\nu_2} J_s(\nu)\Omega_s e^{-\tau(\nu)A}\eta_f(\nu)d\nu, \quad (5.7)$$

which is the signal received by SCUBA. A calibration source must be observed to determine the flux conversion factor. The main calibration sources for SCUBA are

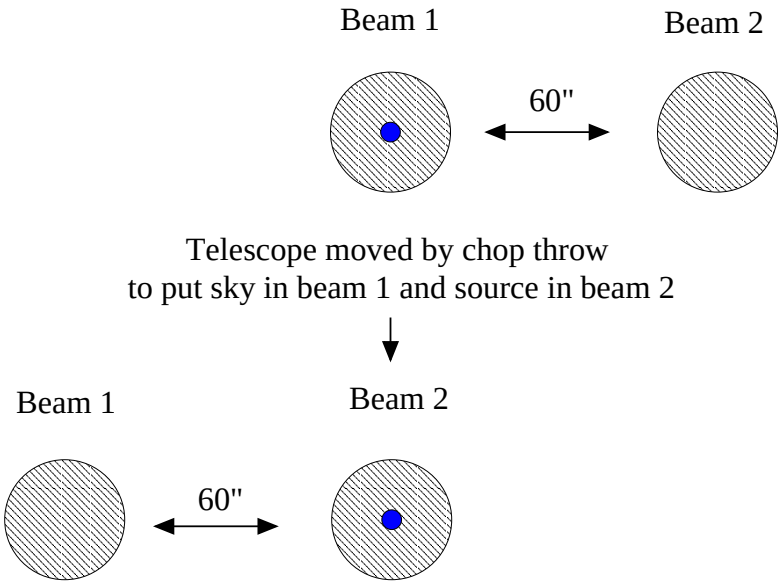

Figure 5.4: *A schematic of the telescope nodding procedure. The blue circle represents Neptune.*

Mars, Uranus, and Neptune. A ratio of the source data against the calibration data gives,

$$\frac{\Delta S_{source}}{\Delta S_c} = \frac{\int_{\nu_1}^{\nu_2} J_s(\nu)\Omega_s e^{-\tau_s(\nu)A_s}\eta_f(\nu)d\nu}{\int_{\nu_1}^{\nu_2} J_c(\nu)\Omega_c e^{-\tau_c(\nu)A_c}\eta_f(\nu)d\nu}, \tag{5.8}$$

where $J_s(\nu)\Omega_s$ and $J_c(\nu)\Omega_c$ are the flux densities of the source and calibrator respectively; and, $\tau_s(\nu)$, $\tau_c(\nu)$, A_s, and A_c are the zenith sky opacities and airmass values for the source and calibrator observations. This measured ratio was compared to model ratios to determine if CO absorption is present in Neptune.

5.3 Observations

The SCUBA observations of Neptune were performed on September 29, 2002 during the same observing run as the 2002 FTS observations (§4.1.3). Uranus was selected as the calibration source, as in Chapter 4, because it met the calibrator criteria (§2.5) and had similar rise and set times as Neptune.

SCUBA was used in photometry mode to measure the flux of Neptune in the 850μm bandpass (LW array). This mode used the central pixel of the LW array to

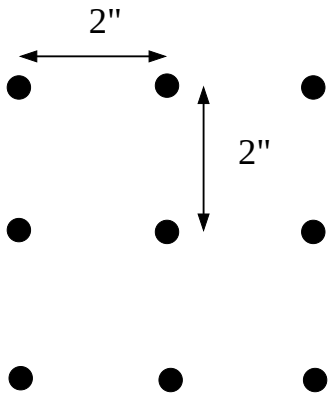

Figure 5.5: *The observation pattern observed by SCUBA. A sample is taken at each position on the grid. The grid is covered by moving the secondary by 2″ spacing.*

observe the source. The standard method of observation for point-source photometry was used, which involved moving the secondary mirror, during the integrations, to observe a small 3x3 grid with a 2″ spacing around the source (Fig. 5.5). This observation method was necessary because the source will not always be precisely centred on the array; applying the jiggle pattern and fitting a paraboloid to the data accounts for this situation.

The secondary mirror was moved by a chop throw of 60″ at a rate of 7.8 Hz to allow sequential viewing of the source and sky. The observations proceeded by observing one cycle of the 3x3 grid (9 positions) after which the telescope nodded and the observations were repeated. A total integration time of ∼30 s was required for each one of these cycles.

The observations of Uranus and Neptune produced a total of 16 and 64 integrations in ∼7 and ∼29 minutes respectively. These integration times were chosen so as to guarantee a SNR greater than 200.

The pwv was monitored during the SCUBA observations allowing the Earth's atmospheric transmittance to be accounted for during the analysis. Fig. 5.6 shows the pwv during the Uranus and Neptune observations as measured by three instruments:

(a) the WVM;

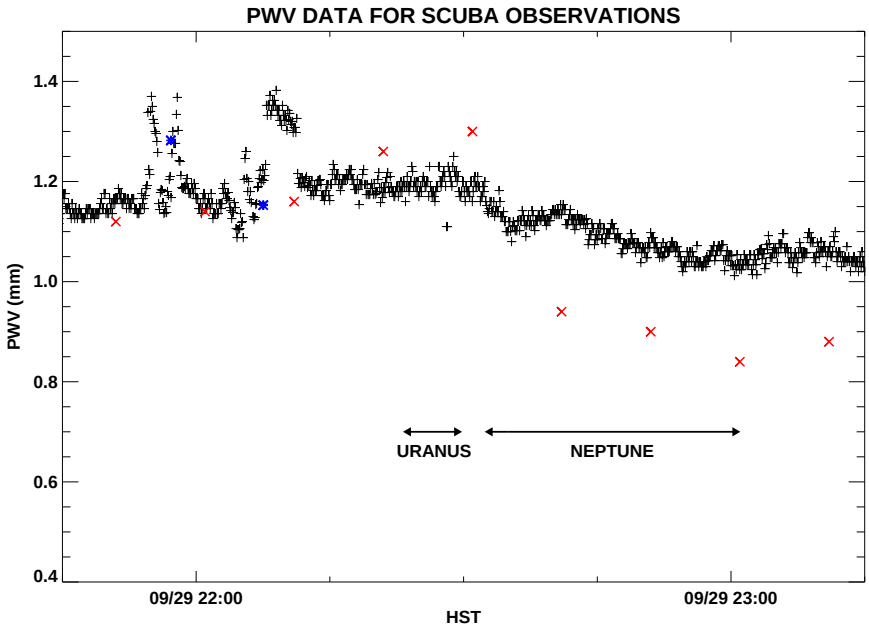

Figure 5.6: *The pwv during the SCUBA observations of Neptune and Uranus. The pwv was measured using three instruments: (a) using the WVM (+), (b) using the CSO radiometer (×) and, (c) using skydips performed by the telescope (∗).*

(b) the CSO radiometer; and,

(c) skydips performed by the telescope.

Skydips are regularly performed during SCUBA observations to measure the atmospheric transmittance. During a skydip the sky brightness temperature is measured using SCUBA as a function of elevation. Knowledge of the telescope's transmission properties allow these data to be fit and a zenith sky opacity derived (Archibald *et al.* 2002).

5.4 Data analysis

The Neptune and Uranus photometric observations were reduced using the SCUBA User Reduction Facility (SURF) suite of software (Jenness and Lightfoot 2000). Several measurements were included in the data set:

Table 5.1: *The mean signal for Neptune and Uranus.*

Source	Number of Integrations	Mean (arb. units)	Standard Deviation
Neptune	64	0.079	0.001
Uranus	16	0.2227	0.0007

1. Noise measurements. The external chopper was activated allowing the arrays to look at a cold load so that noise measurements were performed. Especially noisy pixels were identified and noted for the data analysis.

2. Skydip data. The skydip data were reduced and used, in conjunction with the WVM and CSO data, to extract the sky opacity during each of the observations. These data were used in the extinction correction process (see §5.4.1).

3. Source and calibrator data. These data were reduced using the standard data reduction method for photometry. The first step in this reduction algorithm subtracted the sky from the source signal and then subtracted the nodded data. The data were then flat-fielded to standardize the output from each bolometer. The ring of pixels surrounding the central pixel in the 850μm array were used to determine a mean sky signal; these pixels viewed the terrestrial atmosphere during the observations. The mean sky signal was subtracted from the source signal. In the last step, the 9-point grid was reduced to one value for each integration in the measurement.

Figs. 5.7 and 5.8 show the signal received for each integration in the Neptune and Uranus observations respectively. The Neptune and Uranus integrations were averaged to give a mean and standard deviation (Table 5.1). A Neptune:Uranus ratio of 0.355 ± 0.005 was found using these values.

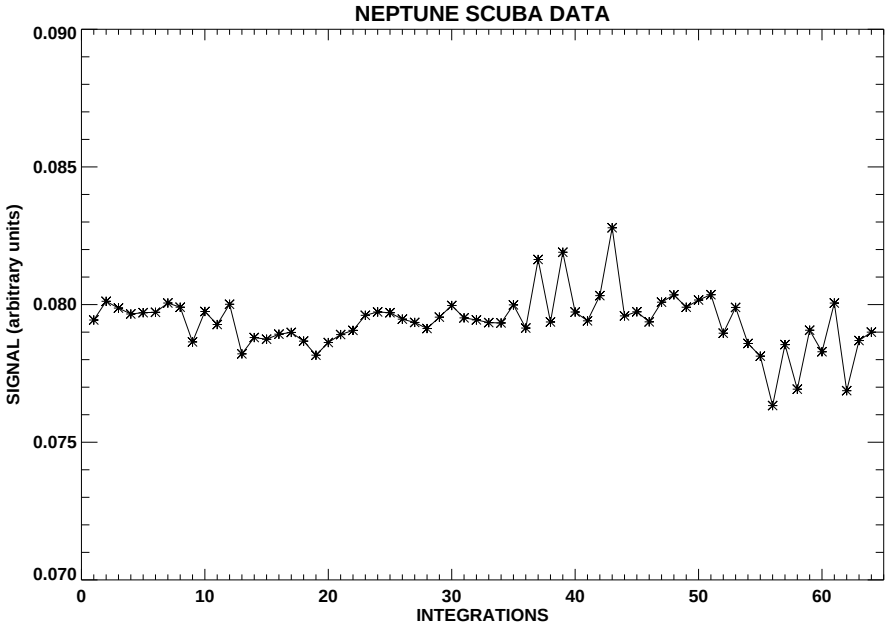

Figure 5.7: *The peak signal for Neptune during each integration.*

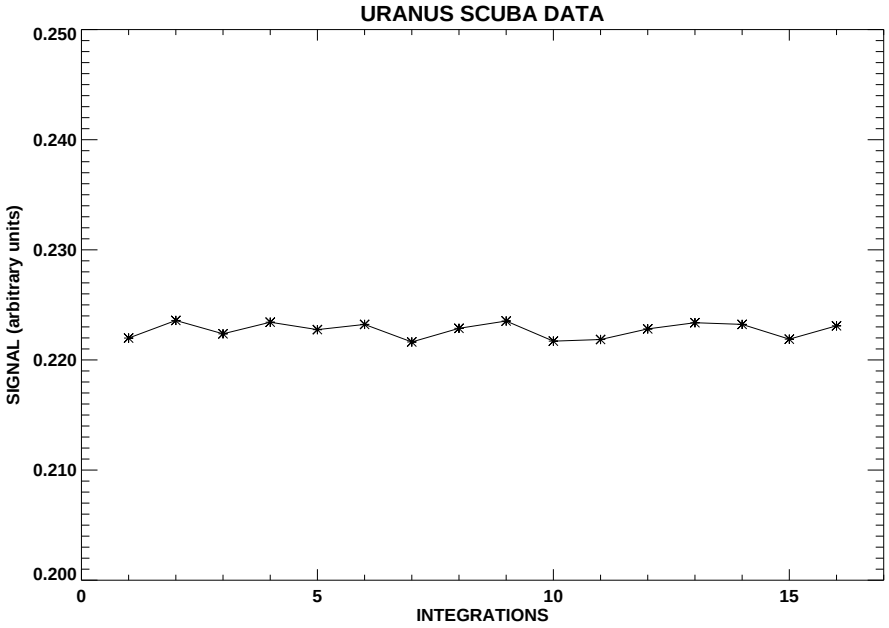

Figure 5.8: *The peak signal for Uranus during each integration.*

Table 5.2: *The airmass, pwv, and angular diameters for the Neptune and Uranus observations.*

Source	Airmass	pwv (mm)	Ang. Dia. $''$
Neptune	1.590	1.09	2.311
Uranus	1.231	1.19	3.662

5.4.1 Adaptation of the radiative transfer model

The Neptune and Uranus models (Chapter 2) were adapted to compute the flux in the 850μm band. To model the signal received by SCUBA, Eq. 5.8 was calculated in which the source (Neptune) and calibrator (Uranus) emission $J_s(\nu), J_c(\nu)$ were given by the model intensities $I_s(\nu), I_c(\nu)$ (Eq. 2.61). The black curve of Fig. 5.9 shows the model Neptune flux density ($J_N(\nu)\Omega_N$). The extinction term $e^{-\tau(\nu)A}$, of Eq. 5.8, was calculated by determining the average airmass and pwv during the observations. The average pwv was calculated using the WVM measurements during each observation period. This was justified due to the strong correlation, at the beginning of the night, between the skydip and WVM data (Fig. 5.6). Table 5.2 lists the values used in the model calculations. These values were used along with the ULTRAM model (§4.1.4; Chapman (2000)) to calculate the zenith sky opacity and the extinction. The blue curve of Fig. 5.9 shows an example of the transmittance of the Earth's atmosphere for $pwv = 1$ mm and $A = 1.3$. The term $\eta_f(\nu)$ was given by the transmittance of the 850μm filter (red curve, Fig. 5.9) as measured by the University of Lethbridge FTS (Holland *et al.* 1999). The integration over the product of all three terms produced the model SCUBA signal for the source being observed.

5.4.2 Results

The Neptune and Uranus models were calculated assuming a CO mole ratio of zero. The model and measured ratios are given in Table 5.3. The measured N:U ratio

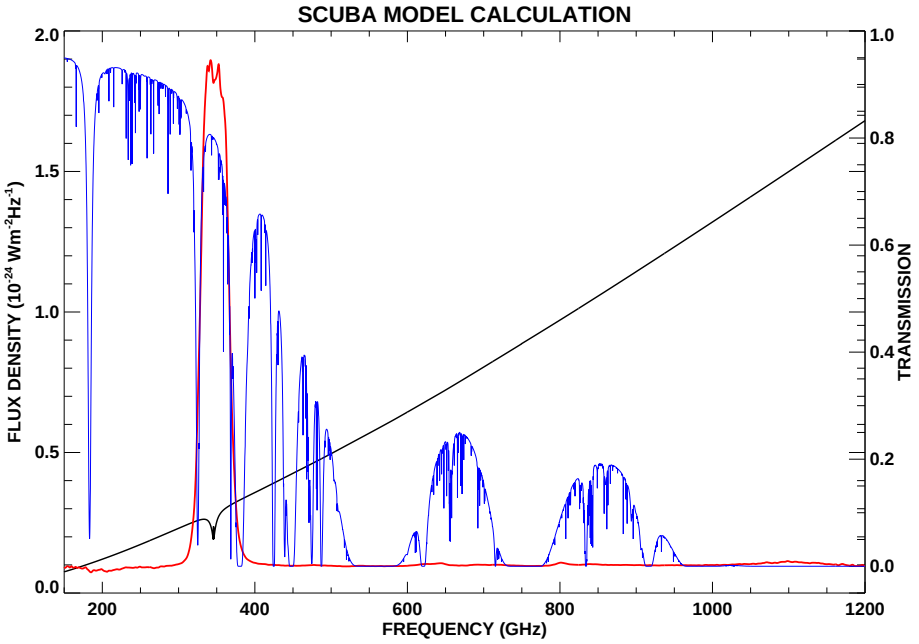

Figure 5.9: *The three terms used in the computation of the SCUBA model: (a) the flux density of Neptune using a CO mole ratio of* $1.0\text{x}10^{-6}$ *and an angular diameter of* $2.311''$ *(black curve); (b) the transmission of the Earth's atmosphere calculated for* $A = 1.3$ *and* $pwv = 1$ *mm (blue curve); (c) the transmission of the* 850μ*m SCUBA filter (red curve).*

Table 5.3: *The measured and model ratios assuming a CO mole ratio of zero.*

Source/Calibrator	Measured Ratio	Modelled Ratio
Neptune/Uranus	0.355 ± 0.005	0.403

when compared to the modelled ratio indicates that the SCUBA data show evidence of CO absorption in Neptune. Fig. 5.10 shows the model Neptune to Uranus ratios calculated for various uniform Neptune CO mole ratios. The measured ratio is shown as a range of values with the upper and lower values defined by the uncertainty in the measurement (dashed curves). Uranus was assumed to have no CO in this calculation. These values indicate that Neptune's CO mole ratio is between $1.2\text{x}10^{-6}$ and $1.7\text{x}10^{-6}$.

5.5 Calibration against Mars

After the discovery of CO in Uranus during the course of this project by Encrenaz *et al.* (2004), the Neptune and Uranus SCUBA data were re-analyzed using Mars as the calibration source. Mars photometry data were taken from the JCMT data archive, since Mars was not observed during the September 2002 observations. The Mars data were taken on February 16, 2002, during which a total of 6 integrations in 3 minutes were performed to guarantee a SNR greater than 200. Fig. 5.11 shows the pwv during the Mars observations.

The Mars data were analyzed using the same method as the Neptune and Uranus SCUBA data (§5.4). The output from this analysis is shown in Fig. 5.12. Integration 3 was removed from the Mars analysis because it showed an erroneously high signal. The 5 data points were averaged to give a mean signal and standard deviation for Mars of 1.280 ± 0.003. The mean Mars signal and the Neptune and Uranus mean

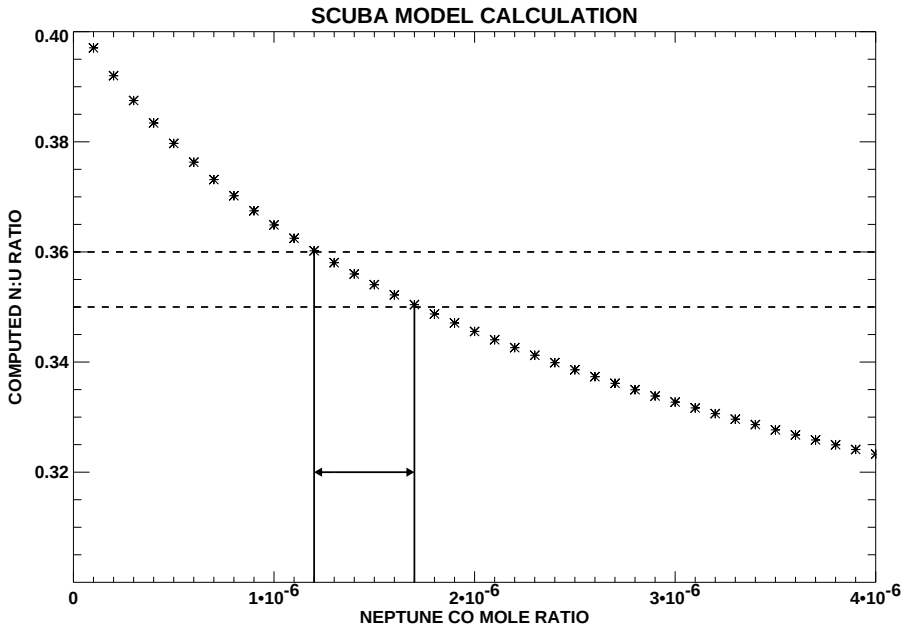

Figure 5.10: *The range of CO mole ratios that produce model Neptune to Uranus ratios in the range of the measured ratio. The calculated ratios are given by the $*$ symbols. The range of the measured ratio is shown with the dashed curves. In this calculation Uranus was assumed to have no CO .*

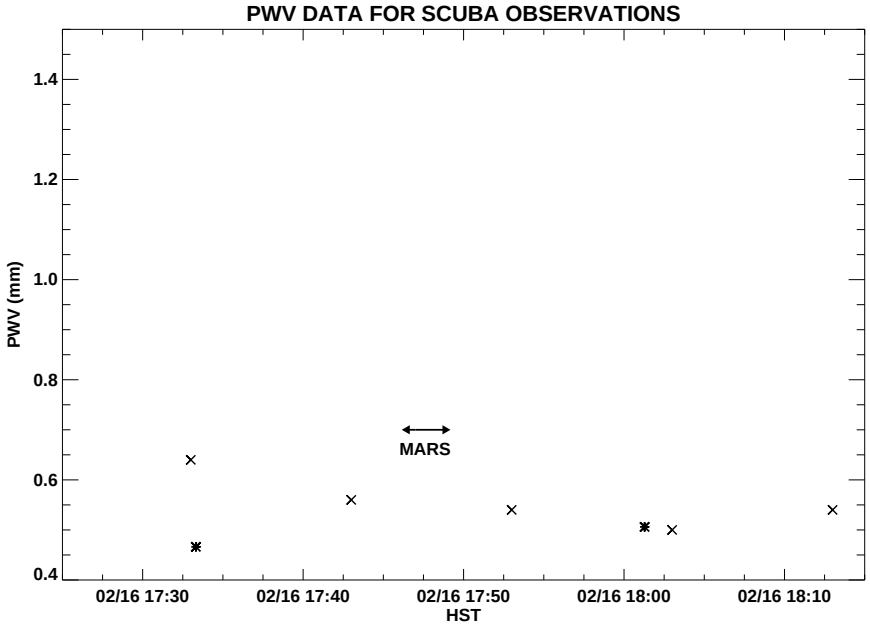

Figure 5.11: *The pwv during the SCUBA observations of Mars. The pwv was measured using two instruments: (a) using the CSO radiometer (×) and, (b) using skydips performed by the telescope (∗).*

signal values given in Table 5.1 were used to compute ratios of,

$$Neptune : Mars = 0.0617 \pm 0.0008, \tag{5.9}$$

$$Uranus : Mars = 0.1740 \pm 0.0007. \tag{5.10}$$

The pwv, airmass, and angular diameter of Mars during the observations were required to compute the Mars SCUBA model. The WVM was unfortunately not functioning during these observations; therefore, the pwv for the mid-point of the Mars observations was calculated using a straight line fit between the skydip measurements taken before and after the Mars observations. A mean airmass of 1.158, pwv of 0.49 mm, and angular diameter of $5.061''$ were used in the Mars model calculations. Assuming CO mole ratios of zero for all three planets, the model Neptune:Mars and Uranus:Mars ratios were calculated for comparison against the measured ratios (Table 5.4).

Fig. 5.13 and 5.14 show the CO mole ratio results for Neptune and Uranus respec-

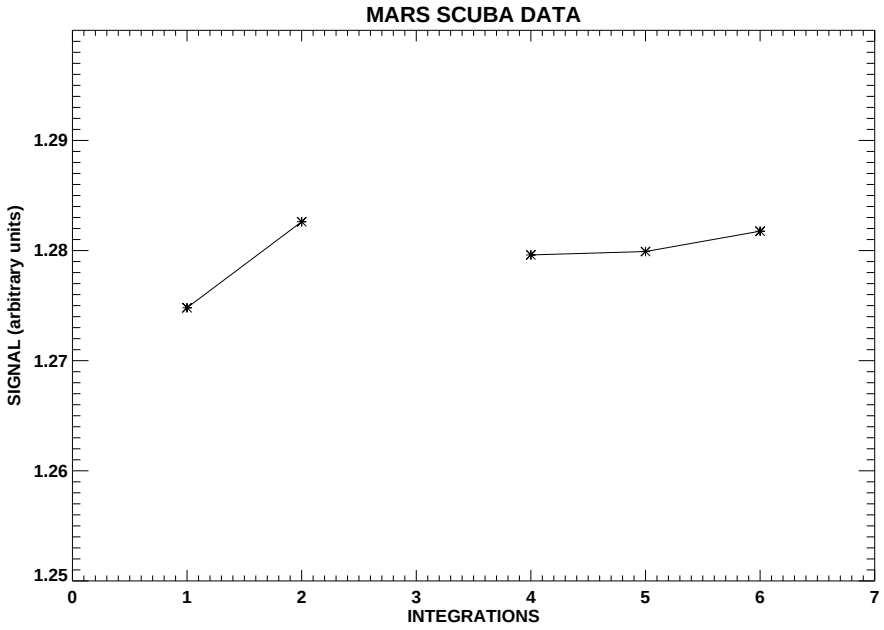

Figure 5.12: *The peak signal for Mars during each integration.*

Table 5.4: *The measured ratios and model ratios assuming a CO mole ratio of zero for all three planets.*

Source/Calibrator	Measured Ratio	Modelled Ratio
Neptune/Mars	0.0617 ± 0.0008	0.064
Uranus/Mars	0.1740 ± 0.0007	0.159

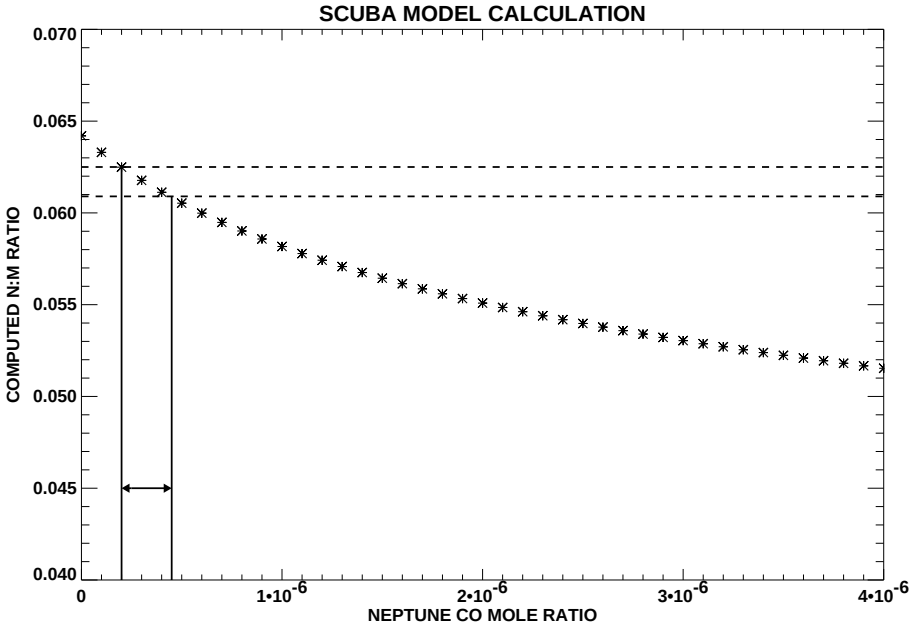

Figure 5.13: *The range of CO mole ratios that produce model Neptune to Mars ratios in the range of the measured ratio. The calculated ratios are given by the ∗ symbols. The range of the measured ratio is shown with the dashed curves.*

tively when the ratio was taken against Mars. For Neptune, calculations indicate a CO mole ratio between $0.2\text{x}10^{-6}$ and $0.45\text{x}10^{-6}$. For Uranus, a CO mole ratio cannot be determined because the measured ratio is higher than the computed zero CO ratio.

Figs. 5.13 and 5.14 indicate that the computed ratios are much too small in comparison to the measured ratios, for both N:M and U:M. The N:M ratio yields CO abundances for Neptune that are unrealistically small, and the U:M ratio does not produce a solution for Uranus. The Mars model was investigated as a potential cause of this discrepancy. Mars exhibits CO absorption but the low-pressure atmosphere produces a very narrow absorption (Fig. 2.16). Calculations taking into account the absorption in Mars produce a SCUBA Mars model that changes by less than 0.1% in comparison to the model without CO. The measured and model ratios can not therefore be brought into agreement with this change alone. The calibration of Neptune and Uranus data against Mars observations taken on different days introduces

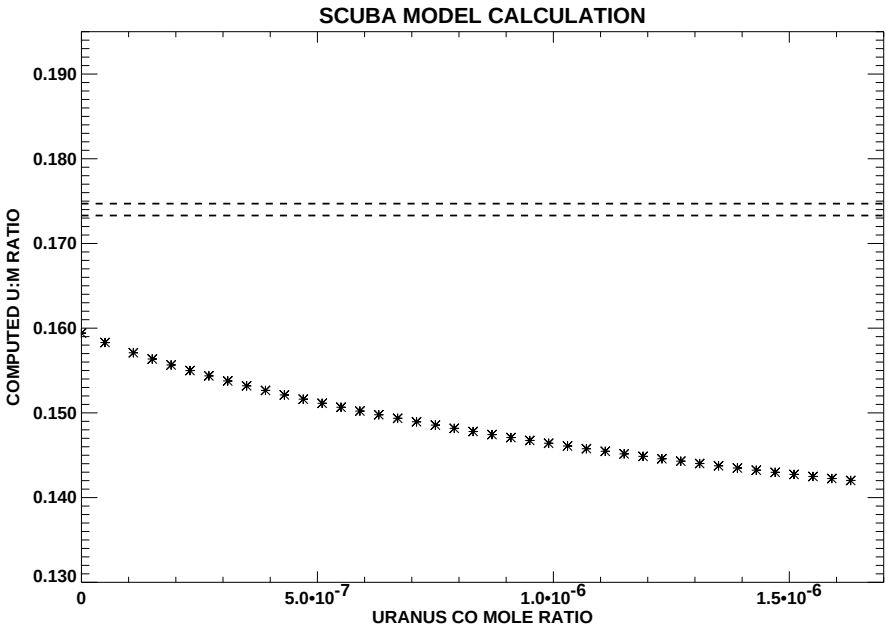

Figure 5.14: *The range of CO mole ratios that produce model Uranus to Mars ratios in the range of the measured ratio. The calculated ratios are given by the $*$ symbols. The range of the measured ratio is shown with the dashed curves.*

an undeterminable error into the measured ratios which this model does not and can not account for. Experience at the JCMT indicates that SCUBA flux repeatability from night to night is rarely better than 5% (Archibald *et al.* 2002) due to a number of factors, including pointing repeatability, focus and dish gain variations, and responsivity variations in the bolometers. This systematic error is significantly higher than the statistical error in the data.

5.6 Summary

The ratios derived using Mars as the calibration source are clearly not trustworthy and therefore can not be used in specifying the CO abundance in Neptune and Uranus. The measured N:U ratio indicates a CO mole ratio in Neptune between $1.2\text{x}10^{-6}$ and $1.7\text{x}10^{-6}$, assuming no CO in Uranus.

Chapter 6

Conclusion

In this thesis project three measurement techniques were used to determine the CO abundance in Neptune. A comparison of the results from these techniques starts this chapter. A discussion of the best result and its implications for the source of CO follows. This chapter ends with recommendations for future work in the field.

6.1 Comparison of results

Three measurement techniques were used to determine the CO abundance profile in Neptune. In Chapter 3, the heterodyne receiver B3 was used to measure the entire CO J=3–2 transition in Neptune, including both the emission and absorption components, at a resolution of 1.25 MHz. Chapter 4 presented the results from two sets of FTS measurements of the CO absorption; the 1993 data were found to be superior and are considered here to the exclusion of the 2002 data. Finally, in Chapter 5 photometric measurements were undertaken using SCUBA to determine the integrated flux in the 850μm band. The results from these three sets of measurements are summarized in Table 6.1.

The heterodyne measurements were superior to the FTS and SCUBA results for two reasons: first, the comprehensive nature of the high-resolution measurement enabled simultaneous determination of the CO abundance throughout the atmosphere; and second, the error bars are smaller indicating a more precise measurement.

The 1993 polarizing FTS spectrum agrees with the RxB3 spectrum to within one standard deviation for a significant part of the frequency range and within two standard deviations for the entire frequency range (Fig. 6.1). As a result of this

Table 6.1: *The CO results for Neptune for the three measurement techniques. All CO values are* x10^{-6}.

Instrument	Lower Atmosphere	Upper Atmosphere
RxB3	0.6–1.0	1.6–2.4
FTS	0.8–20	
SCUBA	1.2–1.7	

agreement, the determined CO mole ratios also agree within the uncertainties. The large uncertainty in the CO mole ratio derived from the FTS spectrum, however, precludes any conclusions being drawn from this result about the source of CO in Neptune's atmosphere.

The SCUBA and RxB3 results do not agree within the given uncertainties. Prompted by this discrepancy, the SCUBA data for Neptune and Uranus were examined in more detail. It will be recalled that in the SCUBA photometry mode (§5.3), the telescope executes a small 3x3 grid centred on the nominal position of the source for each integration, and a parabola is fit to the points so obtained. This method provides an estimate of the flux from the source even in the presence of pointing errors of up to 1.5″, which are common. The parabolic fit also provides, as a by-product, the coordinates of the fitted peak. For the Uranus measurements, the average pointing error was 0.4″, which is well within the 3x3 grid of measured points. For Neptune, however, the pointing error in the 64 integrations ranged from 1.5″ to 5.5″, with a mean value of 3.1″. All of the Neptune data points were therefore outside the range within which the parabolic fit technique is valid, and for most integrations (53) the fitted peaks actually lay outside the 3x3 grid. It is extremely difficult under these circumstances to derive a robust estimate of the flux from the source, and it is therefore not surprising that the SCUBA and RxB3 results do not agree.

The CO abundance profile determined from the B3 measurements is clearly the

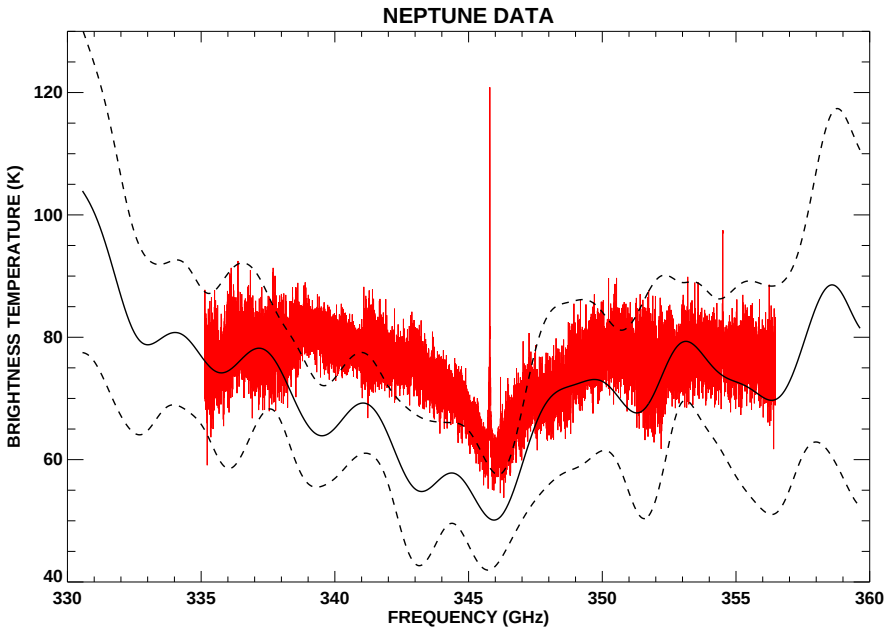

Figure 6.1: *The heterodyne spectrum (red) and the FTS spectrum (black) with uncertainty (dashed curve).*

superior result. This CO abundance profile will therefore be used for the discussion which follows.

6.2 Discussion

Previous determinations of the tropospheric CO abundance by Guilloteau *et al.* (1993), Naylor *et al.* (1994), Courtin *et al.* (1996), and Encrenaz *et al.* (1996) were limited by the precision of their measured spectra. The tropospheric abundance of (0.8 ± 0.2)x10^{-6} determined here agrees with most of these previous measurements within their estimated uncertainties.

The stratospheric CO abundance of $1.9^{+0.5}_{-0.3}$x10^{-6}, however, is significantly higher than others reported in the literature. Using receivers at the JCMT, CSO and IRAM in 1998, Marten *et al.* (2005) measured the emission cores of the J=2–1, 3–2 and 4–3 lines of CO. They assumed a uniform CO abundance of 1.0x10^{-6}, because their spectra did not include any absorption signatures, and determined the corresponding

best-fit temperature profile. In view of more recent results, as discussed in the following paragraph, this assumption is no longer valid.

One strategy to address the conflicting results was to measure a CO transition over a large frequency range at high resolution so that the CO abundance in the stratosphere and troposphere could be determined simultaneously using a single measurement. Concurrently with this thesis project, Lellouch *et al.* (2005) attempted this technique on the J=2–1 line using IRAM. The outcomes are qualitatively similar: Lellouch *et al.* also found a higher CO abundance in the upper stratosphere ($1.0\text{x}10^{-6} \pm 15\%$) than in the troposphere and lower stratosphere ($0.5\text{x}10^{-6} \pm 15\%$). Quantitatively, however, the results do not agree within the quoted uncertainties. It appears that the errors quoted by Lellouch *et al.* were underestimated because their analysis did not include the effects of either the calibration variability in their data or the uncertainty in their temperature profile (Lellouch, private communication). The former effect required these authors to apply post-processing calibration corrections, which carry the potential for corruption of the measured line shape. This corruption is evident on the low-frequency side of their spectrum, as the authors recognize, but examination of their raw data indicates that it must also be present on the high-frequency side at some level. By contrast, the spectrum measured in this work required no post-processing. The latter effect led, in the present work, to an uncertainty of $\sim$30% in the troposphere and lower stratosphere, and would have a similar magnitude for Lellouch *et al.*. It is therefore likely that these results would be brought into quantitative agreement if all sources of error in both data sets were considered. Finally, it is important to recognize that quantitative comparison of the CO abundances is intrinsically difficult in any case, since different spectral models were used; the model in this work included the most recent values of the CO line parameters and the H_2, He, and CH_4 abundances.

Despite these differences, the measured CO abundance profiles from this work and from Lellouch *et al.* (2005) indicate the presence of both an internal source, which provides the tropospheric and lower stratospheric CO, and an external source which provides additional CO to the upper atmosphere. The former, whereby CO is

transported by convection from the deep atmosphere to observable levels, requires an oxygen enrichment in the planetary interior of 440 times the solar abundance (Lodders and Fegley 1994). This high O/H enrichment would indicate an interior dominated by water ice.

Rosenqvist *et al.* (1992) considered two external sources for CO. The first mechanism was the photochemical formation of CO from reactions between methane photochemistry by-products and oxygen released from water on the satellites and rings of the planet. There are three chemical pathways from which CO is formed by an external source of O,

$$(a) \quad \mathrm{O} + \mathrm{CH_3} \rightarrow \mathrm{CH_2O} + \mathrm{H},$$
$$\mathrm{CH_2O} + h\nu \rightarrow \mathrm{CO} + \mathrm{H_2}, \tag{6.1}$$
$$(b) \quad \mathrm{O} + \mathrm{C_2H_4} \rightarrow \mathrm{CH_3} + \mathrm{HCO},$$
$$\mathrm{HCO} + \mathrm{H} \rightarrow \mathrm{H_2} + \mathrm{CO}, \tag{6.2}$$
$$(c) \quad \mathrm{O} + \mathrm{C_2H_2} \rightarrow \mathrm{CO} + \mathrm{CH_2}. \tag{6.3}$$

It is unlikely that this mechanism is responsible for the observed CO abundances due to the lack of water sources at Neptune in comparison with Saturn, and Saturn's low stratospheric CO abundance (more than an order of magnitude smaller than Neptune's).

The second mechanism considered by Rosenqvist *et al.* (1992) involves the photochemical formation of CO by reactions between methane photochemistry by-products and OH. This photochemical pathway begins with the formation of OH from the photolysis of water released from meteoritic ablation through the following reaction,

$$\mathrm{H_2O} + h\nu \rightarrow \mathrm{OH} + \mathrm{H}. \tag{6.4}$$

A methane photochemistry by-product ($\mathrm{C_2H_2}$) is used to produce an intermediate molecule, CHCHOH, in the next step,

$$\mathrm{OH} + \mathrm{C_2H_2} \rightarrow \mathrm{CHCHOH}. \tag{6.5}$$

At low pressures CHCHOH decomposes to produce ketene ($\mathrm{CH_2CO}$) which is then

photolyzed to CO,

$$\mathrm{CHCHOH} \rightarrow \mathrm{CH_2CO} + \mathrm{H}, \tag{6.6}$$

$$\mathrm{CH_2CO} + h\nu \rightarrow \mathrm{CH_2} + \mathrm{CO}. \tag{6.7}$$

This mechanism is more likely because meteorites composed primarily of water ice are known to ablate at high elevations producing OH radicals (Moses 1992).

An order-of-magnitude estimate of the planetary H_2O influx corresponding to the observed abundance of stratospheric CO may be determined as follows. In the stratosphere and troposphere eddy diffusion dominates over molecular diffusion. The downward flux of CO (Φ) is therefore given by the eddy diffusion component of Eq. 1.14,

$$\Phi = K\left(\frac{dn_i}{dz} + n_i\left[\frac{1}{H} + \frac{1}{T}\frac{dT}{dz}\right]\right), \tag{6.8}$$

where n_i is the number density of CO, H is the scale height, T is the temperature and K is the eddy diffusion coefficient. If it is assumed that the atmosphere is isothermal ($\frac{dT}{dz} = 0$) and in hydrostatic equilibrium ($p = p_0 e^{-z/H}$) then Eq. 6.8 reduces to,

$$\Phi = Kn\frac{\partial q}{\partial z} \simeq Kn\frac{\Delta q}{\Delta z}, \tag{6.9}$$

where q is the CO mole ratio, n is the atmospheric number density, and $\Delta q/\Delta z$ is the gradient in the CO mole ratio. Eq. 6.9 was applied to the CO transition layer located at approximately 3 mbar, where the CO produced in the upper atmosphere is converted to CH_4. Using values of $K = 8\text{x}10^3$ cm^{2}s^{-1} (Romani A profile; §1.4.2), $n = 2.4\text{x}10^{23}$ molecules m^{-3}, $\Delta q = 1.1\text{x}10^{-6}$ and $\Delta z = 3482$ km, a flux of $6\text{x}10^9$ CO molecules cm^{-2}s^{-1} was determined. A planetary influx of $> 10^9$ H_2O molecules cm^{-2}s^{-1} would therefore be required to match this observed CO abundance.

Feuchtgruber *et al.* (1997) used the first and only observations of neptunian H_2O, as measured by ISO, to estimate the planetary H_2O influx. They found an H_2O influx in the range 10^5 to 10^7 molecules cm^{-2}s^{-1}. This is 10^2 to 10^4 times smaller than the influx calculated above. Two possibilities remain:

1. If stratospheric CO in Neptune is produced by water influx due to meteorites and interplanetary grains, as originally suggested by Rosenqvist *et al.* (1992),

then the steady-state influx of H_2O must be higher than estimated by Feuchtgruber *et al.*. More measurements of neptunian H_2O are necessary to determine if the H_2O influx is in fact higher.

2. If, on the other hand, the steady-state influx of H_2O was correctly estimated by Feuchtgruber *et al.*, then an alternative physical mechanism is required which can deliver CO, but not H_2O, to Neptune's upper atmosphere. Cometary impacts represent an attractive hypothesis, since observations of the Shoemaker-Levy 9 impact revealed that most of the cometary water ice was converted to CO by shock chemistry (Lellouch 1996).

The observations presented here do not, by themselves, allow for discrimination between these two possibilities.

In the case of Uranus, there has been only one other positive detection, by Encrenaz *et al.* (2004), of CO in the planet. Encrenaz *et al.* measured the spectrum of Uranus between 4.6 and 5.0μm using an imaging spectrometer on the Very Large Telescope (VLT) in Chile. The tropospheric continuum was detected and a CO upper limit of $2\text{x}10^{-8}$ for the pressure region between 0.5 and 3.1 bar was determined. The result in this project finds that CO is constrained to the lower troposphere (P $>$ 0.5 bar) with an abundance between $5\text{x}10^{-7}$ and $1\text{x}10^{-5}$. The abundances found in this work are at least one order of magnitude larger than the Encrenaz *et al.* results. More measurements of the Uranus CO profile are required to resolve this discrepancy.

6.3 Recommendations for future work

Plans are already under way to improve the CO abundance profile in Neptune by measuring the J=2–1 and 4–3 CO lines at 230.5 GHz, and 461.0 GHz respectively. The JCMT facility heterodyne receivers A and W (C band) will be used at a resolution of 1.25 MHz to measure both the emission and absorption of each line. Figs. 6.2 and 6.3 show the model J=2–1 and 4–3 CO lines for uniform CO mole

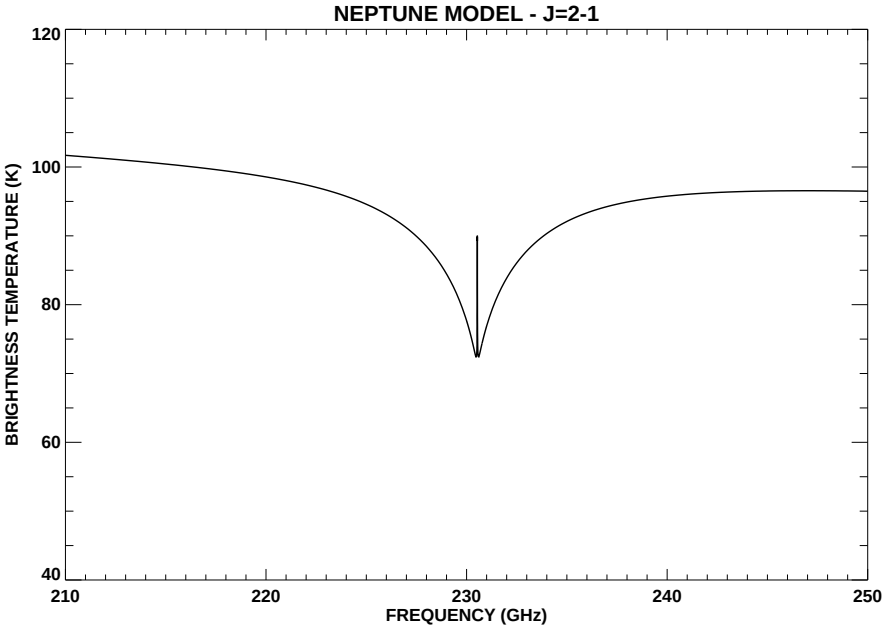

Figure 6.2: *The J=2–1 CO line at 230.5 GHz for a uniform CO mole ratio of* $1\text{x}10^{-6}$ *and a resolution of 1.25 MHz.*

ratios of $1\text{x}10^{-6}$. The contribution functions corresponding to these lines are shown in Figs. 6.4 and 6.5; for comparison the J=3–2 contribution functions are shown in Fig. 6.6. The contribution from the central frequencies (red curves) of all three lines peak at different levels in the stratosphere and the J=2–1 line shows a broad contribution over a range of pressure levels including a significant component in the lower troposphere. The peak of the contribution functions at 0.5, 5, and 10 GHz from line centre (green, blue, and violet curves) also corresponds to different pressure levels in the atmosphere. Model fits to measurements of these lines will allow a more complete CO abundance profile to be constructed. In addition, observations of the J=2–1, 3–2, and 4–3 CO lines in Uranus will also be attempted to confirm the tentative detection of CO obtained with the FTS.

It was concluded in chapter 4 that improved FTS measurements of CO in Neptune and Uranus require a system that can provide instantaneous removal of atmospheric emission. The imaging FTS (Gom and Naylor 2004, Naylor and Gom 2003) being developed for SCUBA-2 (Holland *et al.* 2003) is a dual-port system that will fulfill

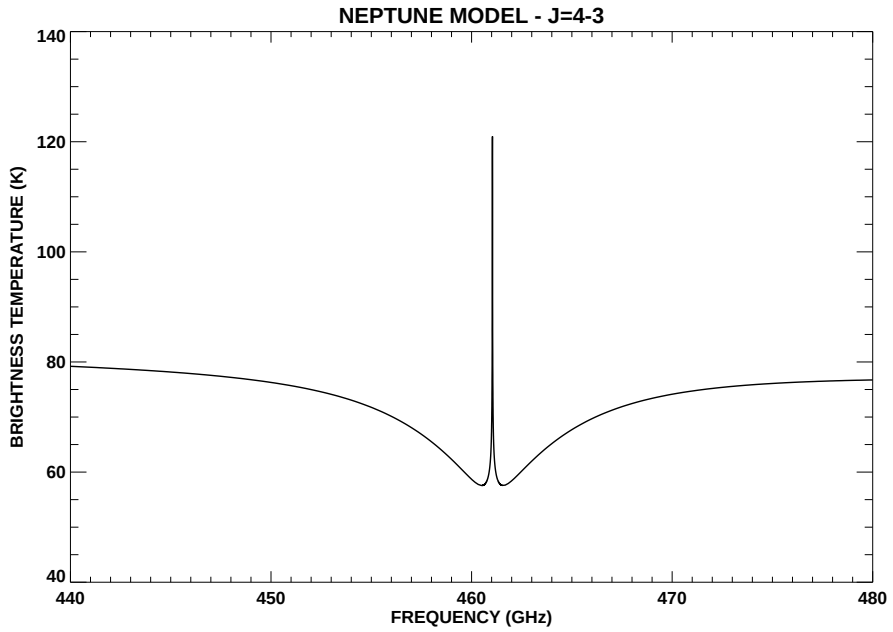

Figure 6.3: *The J=4–3 CO line at 461.0 GHz for a uniform CO mole ratio of* $1\text{x}10^{-6}$ *and a resolution of 1.25 MHz.*

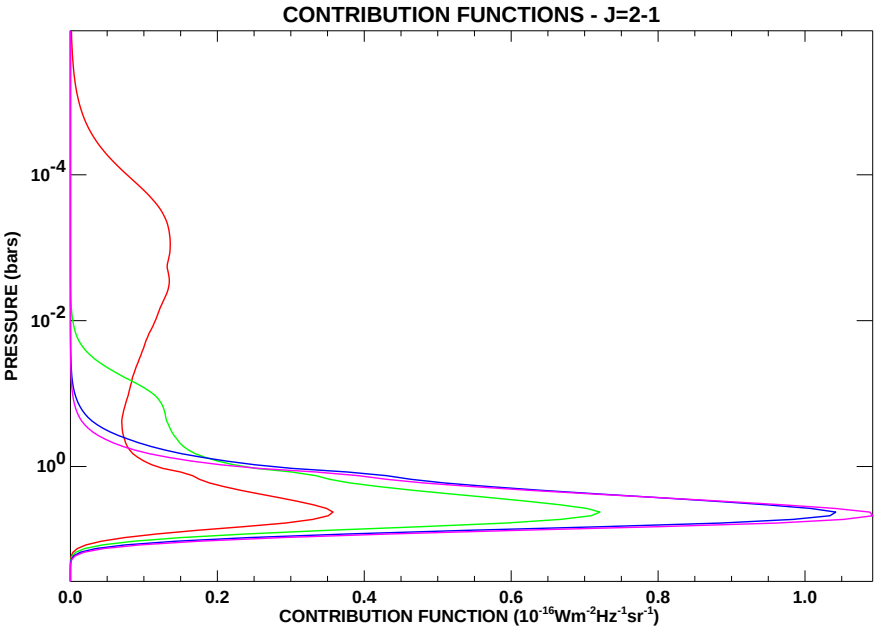

Figure 6.4: *The contribution functions for the J=2–1 CO line. The contribution functions are plotted for the central frequency (red). Frequencies 0.5, 5, and 10 GHz from line centre (green, blue, and violet respectively) are also shown.*

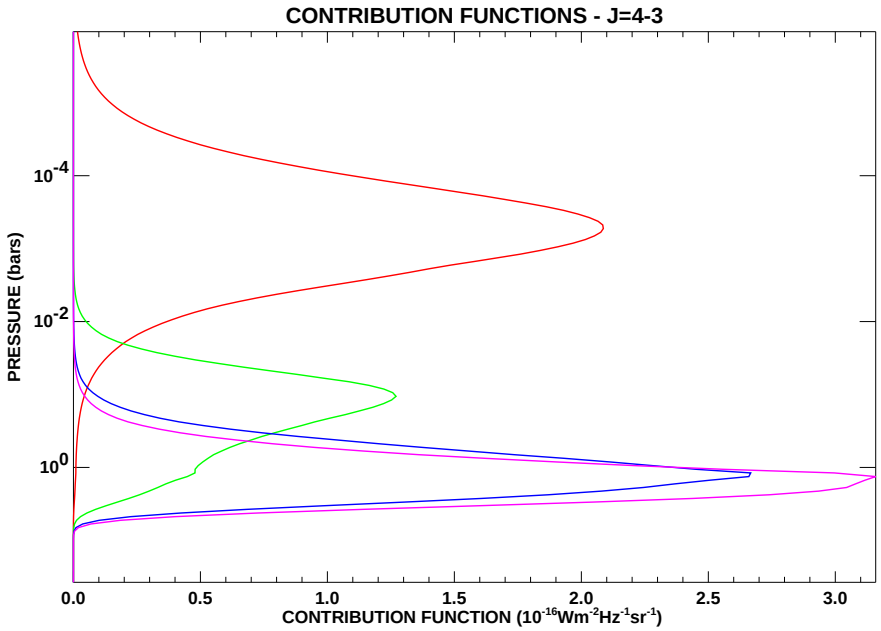

Figure 6.5: *The contribution functions for the J=4–3 CO line. The contribution functions are plotted for the central frequency (red). Frequencies 0.5, 5, and 10 GHz from line centre (green, blue, and violet respectively) are also shown.*

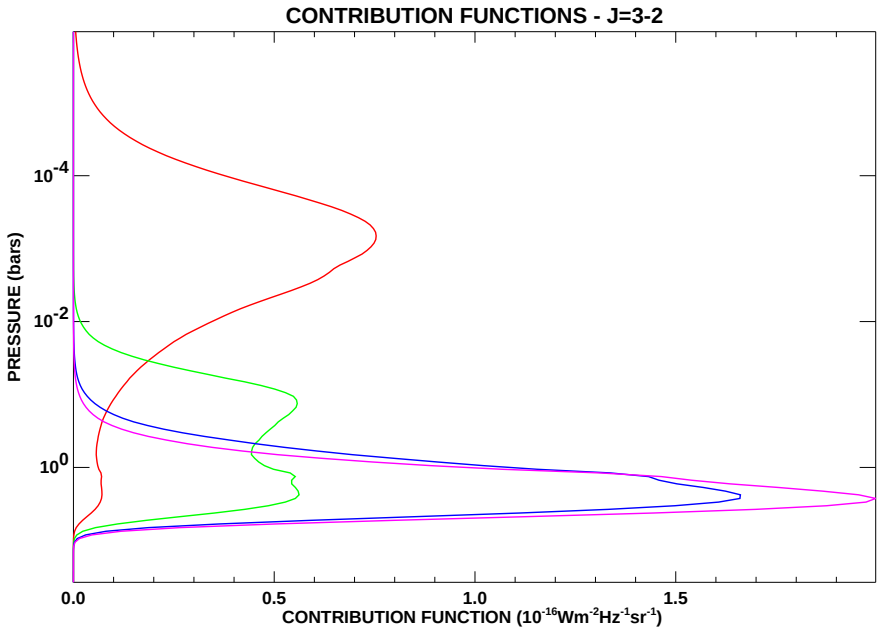

Figure 6.6: *The contribution functions for the J=3–2 CO line. The contribution functions are plotted for the central frequency (red). Frequencies 0.5, 5, and 10 GHz from line centre (green, blue, and violet respectively) are also shown.*

this requirement. SCUBA-2 is the successor to SCUBA, and will have ∼5,000 pixels in each of the 450 and 850μm arrays compared to 91 and 37 pixels for the 450 and 850μm arrays in SCUBA. SCUBA-2 will map the submillimetre sky up to 1000 times faster than SCUBA.

The imaging FTS is being built using the MZ design described in Chapter 4 and will operate at resolutions from 3 to 0.15 GHz. It will have a 3′x3′ field-of-view in each port and will simultaneously produce spectra in the 450 and 850μm bands. The expected per-pixel sensitivity is 280 mJy for a 1-hour integration at the highest resolution (Gom and Naylor 2004). This, combined with instantaneous removal of atmospheric emission, will provide sufficient precision to measure the shapes of the CO lines in both Neptune and Uranus.

It was always part of the observing plan for this thesis project to repeat the SCUBA observations described in Chapter 5 with the following improvements to the observing procedure:

1. Mars, Neptune, and Uranus must be observed on the same day and as close together in time as possible;

2. The pointing must be accurate to within 1.5″ on all sources;

3. Before and after each source measurement a skydip must be performed; and,

4. The WVM must be functioning so that skydip and WVM data can be correlated to more accurately constrain the pwv during each measurement.

SCUBA was recently decommissioned, however, due to a cryogenic fault, precluding any further photometric measurements for this project.

Photometric measurements of Neptune were an interesting attempt to measure the CO abundance indirectly. The superior results obtained using the spectroscopic techniques presented here indicate that this method is not a very promising approach for measuring the CO in both Neptune and Uranus. Photometric measurements using SCUBA-2 for the purpose of measuring the CO abundance in these planets

will likely never be attempted because of the far superior results that will possible using the SCUBA-2 imaging FTS.

References

Ade, P. A. R., P. A. Hamilton, and D. A. Naylor 1999. An absolute dual beam emission spectrometer. Topical meeting poster FWE3.

Appleby, J. F. 1986. Radiative-convective equilibrium models of Uranus and Neptune. *Icarus* **65**, 383–405.

Archibald, E. N., T. Jenness, W. S. Holland, I. M. Coulson, N. E. Jessop, J. A. Stevens, E. I. Robson, R. P. J. Tilanus, W. D. Duncan, and J. F. Lightfoot 2002. On the atmospheric limitations of ground-based submillimetre astronomy using array receivers. *Monthly Notices of the Royal Astronomical Society* **336**, 1–13.

Armstrong, B. H. 1967. Spectrum line profiles: the Voigt function. *Journal of Quantitative Spectroscopy and Radiative Transfer* **7**, 61–88.

Avery, L. 1998. Calibration, beamwidths, and efficiencies. `http://www.jach.hawaii.edu/JCMT/spectral_line/Instrument_homes/RxB3/cal.html`.

Bachet, G., E. R. Cohen, P. Dore, and G. Birnbaum 1983. The translational-rotational absorption spectrum of hydrogen. *Canadian Journal of Physics* **61**, 591–603.

Baines, K. H., and H. B. Hammel 1994. Clouds, hazes, and the stratospheric methane abundance in Neptune. *Icarus* **109**, 20–39.

Baines, K. H., M. E. Mickelson, L. E. Larson, and D. W. Ferguson 1995. The abundances of methane and ortho/para hydrogen on Uranus and Neptune: Implications of new laboratory 4-0 H_2 quadrupole line parameters. *Icarus* **114**, 328–340.

Barnett, J. J., and M. Corney 1985. Middle atmosphere reference model derived from satellite data. In K. Labitzke, J. J. Barnett, and B. Edwards (Eds.), *Handbook MAP 16, SCOSTEP*. Urbana: University of Illinois.

Bell, R. J. 1972. *Introductory Fourier Transform Spectroscopy*. New York: Academic Press.

Belton, M. J. S., and H. Spinrad 1973. Pressure-induced lines in the spectra of the major planets. *Astrophysical Journal* **185**, 363–372.

Bézard, B., P. N. Romani, H. Feuchtgruber, and T. Encrenaz 1999. Detection of the methyl radical on Neptune. *Astrophysical Journal* **515**, 868–872.

Bishop, S. K. Atreya, P. N. Romani, B. R. Sandel, and F. Herbert 1992. Voyager 2 ultraviolet spectrometer solar occultations at Neptune - Constraints on the abundance of methane in the stratosphere. *Journal of Geophysical Research* **97**, 11681–11694.

Bishop, J., S. K. Atreya, P. N. Romani, G. S. Orton, B. R. Sandel, and R. V. Yelle 1995. The middle and upper atmosphere of Neptune. In D. P. Cruikshank (Ed.), *Neptune and Triton*, pp. 427–487. Tucson : University of Arizona Press.

Bishop, J., P. N. Romani, and S. K. Atreya 1998. Voyager 2 ultraviolet spectrometer solar occultations at Neptune: Photochemical modeling of the 125-165 nm lightcurves. *Planetary Space Science* **46**, 1–20.

Borysow, A., and L. Frommhold 1986. Theoretical collision-induced rototranslational absorption spectra for the outer planets: H_2-CH_4. *The Astrophysical Journal* **304**, 849–865.

Borysow, J., and L. Frommhold 1988. Collision-induced rototranslational absorption spectra of H_2-He pairs at temperatures from 40 to 3000k. *The Astrophysical Journal* **326**, 509–515.

Borysow, J., L. Trafton, L. Frommhold, and G. Birnbaum 1985. Modeling of pressure-induced far-infrared absorption spectra: Molecular hydrogen pairs. *The Astrophysical Journal* **296**, 644–654.

Brehm, J. J., and W. J. Mullin 1989. *Introduction to the Structure of Matter*. Toronto: John Wiley and Sons Inc.

Brigham, E. O. 1974. *The Fast Fourier Transform*. Englewood Cliffs, New Jersey: Prentice-Hall Inc.

Broadfoot, A. L., S. K. Atreya, J. L. Bertaux, J. E. Blamont, A. J. Dessler, and S. Linick 1989. Ultraviolet spectrometer observations of Neptune and Triton. *Science* **246**, 1459–1466.

Burgdorf, M., G. S. Orton, G. R. Davis, S. D. Sidher, H. Feuchtgruber, M. J. Griffin, and B. M. Swinyard 2003. Neptune's far-infrared spectrum from the ISO long-wavelength and short-wavelength spectrometers. *Icarus* **164**, 244–253.

Chapman, I. M. 2000. *The atmosphere above Mauna Kea at mid-infrared wavelengths*. Master of Science, University of Lethbridge.

Clancy, R. T., B. J. Sandor, and G. H. Moriarty-Schieven 2003. Doppler wind measurements of Mars atmospheric circulation. *AAS/Division for Planetary Sciences Meeting Abstracts* **35**, 140.

Conrath, B. J., D. Gautier, G. F. Lindal, R. E. Samuelson, and W. A. Shaffer 1991. The helium abundance of Neptune from Voyager measurements. *Journal of Geophysical Research* **96**, 18907–18919.

Conrath, B. J., P. J. Gierasch, and E. A. Ustinov 1998. Thermal structure and para hydrogen fraction on the outer planets from voyager IRIS measurements. *Icarus* **135**, 501–517.

Conrath, B. J., R. A. Hanel, and R. E. Samuelson 1989. Thermal structure and heat balance of the outer planets. In S. K. Atreya, J. B. Pollack, and M. S. Matthews (Eds.), *Origin and Evolution of Planetary and Satellite Atmospheres*, pp. 513–538. University of Arizona Press.

Cooley, J. W., and J. W. Tukey 1965. An algorithm for the machine calculation of complex Fourier series. *Mathematics of Computation* **19**, 297–301.

Courtin, R., D. Gautier, and D. Strobel 1996. The CO abundance on Neptune from HST observations. *Icarus* **123**, 37–55.

Davis, G. R., D. A. Naylor, M. J. Griffin, T. A. Clark, and W. S. Holland 1997. Broadband submillimeter spectroscopy of HCN, NH_3, and PH_3 in the troposphere of Jupiter. *Icarus* **130**, 387–403.

de Bergh, C., B. L. Lutz, T. Owen, and J. P. Maillard 1990. Monodeuterated methane in the outer solar system. IV - Its detection and abundance on Neptune. *Astrophysical Journal* **355**, 661–666.

de Pater, I., and J. J. Lissauer 2001. *Planetary Sciences*. Cambridge: Cambridge University Press.

Duncan, W. D., E. I. Robson, P. A. R. Ade, M. J. Griffin, and G. Sandell 1990. A millimetre/submillimetre common user photometer for the James Clerk Maxwell Telescope. *Monthly Notices of the Royal Astronomical Society* **243**, 126–132.

Encrenaz, T., E. Lellouch, H. Feuchtgruber, G. S. Orton, and S. K. Atreya 2004. First detection of CO in Uranus. *Astronomy and Astrophysics* **413**, L5–L9.

Encrenaz, T., E. Serabyn, and E. W. Weisstein 1996. Millimeter spectroscopy of Uranus and Neptune: Constraints on CO and PH_3 tropospheric abundances. *Icarus* **124**, 616–624.

Feuchtgruber, H., E. Lellouch, B. Bézard, T. Encrenaz, T. de Graauw, and G. R. Davis 1999. Detection of HD in the atmospheres of Uranus and Neptune: a new determination of the D/H ratio. *Astronomy and Astrophysics* **341**, L17–L21.

Feuchtgruber, H., E. Lellouch, T. de Graauw, B. Bézard, T. Encrenaz, and M. Griffin 1997. External supply of oxygen to the atmospheres of the giant planets. *Nature* **389**, 159–162.

Gautier, D., B. J. Conrath, T. Owen, I. de Pater, and S. K. Atreya 1995. The troposphere of Neptune. In D. P. Cruikshank (Ed.), *Neptune and Triton*, pp. 547–611. Tucson : University of Arizona Press.

Gom, B. G., and D. A. Naylor 2004. An update on the imaging Fourier transform spectrometer for SCUBA-2. In *Proc. SPIE Vol. 5498 Astronomical Structures and Mechanisms Technology*, pp. 695–704.

Griffin, M. J., P. A. R. Ade, G. S. Orton, E. I. Robson, W. K. Gear, I. G. Nolt, and J. V. Radostitz 1986. Submillimeter and millimeter observations of Jupiter. *Icarus* **65**, 244–256.

Griffin, M. J., and G. S. Orton 1993. The near-millimeter brightness temperature spectra of Uranus and Neptune. *Icarus* **105**, 537–548.

Guilloteau, S., A. Dutrey, A. Marten, and D. Gautier 1993. CO in the troposphere of Neptune: Detection of the J = 1-0 line in absorption. *Astronomy and Astrophysics* **279**, 661–667.

Hanel, R. A., B. J. Conrath, D. E. Jennings, and R. E. Samuelson 1992. *Exploration of the Solar System by Infrared Remote Sensing*. New York: Cambridge University Press.

Hedin, A. E. 1991. Extension of the MSIS thermospheric model into the middle and lower atmosphere. *Journal of Geophysical Research* **96**, 1159–1172.

Hoffman, J. P., P. G. Steffes, and D. R. DeBoer 2001. Laboratory measurements of the microwave opacity of phosphine: Opacity formalism and application to the atmospheres of the outer planets. *Icarus* **152**, 172–184.

Holland, W. S., W. Duncan, B. D. Kelly, K. D. Irwin, A. J. Walton, P. A. R. Ade, and E. I. Robson 2003. SCUBA-2: a new generation submillimeter imager for the James Clerk Maxwell Telescope. In *Proc. SPIE Vol. 4855 Millimeter and Submillimeter Detectors for Astronomy*, pp. 1–18.

Holland, W. S., E. I. Robson, W. K. Gear, C. R. Cunningham, J. F. Lightfoot, T. Jenness, R. J. Ivison, J. A. Stevens, P. A. R. Ade, M. J. Griffin, W. D. Duncan, J. A. Murphy, and D. A. Naylor 1999. SCUBA: a common-user submillimetre camera operating on the James Clerk Maxwell Telescope. *Monthly Notices of the Royal Astronomical Society* **303**, 659–672.

Hubbard, W. B., P. D. Nicholson, E. Lellouch, B. Sicardy, A. Brahic, F. Vilas, P. Bouchet, R. A. McLaren, R. L. Millis, L. H. Wasserman, J. H. Elais, K. Matthews, J. D. McGill, and C. Perrier 1987. Oblateness, radius, and mean stratospheric temperature of Neptune from the 1985 August 20 occultation. *Icarus* **72**, 635–646.

Hubbard, W. B., M. Podolak, and D. J. Stevenson 1995. The interior of Neptune. In D. P. Cruikshank (Ed.), *Neptune and Triton*, pp. 109–138. Tucson : University of Arizona Press.

Jenness, T., and J. F. Lightfoot 2000. Starlink User Note 216 Starlink Project. `http://docs.jach.hawaii.edu/star/sun216.htx/sun216.html`.

Kraus, J. D. 1966. *Radio Astronomy.* McGraw Hill.

Kutner, M. L., and B. L. Ulich 1981. Recommendations for calibration of millimeter-wavelength spectral line data. *The Astrophysical Journal* **250**, 341–348.

Lazareff, B. 2005. Photon-assisted tunneling. `http://iram.fr/IRAMFR/TA/receiver/rxtutorial/rxtutorial.htm`.

Learner, R. C. M., A. P. Thorne, I. Wynne-Jones, J. W. Brault, and M. C. Abrams 1995. Phase correction of emission line Fourier transform spectra. *Journal of the Optical Society of America* **12**, 2165–2171.

Lellouch, E. 1996. Chemistry induced by the impacts: observations. In K. S. Noll, H. A. Weaver, and P. D. Feldman (Eds.), *The Collision of Comet Shoemaker-Levy 9 and Jupiter, IAU Colloquium no 156*, pp. 213–242. Cambridge University Press.

Lellouch, E., R. Moreno, and G. Paubert 2005. A dual origin for Neptune's carbon monoxide. *Astronomy and Astrophysics* **430**, L37–L40.

Lellouch, E., P. N. Romani, and J. Rosenqvist 1994. The vertical distribution and origin of HCN in Neptune's atmosphere. *Icarus* **108**, 112–136.

Lesurf, J. 2005. Heterodyne systems and complex signals. `http://www.st-andrews.ac.uk/~www_pa/Scots_Guide/RadCom/part1/page3.html`.

Lewis, J. S. 1997. *Physics and Chemistry of the Solar System.* San Diego: Academic Press.

Lide, D. R. (Ed.) 2003. *CRC Handbook of Chemistry and Physics, 2003-2004.* New York: CRC Press.

Lindal, G. F. 1992. The atmosphere of Neptune - An analysis of radio occultation data acquired with Voyager 2. *The Astronomical Journal* **103**, 967–982.

Lindal, G. F., J. R. Lyons, D. N. Sweetnam, V. R. Eshleman, and D. P. Hinson 1990. The atmosphere of Neptune - Results of radio occultation measurements with the Voyager 2 spacecraft. *Geophysical Research Letters* **17**, 1733–1736.

Lindal, G. F., J. R. Lyons, D. N. Sweetnam, V. R. Eshleman, D. P. Hinson, and G. L. Tyler 1987. The atmosphere of Uranus - Results of radio occultation measurements with Voyager 2. *Journal of Geophysical Research* **92**, 14897–15001.

Lodders, K., and B. Fegley 1994. The origin of carbon monoxide in Neptunes's atmosphere. *Icarus* **112**, 368–375.

Marten, A., D. Gautier, T. Owen, D. B. Saunders, H. E. Matthews, S. K. Atreya, R. P. J. Tilanus, and J. R. Deane 1993. First observations of CO and HCN on Neptune and Uranus at millimeter wavelengths and the implications for atmospheric chemistry. *Astrophysical Journal* **406**, 285–297.

Marten, A., H. E. Matthews, T. Owen, R. Moreno, T. Hidayat, and Y. Biraud 2005. Improved constraints on Neptune's atmosphere from submillimetre wavelength observations. *Astronomy and Astrophysics* **429**, 1097–1105.

Martin, D. H., and E. Puplett 1969. Polarised interferometric spectrometry for the millimetre and submillimetre spectrum. *Infrared Physics* **10**, 105–109.

Matthews, H. E., J. Leech, and P. Friberg 2004. Guide to spectral line observing at the JCMT. Technical report, JAC.

Moses, J. I. 1992. Meteoroid ablation in Neptune's atmosphere. *Icarus* **99**, 368–383.

Naylor, D. A., T. A. Clark, and G. R. Davis 1994. A polarizing Fourier transform spectrometer for astronomical spectroscopy at submillimeter and mid-infrared wavelengths. In *Proc. SPIE Vol. 2198 Instrumentation in Astronomy VIII*, pp. 703–714.

Naylor, D. A., G. R. Davis, M. J. Griffin, T. A. Clark, D. Gautier, and A. Marten 1994. Broad-band spectroscopic detection of the CO J=3-2 tropospheric absorption in the atmosphere of Neptune. *Astronomy and Astrophysics* **291**, L51–L53.

Naylor, D. A., and B. G. Gom 2003. SCUBA-2 imaging Fourier transform spectrometer. In *Proc. SPIE Vol. 5159 Imaging Spectrometry IX*, pp. 91–101.

Naylor, D. A., B. G. Gom, P. A. R. Ade, and J. E. Davis 1999. Design and performance of a dual polarizing detector system for broadband astronomical spectroscopy at submillimeter wavelengths. *Review of Scientific Instruments* **70**, 4097–4109.

Naylor, D. A., B. G. Gom, I. Schofield, G. Tompkins, and G. R. Davis 2003. A Mach-Zehnder Fourier transform spectrometer for astronomical spectroscopy at submillimeter wavelengths. In *Proc. SPIE Vol. 4855 Millimeter and Submillimeter Detectors for Astronomy*, pp. 540–551.

Noll, K. S., R. F. Knacke, T. R. Geballe, and A. T. Tokunaga 1986. Detection of carbon monoxide in Saturn. *Astrophysical Journal* **309**, L91–L94.

Norton, R. H., and R. Beer 1976. New apodizing functions for Fourier spectrometry. *Journal of the Optical Society of America* **66**, 259–263.

Orton, G. S., D. K. Aitken, C. Smith, P. F. Roche, J. Caldwell, and R. Snyder 1987. The spectra of Uranus and Neptune at 8-14 and 17-23 μm. *Icarus* **70**, 1–12.

Orton, G. S., K. H. Baines, J. Caldwell, P. N. Romani, A. T. Tokunaga, and R. A. West 1990. Calibration of the 7- to 14-μm brightness spectra of Uranus and Neptune. *Icarus* **85**, 257–265.

Orton, G. S., M. J. Griffin, P. A. R. Ade, I. G. Nolt, and J. V. Radostitz 1986. Submillimeter and millimeter observations of Uranus and Neptune. *Icarus* **67**, 289–304.

Orton, G. S., J. H. Lacy, J. M. Achtermann, P. Parmar, and W. E. Blass 1992. Thermal spectroscopy of Neptune - the stratospheric temperature, hydrocarbon abundances, and isotopic ratios. *Icarus* **100**, 541–555.

Phillips, T. G. 1988. Techniques of submillimeter astronomy. In R. D. Wolstencroft and W. B. Burton (Eds.), *Millimetre and Submillimetre Astronomy*, pp. 1–24. Kluwer Academic Publishers.

Pickett, H. M., R. L. Poynter, E. A. Cohen, M. L. Delitsky, J. C. Pearson, and H. S. P. Muller 1998. Submillimeter, millimeter, and microwave spectral line catalog. *Journal of Quantitative Spectroscopy and Radiative Transfer* **60**, 883–890.

Privett, G., T. Jenness, and H. Matthews 1998. Planetary brightness and flux density calculations. `http://www.starlink.rl.ac.uk/star/docs/sun213.htx/node5.html`.

Romani, P. N., J. Bishop, B. Bézard, and S. Atreya 1993. Methane photochemistry on Neptune: ethane and acetylene mixing ratios and haze production. *Icarus* **106**, 442–463.

Roques, F., B. Sicardy, R. G. French, W. B. Hubbard, A. Barucci, P. Bouchet, A. Brahic, J. A. Gehrels, T. Gehrels, I. Grenier, T. Lebertre, J. Lecacheux, J. P. Maillard, R. A. McLaren, C. Perrier, F. Vilas, and M. D. Waterworth 1994. Neptune's upper stratosphere, 1983-1990: ground-based stellar occultation observations iii. Temperature profiles. *Astronomy and Astrophysics* **288**, 985–1011.

Rosenqvist, J., E. Lellouch, P. N. Romani, G. Paubert, and T. Encrenaz 1992. Millimeter-wave observations of Saturn, Uranus, and Neptune - CO and HCN on Neptune. *Astrophysical Journal* **392**, L99–L102.

Rothman, L. S., D. Jacquemart, A. Barbe, D. C. Benner, M. Birk, L. R. Brown, M. R. Carleer, C. Chackerian, K. Chance, L. H. Coudert, V. Dana, V. M. Devi, J. M. Flaud, R. R. Gamache, A. Goldman, J. M. Hartmann, K. W. Jucks, A. G. Maki, J. Y. Mandin, S. T. Massie, J. Orphal, A. Perrin, C. P. Rinsland, M. A. H. Smith, J. Tennyson, R. N. Tolchenov, R. A. Toth, J. Vander Auwera, P. Varanasi, and G. Wagner 2005. The HITRAN 2004 molecular spectroscopic database. submitted to the Journal of Quantitative Spectroscopy and Radiative Transfer.

Rothman, L. S., C. P. Rinsland, A. Goldman, S. T. Massie, D. P. Edwards, J. M. Flaud, A. Perrin, C. Camy-Peyret, V. Dana, J. Y. Mandin, J. Schroeder, A. McCann, R. R. Gamache, R. B. Wattson, K. Yoshino, K. V. Chance, K. W. Jucks, L. R. Brown, V. Nemtchinov, and P. Varanasi 1998. The HITRAN molecular spectroscopic database and HAWKS (HITRAN Atmospheric Workstation): 1996 edition. *Journal of Quantitative Spectroscopy and Radiative Transfer* **60**, 665–710.

Schulz, B., Encrenaz, B. Bézard, P. N. Romani, E. Lellouch, and S. K. Atreya 1999. Detection of C_2H_4 in neptune from ISO/PHT-S observations. *Astronomy and Astrophysics* **350**, L13–L17.

Tahić, M. K. 2004. *Fourier transform spectroscopy of the Orion molecular cloud*. Master of Science, University of Lethbridge.

Ulich, B. L. 1981. Millimeter-wavelength continuum calibration sources. *The Astronomical Journal* **86**, 1619–1626.

Ulich, B. L., and R. W. Haas 1976. Absolute calibration of millimeter-wavelength spectral lines. *The Astrophysical Journal, Supplement Series* **30**, 247–258.

White, G. J. 1988. Receiver technology. In R. D. Wolstencroft and W. B. Burton (Eds.), *Millimetre and Submillimetre Astronomy*, pp. 27–94. Kluwer Academic Publishers.

Wright, E. L. 1976. Recalibration of the far-infrared brightness temperatures of the planets. *The Astrophysical Journal* **210**, 250–253.

Yelle, R. V., F. Herbert, B. R. Sandel, R. J. Vervack, and T. M. Wentzel 1993. The distribution of hydrocarbons in Neptune's upper atmosphere. *Icarus* **104**, 38–59.

Zeilik, M., S. A. Gregory, and E. v. P. Smith 1992. *Introductory Astronomy and Astrophysics*. New York: Saunders College Publishing.